Dissertation

SUBMITTED TO THE

Combined Faculties of the Natural Sciences and Mathematics
of the Ruperto-Carola-University of Heidelberg, Germany

FOR THE DEGREE OF

Doctor of Natural Sciences

Put forward by

Xiangjin Kong (孔祥进)

Born in: Xinghua, Jiangsu, People's Republic of China (PRC)

(出生地:中华人民共和国江苏省兴化市)

Oral examination: 28.07.2016

Collective effects of nuclei in single x-ray photon superradiance

Referees: **Priv. Doz. Dr. Adriana Pálffy-Buß**
Prof. Dr. Jörg Jäckel

Zusammenfassung

In dieser Arbeit werden kollektive Kerneffekte in der Superradianz einzelner Röntgenphotonen behandelt. Zu diesem Zweck untersuchen wir verschiedene Aspekte der Superradianz sowohl im Aufbau der Kernvorwärtsstreuung als auch in Dünnschichtkavitäten mit ^{57}Fe-Kernen. Ein allgemeingültiges theoretisches Modell wird dazu entwickelt, welches in der Lage ist, die kooperative Emission einzelner Photonen in resonanten Systemen (Atome oder Kerne) unter dem Einfluss der magnetischen Hyperfeinaufspaltung zu beschreiben. Im Grenzfall dicker Proben zeigen unsere Ergebnisse die Möglichkeit auf, die kollektive Emission einzelner Röntgenphotonen im Zuge der Kernvorwärtsstreuung kohärent zu kontrollieren. Des Weiteren haben wir herausgefunden, dass im Fall dünner Eisenschichten eingebettet in Dünnschichtkavitäten interessante kollektive Effekte auftreten, welche die nukleare Levelstruktur der Hyperfeinaufspaltung modifizieren. Zusätzlich hierzu existiert für dieses Setup ein Parameterbereich, in dem ein Spektrum analog zur elektromagnetisch induzierten Transparenz (EIT) erzeugt wird. Basierend auf diesem EIT-ähnlichen Effekt entwickeln wir einen Kontrollmechanismus, um Röntgenpulse in Dünnschichtkavitäten zu stoppen. Schließlich zeigen wir theoretisch, dass es im Fall zweier Kern-Ensembles in einer Dünnschichtkavität zur Aufspaltung der Niveaus kommt, welche durch die starke Kopplung zwischen den beiden Kernschichten hervorgerufen wird und an die Rabi-Spaltung erinnert. Diese Erkenntnis ist anhand vorläufiger Daten bereits experimentell bestätigt.

Abstract

This thesis is dedicated to the study of collective effects of nuclei in single x-ray photon superradiance. To this end we investigate aspects of superradiance in both nuclear forward scattering and in thin-film cavities with an embedded ^{57}Fe nuclear layer. A general theoretical framework is developed to investigate a single-photon cooperative emission from a cloud of resonant systems, atoms or nuclei, in the presence of magnetic hyperfine splitting. In the limit of a thick sample, we present our results for two means to coherently control the collective single x-ray photon emission in nuclear forward scattering. In the limit of a thin sample in a thin-film cavity with embedded resonant nuclei, we find out that unlike the magnetic hyperfine splitting of a single atom or nucleus, interesting collective effects may occur which modify the hyperfine level structure. In addition, for a certain parameter regime a spectrum reminiscent of electromagnetically induced transparency (EIT) can be achieved. Based on this EIT-like effect, a theoretical control mechanism for stopping x-ray pulses in the thin-film x-ray cavity is put forward. Finally, we show theoretically that for the case of two nuclear ensembles in the thin-film cavity, pseudo-Rabi splitting due to the strong coupling between the two layers should occur. The latter findings are confirmed by preliminary experimental data.

Within the framework of this thesis, the following articles were published in refereed journals:

- ***Field control of single x-ray photons in nuclear forward scattering***
  Xiangjin Kong, W.-T. Liao and Adriana Pálffy
  New Journal of Physics **16**, 013049 (2014).

- ***Stopping Narrow-Band X-Ray Pulses in Nuclear Media***
  Xiangjin Kong and Adriana Pálffy
  Phys. Rev. Lett. **116**, 197402 (2016).

Articles submitted for publication in refereed journals:

- ***Collective magnetic splitting in single-photon superradiance***
  Xiangjin Kong and Adriana Pálffy
  arXiv: **1606**, 02988 (2016).

Articles in preparation:

- ***Collective strong coupling of x-rays in nuclear media***

Contents

Chapter 1

Introduction

Without light, the matter remains in darkness. Without matter, the light is useless. God said "Let there be light" because it had already created matter. However, it is not enough to only have matter. The world could be vivid only if both light and matter appeared. If we agree with the Genesis that light and matter are the basic elements of the world, then light-matter interaction is the bridge connecting the world. The light-matter interaction in the blackbody radiation has led to the beginning of quantum mechanics and opened the door for the quantum world. In order to solve the problem of blackbody radiation, Max Planck proposed the famous hypothesis about energy quantization: there is energy exchange between the light in a cavity and the atoms in the walls of the cavity, but the exchanged energy only can be discrete in the interaction of light with atoms. This is described by the equation $E = h\nu$ where h is Planck's constant and ν is the frequency of the emitted light. For this bold hypothesis presented in 1900, Planck was awarded the Nobel Prize in Physics in 1918. Later on, in 1905 Albert Einstein used the hypothesis of light quanta (later called photons) to explain the photoelectric effect discovered by Heinrich Hertz. The main idea of Einstein's hypothesis was that the light energy was carried in discrete quantized packets in the interaction of light with electrons. Einstein earned the Nobel Prize in Physics for his discovery of the law of the photoelectric effect in 1921. In 1923, Arthur Compton discovered the Compton effect which demonstrated that light could not be explained purely as wave. The particle viewpoint of light according to which photons carry momentum and energy was supported by the discovery of the Compton effect. It was this final piece in the puzzle which established the wave-particle duality of light. Compton won Nobel Prize in Physics for the discovery in 1927.

Light-matter interaction was used as a main tool during the establishment of the concept of photon. The invention of laser in 1960 was a significant event for light-matter interaction. It led to the beginning of the investigation of coherent light-matter interactions such as self-induced transparency [1, 2], photon echoes [3, 4] and optical nutation [5, 6]. The appearance of tunable lasers made the study of the resonant light-matter interactions possible. It led to the beginning of modern quantum optics. The light can drive a two-level atom from the ground state to the excited state if the photon is close to the transition energy. One photon will be absorbed during this process. Then the excited atom decays to the ground state and emits one photon via stimulated or spontaneous decay. Spontaneous emission was unexplained within the framework of classical electromagnetic fields. In order to explain the spontaneous decay, the light should be quantized and the

vacuum-matter interaction should be introduced. The vacuum-matter interaction also plays an important role in the case of a single photon absorbed by a cloud of atoms followed by correlated spontaneous emission. Dicke pointed out that a single photon of wavelength λ stored uniformly in an atomic cloud of size $R \ll \lambda$ is emitted spontaneously with a rate $N\gamma$, where γ is the single atom decay rate and N is the number of the atoms [7]. This is the concept of superradiance. In such a system, not only the spontaneous decay rate is enhanced but also the resonant level has a energy shift which is called the collective Lamb shift [8–10]. Surprisingly, the clearest experimental observation of the collective Lamb shift has been recently performed with x-ray photons [11].

In quantum optics, typically photons in the microwave, infrared or optical regime have been used for years. Recently more and more attention has been focused on x-rays. Why x-rays? At present, x-ray quantum optics is much less advanced compared to its optical counterpart. However, the hope is that x-ray quantum optics may enable coherent control of x-rays, with potential applications for the fields of petrology, material science, quantum information, biology and chemistry. The desirable properties of x-rays are deeper penetration, better focus, no longer limited by an inconvenient diffraction limit as for optical photons, correspondingly spatial resolution, robustness, and the large momentum transfer they may produce. Recent years have witnessed the commissioning of coherent x-ray sources opening the new field of x-ray quantum optics [12]. The third-generation synchrotron radiation (SR) sources produce monochromatized and intense x-ray beams for a number of applications. The new fourth generation light sources like x-ray free-electron lasers (XFELs) [13–17] provide coherent x-ray beams with an even higher intensity compared to the SR sources.

With the high photon energy, x-rays are resonant to either inner shell electron transitions in highly charged ions or transitions in atomic nuclei. How come nuclear transitions? Nuclear transitions naturally lie in the x-ray and γ-ray frequency region. They are very well isolated from the environment and present long coherence times. Comparing with highly charged ions, nuclei are much easier to trap. The nuclei can be embedded into solid targets and no other trap devices are required. Coherent control tools based on nuclear cooperative effects [11, 18–20] are known also from nuclear forward scattering (NFS) experiments with third-generation light sources using Mössbauer nuclei. The underlying physics here relies on the delocalized nature of the nuclear excitation produced by SR light, i.e., the formation of so-called nuclear excitons and on their partially superradiant decay. For instance, a NFS setup in planar thin film waveguides [21] was used for novel quantum optics experiments in the x-ray regime using nuclei instead of atoms. The excitonic nature of the nuclear excitation in NFS was the feature that helped to identify the cooperative Lamb shift [11], to demonstrate electromagnetically induced transparency (EIT) [20] or to obtain spontaneously generated coherence [22] and to slow x-ray light [23] in a nuclear system. Furthermore, NFS setups also offer a framework for control of single x-ray photons, which might become a useful tool for optics and quantum information applications at shorter wavelengths on the way towards more compact photonic devices [24]. Phase-sensitive storage and π phase modulation for single hard x-ray photons in a NFS setup have been recently

proposed [25], as well as the generation of a nuclear polariton with two entangled counter-propagating branches [26] comprising a single x-ray photon. Single-qubit and binary logical operations based on the control of x-ray polarization, such as a destructive C-NOT gate were also discussed in the framework of NFS [27]. Using Mössbauer sources, the coherent control of the single-photon wavepackets shape has been recently demonstrated [28, 29]. With higher excitation rates becoming available, based on nuclear transitions, the manipulations of nuclei by coherent XFELs photons may open a door for some applications, such as a nuclear energy storage solution [30, 31]. The collective x-ray-matter interaction for an ensemble of nuclei will strongly depend on the shape and size of the sample. Accordingly, also the theoretical approaches to describe the collective excitation are different for bulk [32] or thin-film samples [33, 34].

In this thesis, we investigate from the theory side collective effects of nuclei in x-ray single photon superradiance. Our goal is to exploit the unique properties of nuclei for control at a single-photon level of x-ray quanta. We address here aspects of superradiance in both bulk nuclear samples and in thin-film cavities with an embedded ^{57}Fe nuclear layer. We develop for the first time a general theoretical framework to investigate a single-photon cooperative emission from a cloud of resonant systems, atoms or nuclei, in the presence of magnetic (hyperfine) splitting. Based on this formalism, we show that in addition to the collective Lamb shift, a so far *unknown modification of the magnetic hyperfine splitting* of the nuclear lines occurs. We also show that manipulation of the magnetic field may lead to the complete *storage of a narrow-band x-ray pulse* for times on the order of 100 ns. Finally, we investigate the regime of strong coupling of single x-ray photons in dissipative cavities. Our results show that for the case of two nuclear ensembles in the thin-film cavity, *pseudo-Rabi splitting due to strong coupling* between the two layers should occur. These three main results of this thesis are genuinely new and unexpected aspects of collective effects of nuclei in x-ray single photon superradiance, inviting for many applications in the field of x-ray science.

This thesis is structured as follows. In Chapter 2 we study the collective magnetic splitting in the single photon superradiance from a cloud of generic atoms. For simplicity, we only consider two resonant transitions. Based on the initial condition, we present characteristic single-photon radiation spectra. For instance, in some cases the energy gap between the two resonant transitions is no longer the same as the traditional Zeeman splitting of a single atom. The collective effects can broaden the gap. We also find that for a certain parameter domain, the shape of the splitting resembles an EIT-like spectrum for a single photon. Instead of two independent peaks, a transparency window appears in the radiation spectrum and this effect and its applications are discussed in more detail in Chapter 5.

We try to observe the collective effects presented in Chapter 2 with single x-ray photon interacting with ^{57}Fe nuclei. In Chapter 3, coherent control of single x-ray photon superradiance in NFS off bulk samples is investigated. Due to the different parameter regime characterizing the ensemble, we introduce a different theoretical approach based on the Maxwell-Bloch equations. We show that the simultaneous propagation of two pulses through the same nuclear sample can lead to the transfer of signal intensity between the two, depending on the corresponding

intensities and time delay between the pulses. Thus, the presence of a strong pulse, for instance produced by the XFEL, can lead to the enhancement or suppression of the signal of a weaker excitation, potentially comprising a single resonant x-ray photon. Furthermore, the signal of such a weak excitation can be shifted forward in time by the alternation between scattering intervals in the presence and absence of a hyperfine magnetic field. This is the inverse effect of coherent photon storage and may become a valuable technique if single x-ray photons are to become the information carriers in future photonic devices.

It is unfortunately not possible to observe experimentally the effects predicted in Chapter 2 in bulk (thick) ^{57}Fe samples investigated in Chapter 3. In Chapter 4 we study therefore a thin-film cavity with embedded ^{57}Fe nuclei probed by an x-ray pulse at grazing incidence. The thickness of the nuclear ensemble is on the scale of nanometers. We double-check here our general results from Chapter 2 with a quantum model developed specifically for the thin-film cavity in Ref. [33]. We show that the eigenvalues of the thin-film cavity system obtained from the quantum model are consistent with our results in Chapter 2 and that the radiation spectra calculated via the two methods agree well. Based on our analysis, the main effects predicted in Chapter 2, such as the EIT-like spectrum and the broadened split gap, should be observable in the thin-film x-ray cavity with embedded nuclei under experimental parameters available already today.

With the development of control over photons in optical regime, important applications based on the light-matter interaction in quantum optics have been put forward in the fields of quantum information and computation. Here, a single photon is used as a flying qubit which is a state in a two-dimensional Hilbert space. An essential technology is the ability to store the qubit. The way to store optical photons is based on EIT, a quantum interference effect that can be used to render a resonant opaque medium transparent. Typically, EIT can be achieved in a so-called Λ three-level system driven simultaneously by a strong control and a weaker probe pulse. Due to the control field, the medium becomes transparent for the probe pulse in a narrow window around the resonance frequency [35]. In the optical regime, EIT can be used to stop light in an atomic medium [36–40] by a sudden turning off of the control field. Turning back on the control field, the light is released. This is the typical way to store optical photons. However, due to the lack of two-color x-ray sources [41, 42] and the proper nuclear three-level systems, the traditional optical EIT scenario is not available at present for x-rays. In Chapter 5 we show that a spectrally narrow x-ray pulse can be mapped and stored as nuclear coherence in the thin-film cavity with embedded ^{57}Fe based on the EIT-like spectrum obtained in Chapter 4. The role of the control field is played by the hyperfine magnetic field. By switching off the control magnetic field, x-ray photons can be completely stored in the cavity for approximately 100 ns.

The implementation of quantum information and computation requires to efficiently control photons, ultimately at the single photon level, requiring strong coupling between light and matter. In order to achieve this strong coupling between single photons and atoms, usually high-quality cavities are used. When the atoms are confined in a cavity, the coupling strength of the photon-atom interaction can be enhanced. Ground-breaking experimental methods with optical and

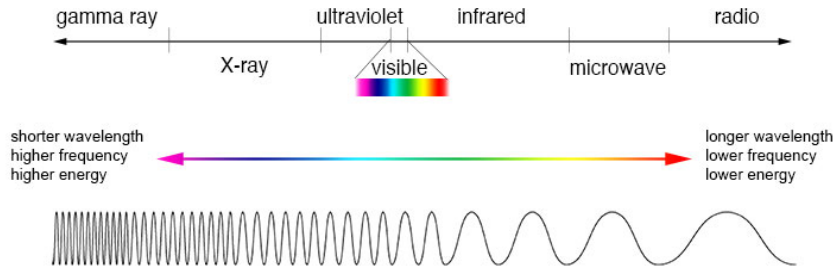

Figure 1.1: Comparison of wavelength, frequency and energy for the electromagnetic spectrum. (Credit: NASA's Imagine the Universe).

microwave cavities have enabled measuring and manipulation of individual quantum systems, for instance, quantum entanglement between atoms and photons [43], quantum phase transitions [44, 45] and quantum logic gates [46, 47]. Photon blockade and vacuum Rabi resonance in an optical cavity with one trapped atom have also been observed [48, 49]. Another proposal to reach the strong coupling on the single-photon level is a collective interaction. In a N two-level atoms system, the photon-atom coupling can be enhanced by a factor $\sqrt{N}$. This collective strong coupling recently has been realised in many systems, such as the collective strong coupling with ion Coulomb crystals [50], the observation of coherent many-body Rabi oscillations [51] and the observation of collective excition of two individual atoms [52]. For x-rays, strong coupling has not been achieved yet due to the lack of high-quality cavities. In Chapter 6 we theoretically investigate the collective strong coupling between a ^{57}Fe nuclear ensemble and single x-ray photons in a coupled-cavities system. Our results show that Rabi oscillations of single x-ray photons can be observed. Moreover, we also investigate the collective strong coupling between two ^{57}Fe nuclear ensembles in the thin-film cavity and predict a pseudo-Rabi splitting of the nuclear resonance line. The latter findings are confirmed by preliminary experimental data.

Figure 1.1 shows the electromagnetic spectrum from radio waves to γ-ray. One may envisage that each electromagnetic wave domain can represent a period of humanity's modern history. For example, the microwave region represents the time from 1860s to 1960s. During this period, the microwaves were discovered and were used for many applications, ranging well into today. Today, we enter the age of x-rays, and expect their new applications to flourish.

Chapter 2

Collective effects in single photon superradiance

In 1954, Robert Dicke presented the concept of superradiance describing the collective spontaneous emission of a single photon from a cloud of atoms [7]. Dicke pointed out that a single photon of wavelength λ stored uniformly in an atomic cloud of size $R \ll \lambda$ is emitted spontaneously with a rate $N\gamma$, where γ is the single atom decay rate and N is the number of the atoms. This is because the atoms are coherently radiating light in phase with each other, and the constructive interferences between the scattered waves lead to superradiance [53]. The atoms act like one big atom and decay collectively, a feature which has been observed in many experiments [11, 54–58].

Another fascinating aspect of single photon superradiance is the collective Lamb shift [8–11, 59, 60]. The Lamb shift [61–66] was first observed in 1947 by Willis Lamb in the experiment on the hydrogen microwave spectrum [61] and this measurement provided the stimulus for renormalized quantum electrodynamics and quantum field theory. To a certain extent the Lamb shift is also related to the process of spontaneous decay. An atom jumps from the excited state to the ground state and emits a real photon which is the spontaneous radiation. It is also possible that the atom radiates a virtual photon and jumps from the ground state to the excited state, followed quickly by the reverse process [10]. These virtual processes cause a energy shift of the levels which is a part of the Lamb shift [10]. We remember that the spontaneous emission rate is enhanced if we consider a N two-level system interacting with an electromagnetic field instead of one atom [7, 58]. Does the Lamb shift also change in such a N two-level system? In this case, a virtual photon emitted by one atom may be reabsorbed by another atom within the ensemble. The atom-atom interaction connecting the emission and reabsorption of the virtual photon results in the variation of Lamb shift, which is called the collective Lamb shift.

In this Chapter, we start by introducing the theoretical model developed in Ref. [67] to describe the collective emission of a single photon from a cloud of two-level atoms. This problem is simplified to find eigenfunctions and eigenvalues of an integral equation. The superradiance decay rate and the collective Lamb shift are given in an exact analytical solution. We then we extend this model to study the case in which there is a magnetic field applied to the atoms. The excited and ground states are split and two resonant transitions have been taken into account. We derive the eigenfunctions and eigenvalues of this effective N four-level atoms

system and give an analytical expression for the single-photon radiation spectrum. We find that surprisingly an additional collective contribution appears under the action of the external magnetic field, which leads to characteristic single-photon radiation spectra. For instance, in some cases the energy gap between the two resonant transitions is no longer the same as the traditional Zeeman splitting of a single atom. The collective effects can broaden the gap. We also find that for a certain parameter domain, the shape of the splitting resembles an EIT-like spectrum for a single photon. Instead of two independent peaks, a transparency window appears in the radiation spectrum and this will have many applications in x-ray quantum optics.

2.1 Theoretical model for collective emission of two-level atoms

In this Section we mainly follow the model presented in Ref. [67]. In that paper, the problem of a single photon cooperative spontaneous emission from a cloud of N two-level atoms [one excited, $(N-1)$ in the ground state] has been studied in detail. In particular, an exact analytical solution of this many-atom problem for a spherically symmetric two-level atomic cloud is found. We reproduce here the expressions for superradiance and the collective Lamb shift yielded by the virtual processes.

2.1.1 Derivation of eigenvalue equation

We consider a system of N two level atoms and the resonant energy is $\hbar\omega_0$. Initially one of the atoms is in the excited state and there no photons are present. Atoms are located at positions $\vec{r}_j$ $(j = 1, ..., N)$. In the dipole approximation the interaction between the atoms and the photons is described by the Hamiltonian in the interaction picture

$$H_{int} = \sum_{\vec{k}} \sum_{j=1}^{N} g_k (\hat{\sigma}_j e^{-i\omega_0 t} + \hat{\sigma}_j^+ e^{i\omega_0 t})(\hat{a}_{\vec{k}}^+ e^{i\nu_k t - i\vec{k}\cdot\vec{r}_j} + \hat{a}_{\vec{k}} e^{-i\nu_k t + i\vec{k}\cdot\vec{r}_j}) \,, \tag{2.1}$$

where $\hat{\sigma}_j$ is the lowering operator for atom j, $\hat{a}_{\vec{k}}$ $\left(\hat{a}_{\vec{k}}^+\right)$ is the photon annihilation (creation) operator, ν_k is the frequency of photon, and g_k is the atom-photon coupling constant for the $\vec{k}$ mode

$$g_k = \omega_0 \frac{\Omega}{\hbar} \sqrt{\frac{\hbar}{\epsilon_0 \nu_k V_{ph}}} \,, \tag{2.2}$$

where Ω is the electric-dipole transition matrix element and V_{ph} is the photon volume.

We do not make the rotating wave approximation in Eq. (2.1). The part of the Hamiltonian omitted in the rotating wave approximation plays an important role for the virtual processes. We try to find a solution of the Schrödinger equation for

the atoms and the field as a superposition of the Fock states

$$|\psi\rangle = \sum_{j=1}^{N} \beta_j(t)|g_1 g_2 ... e_j ... g_N\rangle|0\rangle + \sum_{\vec{k}} \gamma_{\vec{k}}(t)|g_1 g_2 ... g_N\rangle|1_{\vec{k}}\rangle$$

$$+ \sum_{m<n} \sum_{\vec{k}} \alpha_{mn,\vec{k}}(t)|g_1 g_2 ... e_m, ... e_n, ... g_N\rangle|1_{\vec{k}}\rangle\,, \tag{2.3}$$

where $\alpha_{mn,\vec{k}} = \alpha_{nm,\vec{k}}$. In the first sum there is no photon in the states, while in the second sum the photon occupation number is equal to one and all atoms are in the ground state. The last term corresponds to the presence of two excited atoms and one virtual photon with "negative" energy.

We adopt $\hbar = 1$ and then the Schrödinger equation can be written as

$$|\dot{\psi}(t)\rangle = -iH_{int}|\psi(t)\rangle\,. \tag{2.4}$$

Substituting Eq. (2.1) and Eq. (2.3) into Eq. (2.4) yields the following equations

$$\frac{\partial \beta_j}{\partial t} = -i \sum_{\vec{k}} g_k \gamma_{\vec{k}}(t) e^{-i(\nu_k - \omega_0)t + i\vec{k}\cdot\vec{r}_j}$$

$$- i \sum_{\vec{k}} g_k \sum_{j' \neq j, j'=1}^{N} \alpha_{jj',\vec{k}} e^{-(\nu_k + \omega_0)t + i\vec{k}\cdot\vec{r}_{j'}}\,, \tag{2.5}$$

$$\frac{\partial \gamma_{\vec{k}}}{\partial t} = -ig_k \sum_{j=1}^{N} \beta_j(t) e^{i(\nu_k - \omega_0)t - i\vec{k}\cdot\vec{r}_j}\,, \tag{2.6}$$

$$\frac{\partial \alpha_{mn,\vec{k}}}{\partial t} = -ig_k \beta_n(t) e^{i(\nu_k + \omega_0)t - i\vec{k}\cdot\vec{r}_m} - ig_k \beta_m(t) e^{i(\nu_k + \omega_0)t - i\vec{k}\cdot\vec{r}_n}\,. \tag{2.7}$$

Integrating Eq. (2.6) and Eq. (2.7) over time with initial conditions $\gamma_{\vec{k}}(0) = 0,\ \alpha_{mn,\vec{k}}(0) = 0$, we obtain

$$\gamma_{\vec{k}}(t) = -ig_k \int_0^t dt' \sum_{j=1}^{N} \beta_j(t') e^{i(\nu_k - \omega_0)t' - i\vec{k}\cdot\vec{r}_j}\,, \tag{2.8}$$

$$\alpha_{mn,\vec{k}}(t) = -ig_k \int_0^t dt' [\beta_n(t') e^{i(\nu_k + \omega_0)t' - i\vec{k}\cdot\vec{r}_m} + \beta_m(t') e^{i(\nu_k + \omega_0)t' - i\vec{k}\cdot\vec{r}_n}]\,, \tag{2.9}$$

and substituting $\gamma_{\vec{k}}(t)$ and $\alpha_{mn,\vec{k}}(t)$ into Eq. (2.5) , we get an equation for $\beta_j(t)$

$$\frac{\partial \beta_j(t)}{\partial t} = -\sum_{\vec{k}} \sum_{j'=1}^{N} \int_0^t dt' g_k^2 \beta_{j'}(t') e^{i(\nu_k - \omega_0)(t'-t) + i\vec{k}\cdot(\vec{r}_j - \vec{r}_{j'})}$$

$$- (N-1) \sum_{\vec{k}} \int_0^t dt' g_k^2 \beta_j(t') e^{i(\nu_k + \omega_0)(t'-t)}$$

$$-\sum_{\vec{k}}\sum_{j'=1,j'\neq j}^{N}\int_0^t dt' g_k^2\beta_{j'}(t')e^{i(\nu_k+\omega_0)(t'-t)-i\vec{k}\cdot(\vec{r}_j-\vec{r}_{j'})}\,. \tag{2.10}$$

We make the Markovian approximation (slow decay) and replace $\beta_j(t') = \beta_j(t)$ under the integral in Eq. (2.10). This approximation is valid provided the state decay time is larger than the time of the photon flight through the atomic cloud. We perform the integration by taking the remaining integral over t' and replacing summation over $\vec{k}$. We then obtain

$$\begin{aligned}\frac{\partial\beta_j(t)}{\partial t} =&\frac{iV_{ph}}{(2\pi)^3}\beta_j(t)\int d^3\vec{k}g_k^2\left(\frac{1-e^{-i(\nu_k-\omega_0)t}}{\nu_k-\omega_0}\right)\\ &+(N-1)\frac{iV_{ph}}{(2\pi)^3}\beta_j(t)\int d^3\vec{k}g_k^2\left(\frac{1-e^{-i(\nu_k+\omega_0)t}}{\nu_k+\omega_0}\right)\\ &+\frac{iV_{ph}}{(2\pi)^3}\int d^3\vec{k}g_k^2\sum_{j'=1,j'\neq j}^{N}\left(\frac{1-e^{-i(\nu_k-\omega_0)t}}{\nu_k-\omega_0}\right)e^{i\vec{k}\cdot(\vec{r}_j-\vec{r}_{j'})}\beta_{j'}(t)\\ &+\frac{iV_{ph}}{(2\pi)^3}\int d^3\vec{k}g_k^2\sum_{j'=1,j'\neq j}^{N}\left(\frac{1-e^{-i(\nu_k+\omega_0)t}}{\nu_k+\omega_0}\right)e^{-i\vec{k}\cdot(\vec{r}_j-\vec{r}_{j'})}\beta_{j'}(t)\,.\end{aligned} \tag{2.11}$$

Integrating over all possible directions of $\vec{k}$ gives

$$\begin{aligned}\frac{\partial\beta_j(t)}{\partial t} =&\frac{iV_{ph}}{2\pi^2c}\beta_j(t)\int_0^\infty dkk^2g_k^2\left(\frac{1-e^{-ic(k-k_0)t}}{k-k_0}\right)\\ &+(N-1)\frac{iV_{ph}}{2\pi^2c}\beta_j(t)\int_0^\infty dkk^2g_k^2\left(\frac{1-e^{-ic(k+k_0)t}}{k+k_0}\right)\\ &+\frac{iV_{ph}}{2\pi^2c}\int_0^\infty dkk^2g_k^2\sum_{j'\neq j}^{N}\left(\frac{1-e^{-ic(k-k_0)t}}{k-k_0}\right)\frac{\sin(k|\vec{r}_j-\vec{r}_{j'}|)}{k|r_j-r_{j'}|}\beta_{j'}(t)\\ &+\frac{iV_{ph}}{2\pi^2c}\int_0^\infty dkk^2g_k^2\sum_{j'\neq j}^{N}\left(\frac{1-e^{-ic(k+k_0)t}}{k+k_0}\right)\frac{\sin(k|\vec{r}_j-\vec{r}_{j'}|)}{k|\vec{r}_j-\vec{r}_{j'}|}\beta_{j'}(t)\,,\end{aligned} \tag{2.12}$$

where $k = \nu_k/c$, $k_0 = \omega_0/c$. Next we replace k_0 by $k_0 + i0$. We disregard the exponential factors containing t because they oscillate very fast under integration over k. Then we find

$$\begin{aligned}\frac{\partial\beta_j(t)}{\partial t} =&\frac{iV_{ph}}{2\pi^2c}\beta_j(t)\int_0^\infty dkk^2g_k^2\left(\frac{1}{k-k_0-i0}\right)\\ &+(N-1)\frac{iV_{ph}}{2\pi^2c}\beta_j(t)\int_0^\infty dkk^2g_k^2\left(\frac{1}{k+k_0+i0}\right)\end{aligned}$$

$$+\frac{iV_{ph}}{2\pi^2 c}\int_0^\infty dk k^2 g_k^2 \sum_{j'\neq j}^{N}\left(\frac{1}{k-k_0-i0}\right)\frac{\sin(k|\vec{r}_j-\vec{r}_{j'}|)}{k|\vec{r}_j-\vec{r}_{j'}|}\beta_{j'}(t)$$

$$+\frac{iV_{ph}}{2\pi^2 c}\int_0^\infty dk k^2 g_k^2 \sum_{j'\neq j}^{N}\left(\frac{1}{k+k_0+i0}\right)\frac{\sin(k|\vec{r}_j-\vec{r}_{j'}|)}{k|\vec{r}_j-\vec{r}_{j'}|}\beta_{j'}(t)\,. \tag{2.13}$$

We now may rewrite the first two terms in Eq. (2.13) using the relation $\frac{1}{x\mp i0} = \mathcal{P}\left(\frac{1}{x}\right) \pm i\pi\delta(x)$, where $\mathcal{P}$ stands for the Cauchy principle part. Then we obtain

$$\begin{aligned}\frac{\partial\beta_j(t)}{\partial t} =& \frac{i\gamma}{\pi k_0}\beta_j(t)\int_0^\infty dk k\left(\mathcal{P}\left(\frac{1}{k-k_0}\right)+i\pi\delta(k-k_0)\right)\\ &+\frac{i\gamma}{\pi k_0}(N-1)\beta_j(t)\int_0^\infty dk k\left(\mathcal{P}\left(\frac{1}{k+k_0}\right)-i\pi\delta(k+k_0)\right)\\ &+\frac{i\gamma}{\pi k_0}\sum_{j'\neq j}^{N}\int_0^\infty dk\left[\frac{1}{k-k_0-i0}+\frac{1}{k+k_0+i0}\right]\frac{\sin(k|\vec{r}_j-\vec{r}_{j'}|)}{k|\vec{r}_j-\vec{r}_{j'}|}\beta_{j'}(t)\,,\end{aligned} \tag{2.14}$$

where $\gamma = (k_0^3\Omega^2)/(2\pi\epsilon_0\hbar)$ is the spontaneous decay rate for the single atom. We transform the integral over dk in the last term into an integral from $-\infty$ to ∞ as

$$\begin{aligned}&\int_0^\infty dk\left[\frac{1}{k-k_0-i0}+\frac{1}{k+k_0+i0}\right]\sin(k|\vec{r}_j-\vec{r}_{j'}|)\\ &=\int_{-\infty}^{\infty}dk\frac{\sin(k|\vec{r}_j-\vec{r}_{j'}|)}{k-k_0-i0}\\ &=\frac{1}{2i}\int_{-\infty}^{\infty}dk\left(\frac{\exp(ik|\vec{r}_j-\vec{r}_{j'}|)}{k-k_0-i0}-\frac{\exp(-ik|\vec{r}_j-\vec{r}_{j'}|)}{k-k_0-i0}\right).\end{aligned} \tag{2.15}$$

In order to calculate the integration, we use the contour method. For the first term we close the integration contour in the upper half-plane of complex k, while for the second term in the lower half-plane. Then we find the integration of the second term is zero and obtain

$$\begin{aligned}\frac{\partial\beta_j(t)}{\partial t} =& \frac{i\gamma}{\pi k_0}\beta_j(t)\int_0^\infty dk k\left(\mathcal{P}\left(\frac{1}{k-k_0}\right)+\mathcal{P}\left(\frac{N-1}{k+k_0}\right)\right)\\ &-\gamma\beta_j(t)+i\gamma\sum_{j\neq j'}^{N}\frac{\exp(ik_0|\vec{r}_j-\vec{r}_{j'}|)}{k_0|\vec{r}_j-\vec{r}_{j'}|}\beta_{j'}(t)\,.\end{aligned} \tag{2.16}$$

The first term is the same for all $\beta_j(t)$ and corresponds to a frequency shift. We neglect the constant shift and obtain

$$\frac{\partial\beta_j(t)}{\partial t} = -\gamma\beta_j(t)+i\gamma\sum_{j\neq j'}\frac{\exp(ik_0|\vec{r}_j-\vec{r}_{j'}|)}{k_0|\vec{r}_j-\vec{r}_{j'}|}\beta_{j'}(t)\,. \tag{2.17}$$

We assume that the system is initially prepared in an eigenstate and the state decays exponentially, i.e.,

$$\beta_j(t) = \beta_j e^{-\lambda_n t}\,, \tag{2.18}$$

where $Re(\lambda_n) > 0$. Substituting Eq. (2.18) into Eq. (2.17) finally yields the eigenvalue equation

$$\lambda_n \beta_j = \gamma\beta_j - i\gamma \sum_{j'\neq j} \frac{\exp(ik_0|\vec{r}_j - \vec{r}_{j'}|)}{k_0|\vec{r}_j - \vec{r}_{j'}|}\beta_{j'}\,. \tag{2.19}$$

Next we will present an analytical solution of the eigenvalue equation for a dense cloud.

2.1.2 Derivation of the superradiance decay rate and collective Lamb shift

Here we consider a dense cloud such that there are many atoms in volume λ^3, and we may replace the summation by integration. The eigenvalue equation (2.19) reads

$$-i\gamma\frac{N}{V}\int d\vec{r}\,'\frac{\exp(ik_0|\vec{r}-\vec{r}\,'|)}{k_0|\vec{r}-\vec{r}\,'|}\beta(\vec{r}\,') = \lambda_n\beta(\vec{r})\,. \tag{2.20}$$

We assume that the atoms are uniformly distributed in a sphere of volume $V = 4\pi R^3/3$ and N/V is the atomic density. The imaginary part of the kernel $i\exp(ik_0|\vec{r}_j - \vec{r}_{j'}|)/(k_0|\vec{r}_j - \vec{r}_{j'}|)$ is induced by the virtual photons which correspond to $\mathrm{Im}(\lambda_n)$. $\mathrm{Im}(\lambda_n)$ yields the frequency shift and $\mathrm{Re}(\lambda_n)$ describes the decay rate of the eigenstate.

In order to obtain the solution of Eq. (2.20), we take into account that the exponential kernel coincides with the retarded Green's function $G^R(\vec{r}-\vec{r}\,')$ of the Helmholtz equation

$$(\Delta + k_0^2)G^R(\vec{r}-\vec{r}\,') = -\delta(\vec{r}-\vec{r}\,')\,, \tag{2.21}$$

where

$$G^R(\vec{r}-\vec{r}\,') = \frac{\exp(ik_0|\vec{r}-\vec{r}\,'|)}{4\pi|\vec{r}-\vec{r}\,'|}. \tag{2.22}$$

Operating $(\Delta + k_0^2)$ to both sides of Eq. (2.20) we obtain

$$\lambda_n(\bigtriangledown^2 + k_0^2)\beta(\vec{r}) = \frac{i4\pi N\gamma}{k_0 V}\beta(\vec{r})\,, \tag{2.23}$$

which can be written in the form

$$\Delta\beta(\vec{r}) + a^2k_0^2\beta(\vec{r}) = 0\,, \tag{2.24}$$

where

$$a^2 = 1 - \frac{3iN\gamma}{\lambda_n(k_0R)^3}\,. \tag{2.25}$$

The solutions of the Helmholtz equation (2.24) for our spherically symmetric problem are chosen in the form

$$\beta(\vec{r}) = j_n(ak_0r)Y_{nm}(\hat{r})\,, \tag{2.26}$$

where $Y_{nm}(\hat{r}) \equiv Y_{nm}(\theta,\varphi)$ are spherical harmonics. In order to obtain the eigenvalues λ_n, first we need to find the parameter a. We expand the Green function in the form

$$\frac{\exp(ik_0|\vec{r}-\vec{r}\,'|)}{4\pi|\vec{r}-\vec{r}\,'|} = 4\pi i\sum_{k=0}^{\infty}\sum_{s=-k}^{k} Y_{ks}(\hat{r})Y^*_{ks}(\hat{r}')\begin{cases} j_k(k_0r')h_k^{(1)}(k_0r), & r>r' \\ j_k(k_0r)h_k^{(1)}(k_0r'), & r\le r' \end{cases}, \tag{2.27}$$

where $\hat{r}$ and $\hat{r}'$ are unit vectors in the directions of $\vec{r}$ and $\vec{r}\,'$, respectively. The spherical Bessel functions $j_k(z)$ and $h_k^{(1)}$ are written as

$$j_k(z) \approx \frac{\sqrt{\pi}}{(2k+1)\Gamma(k+1/2)}\left(\frac{z}{2}\right)^2,$$

$$h_k^{(1)}(z) \approx -i\frac{\Gamma(k+1/2)}{2\sqrt{\pi}}\left(\frac{2}{z}\right)^{k+1},\ z\to 0. \tag{2.28}$$

If we multiply both sides of Eq. (2.27) by k_0 and then take the limit $k_0 \to 0$, we obtain an expansion for the Coulomb potential

$$\frac{1}{|r-r'|} = 4\pi\sum_{k=0}^{\infty}\sum_{s=-k}^{k} Y_{ks}(\hat{r})Y^*_{ks}(\hat{r}')\frac{1}{2k+1}\begin{cases} r'^k r^{-k+1}, & r>r' \\ r^k r'^{-k+1}, & r\le r' \end{cases}. \tag{2.29}$$

Substituting Eqs. (2.26) and (2.27) into Eq. (2.20) we obtain

$$4\pi\gamma\frac{N}{V}\int dr' j_n(ak_0r')Y_{nm}(\hat{r}')\sum_{k=0}^{\infty}\sum_{s=-k}^{k} Y_{ks}(\hat{r})Y^*_{ks}(\hat{r}')\begin{cases} j_k(k_0r')h_k^{(1)}(k_0r), & r>r' \\ j_k(k_0r)h_k^{(1)}(k_0r'), & r\le r' \end{cases}$$

$$= \lambda_n j_n(ak_0r)Y_{nm}(\hat{r})\,. \tag{2.30}$$

Using the orthogonality condition for spherical harmonics we can perform an integration over the $\vec{r}\,'$ direction

$$\int d\Omega_{r'} Y^*_{ls}(\hat{r}')Y_{nm}(\hat{r}') = \delta_{nl}\delta_{sm} \tag{2.31}$$

which yields

$$4\pi\gamma\frac{N}{V}\int_0^R dr' r'^2 j_n(ak_0r')\begin{cases} j_n(k_0r')h_n^{(1)}(k_0r), & r>r' \\ j_n(k_0r)h_n^{(1)}(k_0r'), & r\le r' \end{cases} = \lambda_n j_n(ak_0r)\,. \tag{2.32}$$

We then rewrite Eq. (2.32) as

$$\int_0^{k_0R} dx' x'^2 j_n(ax')\begin{cases} j_n(k_0r')h_n^{(1)}(xr), & x>x' \\ j_n(k_0r)h_n^{(1)}(x'), & x\le x' \end{cases} = \lambda'_n j_n(ax)\,, \tag{2.33}$$

where $x(x') = k_0 r(r')$ and

$$\lambda_n' = \frac{k_0^3 V}{4\pi N}\lambda_n = \frac{k_0^3 R^3}{3N}\lambda_n \,. \tag{2.34}$$

Next we calculate the integral in Eq. (2.33) using

$$\int dx x^2 j_n(ax) j_n(x) = \frac{x^2}{1-a^2}\left[a j_n(x) j_{n-1}(ax) - j_{n-1}(x) j_n ax\right] , \tag{2.35}$$

$$\int dx x^2 j_n(ax) h_n^{(1)}(x) = \frac{x^2}{1-a^2}\left[a h_n^{(1)}(x) j_{n-1}(ax) - h_{n-1}^{(1)}(x) j_n ax\right] , \tag{2.36}$$

and the identity

$$j_n(x) h_{n-1}^{(1)}(x) - h_n^{(1)}(x) j_n(x) = \frac{i}{x^2} \,. \tag{2.37}$$

This leads to

$$\int_0^{k_0 R} dx' x'^2 j_n(ax') \left\{ \begin{array}{ll} j_n(x') h_n^{(1)}(x), & x > x' \\ j_n(x) h_n^{(1)}(x'), & x \le x' \end{array} \right. = \lambda_n' j_n(ax)$$

$$+ i(k_0 R)^2 \lambda_n' j_n(x)\left[a h_n^{(1)}(k_0 R) j_{n-1}(a k_0 R) - h_{n-1}^{(1)}(k_0 R) j_n(a k_0 R)\right] . \tag{2.38}$$

The integral equation (2.20) is satisfied provided the last term in Eq. (2.38) equals zero. This yields the solution for the eigenvalues

$$a = \frac{j_n(a k_0 R)}{j_{n-1} k_0 R} \frac{h_{n-1}^{(1)}(k_0 R)}{h_n^{(1)}(k_0 R)} \,. \tag{2.39}$$

For $n = 0$

$$j_0(x) = \frac{\sin(x)}{x} \,, \quad j_{-1}(x) = \frac{\cos(x)}{x} \,, \tag{2.40}$$

$$h_0^{(1)}(x) = \frac{e^{ix}}{ix} \,, \quad h_{-1}^{(1)}(x) = \frac{e^{ix}}{x} \,, \tag{2.41}$$

and we can simplify Eq. (2.39) to

$$a = i \tan(a k_0 R) \,. \tag{2.42}$$

In the following we take into account the two limiting cases of small and large atomic cloud. First in the limit $k_0 R \ll 1$ we have

$$\frac{h_{n-1}^{(1)}(k_0 R)}{h_n^{(1)}(k_0 R)} \approx i \frac{(k_0 R)^{2n}}{[(2n-1)!!]^2} + \left\{ \begin{array}{ll} 0, & n = 0 \\ \frac{k_0 R}{2n-1}, & n > 0 \end{array} \right. . \tag{2.43}$$

Neglecting the real part in the right hand side of Eq. (2.43) we obtain

$$a j_{n-1}(a k_0 R) \approx i \frac{(k_0 R)^{2n}}{[(2n-1)!!]^2} j_n(a k_0 R) \,. \tag{2.44}$$

Using the identity

$$\frac{d}{dx}[xj_{n-1}(x)] = nj_{n-1}(x) - xj_n(x) \tag{2.45}$$

we expand the left hand side of Eq. (2.44) near $ak_0R = A_{nl}$, where A_{nl} is a positive zero of the Bessel function $j_{n-1}(x)$. Then we derive

$$a \approx \frac{A_{nl}}{k_0R} - i\frac{(k_0R)^2}{A_{nl}[(2n-1)!!]^2}\,, \tag{2.46}$$

which yields the corresponding eigenvalues and eigenfunctions

$$\lambda_{nl} \approx -\frac{3i\gamma N}{A_{nl}^2 k_0R} + \frac{6\gamma N(k_0R)^{2n}}{A_{nl}^4[(2n-1)!!]^2}\,, \tag{2.47}$$

$$\beta_{nlm}(\vec{r}) = j_n(A_{nl}\frac{r}{R})Y_{nm}(\hat{r})\,. \tag{2.48}$$

In particular, $A_{0l} = (2l-1)\pi/2$ and $A_{1l} = \pi l$ where $l = 1, 2, 3.....$ As we can see $\mathrm{Im}(\lambda_{nl})$ is very large for $k_0R \ll 1$. The imaginary part corresponding to the frequency shift is called collective Lamb shift [11, 60] and becomes observable in this case. In the limit $k_0R \ll 1$ only eigenvalues with $n = 0$ have a large real part, while the other eigenvalues with $n > 0$ are suppressed by a factor of $(k_0R)^{2n}$. The value of the decay rate is given by

$$\sum_{l=1}^{\infty} Re(\lambda_{0l}) = \sum_{l=1}^{\infty} \frac{6\gamma N}{A_{0l}^4} = \gamma N\,, \tag{2.49}$$

which is consistent with what was expected from Dicke's paper [7].

Now we focus on the large cloud limit $k_0R \gg n$. In this case we consider the asymptotics of the Bessel functions in Eq. (2.39) ($z \gg n$)

$$j_n(z) \approx \frac{1}{z}\sin\left(z - \frac{n}{2}\pi\right)\,, \tag{2.50}$$

$$h_n^{(1)} \approx \frac{1}{z}(-i)^{(n+1)}e^{(iz)}\,, \tag{2.51}$$

and obtain

$$a = i\tan\left(ak_0R - \frac{n}{2}\pi\right)\,. \tag{2.52}$$

We rewrite Eq. (2.52) as

$$i\,\mathrm{arctanh}(a) = -ak_0R + \frac{n}{2}\pi + \pi l\,, \tag{2.53}$$

where l is an integer. In the logarithmic representation, $\mathrm{arctanh}(a) = \frac{1}{2}\ln\left(\frac{1+a}{1-a}\right)$. In the case $|a| \ll 1$ which yields $\mathrm{arctanh}(a) \approx a$, we obtain the solution

$$a \approx \frac{\pi(n+2l)}{2k_0R}\left(1 - \frac{i}{k_0R}\right)\,, \tag{2.54}$$

$$\lambda_n \approx \frac{3i\gamma N}{(k_0R)^3}\left(1+\frac{\pi^2(n+2l)^2}{4(k_0R)^2}\right), \tag{2.55}$$

which is valid provided $|n+2l| \ll k_0R$. For $|a| \gg 1$ we approximate $\operatorname{arctanh}(a) \approx -i\pi/2 + 1/a$ and find

$$a \approx \frac{\pi(n+2l-1)}{2k_0R} - \frac{2i}{\pi(n+2l-1)}, \tag{2.56}$$

$$\lambda_n \approx -\frac{12i\gamma N}{\pi^2(n+2l-1)^2k_0R} + \frac{96\gamma N}{\pi^4(n+2l-1)^4}, \tag{2.57}$$

which is valid if $|n+2l| \gg k_0R$.
Finally, if $|a+1| \ll 1$ we find with logarithmic accuracy

$$a \approx -1 + \frac{\pi}{2k_0R}\left(\frac{1}{2}+n+2l+\left\{\frac{2k_0R}{\pi}\right\}\right) + \frac{i}{2k_0R}\ln\left(\frac{4k_0R}{\ln(4k_0R)}\right), \tag{2.58}$$

$$\lambda_n \approx \frac{3i\gamma N}{(k_0R)^2}\left[\pi\left(\frac{1}{2}+n+2l+\left\{\frac{2k_0R}{\pi}\right\}\right) + i\ln\left(\frac{4k_0R}{\ln(4k_0R)}\right)\right]^{-1}, \tag{2.59}$$

where $\{...\}$ represents the fractional part of a number.

In summary, in this section we have presented the theoretical model of collective two-level atom states in which only one atom is excited. We obtain the analytical formulas for the eigenstates and eigenvalues of the system and discuss the results of the two limiting cases ($k_0R \ll 1$ and $k_0R \gg 1$). We have followed here the derivation in Ref. [67]. In the next section, we extend this model in order to address the more complicated situation in which there is a magnetic field applied to the atoms.

2.2 Collective spontaneous emission of N atoms with Zeeman splitting

In this Section, we study the collective effects in single photon radiation taking into account the effect of a magnetic field. We extend the model presented in Sec. 2.1 to manage the system with N multi-level atoms. Here we also assume that only one atom has been excited and we only consider for simplicity two resonant transitions. We derive the eigenfunctions and eigenvalues of the system. Particularly, we obtain an exact analytical solution of the spontaneous radiation spectrum in this situation. We discuss here several parameter regimes of interest. We find an additional collective effect occurs which leads to characteristic single-photon spectra.

2.2.1 Theoretical model

In the following we focus on the transition from the ground state to the excited state at the resonant energy of ω_0 in a large cloud of N atoms. In the absence of magnetic fields it acts as a two-level system. In the presence of a magnetic

field, the ground and excited states with spin different from zero will be split into multiplets. Here we only consider for simplicity two transitions with the resonant energies are ω_1 and ω_2, respectively. The atoms are located at positions $\vec{r}_j\,(j = 1, ..., N)$ and the number of atoms which can be driven by transition 1 is N_1. The interaction between the atoms and the photons is described by the Hamiltonian in the interaction picture

$$H_{int} = \sum_{\vec{k}} \sum_{j=1}^{N_1} g_{k,1}(\hat{\sigma}_1^j e^{-i\omega_1 t} + \hat{\sigma}_1^{j+} e^{i\omega_1 t})(\hat{a}_{\vec{k}}^+ e^{i\nu_k t - i\vec{k}\cdot\vec{r}_j} + \hat{a}_{\vec{k}} e^{-i\nu_k t + i\vec{k}\cdot\vec{r}_j})$$

$$+ \sum_{\vec{k}} \sum_{j=N_1+1}^{N} g_{k,2}(\hat{\sigma}_2^j e^{-i\omega_2 t} + \hat{\sigma}_2^{j+} e^{i\omega_2 t})(\hat{a}_{\vec{k}}^+ e^{i\nu_k t - i\vec{k}\cdot\vec{r}_j} + \hat{a}_{\vec{k}} e^{-i\nu_k t + i\vec{k}\cdot\vec{r}_j})\,, \quad (2.60)$$

where $\hat{\sigma}_{1(2)}^j$ is the lowering operator of transition 1(2) for atom j, $\hat{a}_{\vec{k}}$ $\left(\hat{a}_{\vec{k}}^+\right)$ is the photon annihilation (creation) operator, ν_k is the frequency of photon, and $g_{k,1(2)}$ is the atom-photon coupling constant for the $\vec{k}$ mode. We assume for simplicity $g_{k,1} = g_{k,2} = g_k$. Here, we do not make the rotating wave approximation in the Hamiltonian.

We look for a solution of the Schrödinger equation for the atoms and the field as a superposition of Fock states

$$|\psi\rangle = \sum_{j=1}^{N_1} \beta_1^j(t)|g_1 g_2 ... e_j ... g_{N_1} ... g_N\rangle|0\rangle$$

$$+ \sum_{j=N_1+1}^{N} \beta_2^j(t)|g_1 ... g_{N_1} g_{N_1+1} ... e_j ... g_N\rangle|0\rangle$$

$$+ \sum_{\vec{k}} \gamma_{\vec{k}}(t)|g_1 g_2 ... g_N\rangle|1_{\vec{k}}\rangle$$

$$+ \sum_{m<n\le N_1} \sum_{\vec{k}} \alpha_1^{mn,\vec{k}}(t)|g_1 ... e_m ... e_n ... g_{N_1} ... g_N\rangle|1_{\vec{k}}\rangle$$

$$+ \sum_{m\le N_1<n} \sum_{\vec{k}} \alpha_2^{mn,\vec{k}}(t)|g_1 ... e_m ... g_{N_1} ... e_n ... g_N\rangle|1_{\vec{k}}\rangle$$

$$+ \sum_{N_1<m<n} \sum_{\vec{k}} \alpha_3^{mn,\vec{k}}(t)|g_1 ... g_{N_1} ... e_m ... e_n ... g_N\rangle|1_{\vec{k}}\rangle\,, \quad (2.61)$$

where $\alpha_j^{mn,\vec{k}} = \alpha_j^{nm,\vec{k}}, j = 1, 2, 3$. States in the first two sums correspond to zero number of photons, while in the third sum the photon occupation number is equal to one and all atoms are in the ground state. The last three terms correspond to the presence of a photon with "negative" energy. This is the way how we take into account the virtual process.

We adopt $\hbar = 1$ and then the Schrödinger equation can be written as

$$|\dot{\psi}(t)\rangle = -iH_{int}|\psi(t)\rangle\,. \tag{2.62}$$

Substituting Eqs. (2.60) and (2.61) into Eq. (2.62) and we obtain the following equations

$$\begin{aligned}\frac{\partial\beta_1^j}{\partial t} =& -i\sum_{\vec{k}} g_k\gamma_{\vec{k}}(t)e^{-i(\nu_k-\omega_1)t+i\vec{k}\cdot\vec{r}_j}\\ &-i\sum_{\vec{k}} g_k\sum_{j'\neq j,j'=1}^{N_1}\alpha_1^{jj',\vec{k}}e^{-(\nu_k+\omega_1)t+i\vec{k}\cdot\vec{r}_{j'}}\\ &-i\sum_{\vec{k}} g_k\sum_{j'\neq j,j'=N_1+1}^{N}\alpha_2^{jj',\vec{k}}e^{-(\nu_k+\omega_2)t+i\vec{k}\cdot\vec{r}_{j'}}\,,\end{aligned} \tag{2.63}$$

$$\begin{aligned}\frac{\partial\beta_2^j}{\partial t} =& -i\sum_{\vec{k}} g_k\gamma_{\vec{k}}(t)e^{-i(\nu_k-\omega_2)t+i\vec{k}\cdot\vec{r}_j}\\ &-i\sum_{\vec{k}} g_k\sum_{j'\neq j,j'=N_1+1}^{N}\alpha_3^{jj',\vec{k}}e^{-(\nu_k+\omega_2)t+i\vec{k}\cdot\vec{r}_{j'}}\\ &-i\sum_{\vec{k}} g_k\sum_{j'\neq j,j'=1}^{N_1}\alpha_2^{jj',\vec{k}}e^{-(\nu_k+\omega_1)t+i\vec{k}\cdot\vec{r}_{j'}}\,,\end{aligned} \tag{2.64}$$

$$\begin{aligned}\frac{\partial\gamma_{\vec{k}}}{\partial t} =& -ig_k\sum_{j=1}^{N_1}\beta_1^j(t)e^{i(\nu_k-\omega_1)t-i\vec{k}\cdot\vec{r}_j}\\ &-ig_k\sum_{j=N_1+1}^{N}\beta_2^j(t)e^{i(\nu_k-\omega_2)t-i\vec{k}\cdot\vec{r}_j}\,,\end{aligned} \tag{2.65}$$

$$\begin{aligned}\frac{\partial\alpha_1^{mn,\vec{k}}}{\partial t} =& -ig_k\beta_1^m(t)e^{i(\nu_k+\omega_1)t-i\vec{k}\cdot\vec{r}_n}\\ &-ig_k\beta_1^n(t)e^{i(\nu_k+\omega_1)t-i\vec{k}\cdot\vec{r}_m}\,,\end{aligned} \tag{2.66}$$

$$\begin{aligned}\frac{\partial\alpha_3^{mn,\vec{k}}}{\partial t} =& -ig_k\beta_2^m(t)e^{i(\nu_k+\omega_2)t-i\vec{k}\cdot\vec{r}_n}\\ &-ig_k\beta_2^n(t)e^{i(\nu_k+\omega_2)t-i\vec{k}\cdot\vec{r}_m}\,,\end{aligned} \tag{2.67}$$

$$\frac{\partial\alpha_2^{mn,\vec{k}}}{\partial t} = -ig_k\beta_1^m(t)e^{i(\nu_k+\omega_2)t-i\vec{k}\cdot\vec{r}_n} - ig_k\beta_2^n(t)e^{i(\nu_k+\omega_1)t-i\vec{k}\cdot\vec{r}_m}\,. \tag{2.68}$$

Integrating Eqs. (2.65)∼(2.68) over time with initial conditions $\gamma_{\vec{k}}(0)=0$, $\alpha_1^{mn,\vec{k}}(0)=\alpha_2^{mn,\vec{k}}(0)=\alpha_3^{mn,\vec{k}}(0)=0$ and substituting $\gamma_{\vec{k}}(t)$ and $\alpha_j^{mn,\vec{k}}(t)\,(j=1,2,3)$ into Eq. (2.63), we obtain an equation for $\beta_1^j(t)$

$$\begin{aligned}\frac{\partial\beta_1^j(t)}{\partial t} =& -\sum_{\vec{k}}\sum_{j'=1}^{N_1}\int_0^t dt' g_k^2\beta_1^{j'}(t')e^{i(\nu_k-\omega_1)(t'-t)+i\vec{k}\cdot(\vec{r}_j-\vec{r}_{j'})}\\ &-(N_1-1)\sum_{\vec{k}}\int_0^t dt' g_k^2\beta_1^{j'}(t')e^{i(\nu_k+\omega_1)(t'-t)}\\ &-\sum_{\vec{k}}\sum_{j'=1,j'\neq j}^{N_1}\int_0^t dt' g_k^2\beta_1^{j'}(t')e^{i(\nu_k+\omega_1)(t'-t)-i\vec{k}\cdot(\vec{r}_j-\vec{r}_{j'})}\\ &-\sum_{\vec{k}}\sum_{j'=N_1+1}^{N}\int_0^t dt' g_k^2\beta_2^{j'}(t')e^{i(\nu_k-\omega_2)t'-i(\nu_k-\omega_1)t+i\vec{k}\cdot(\vec{r}_j-\vec{r}_{j'})}\\ &-(N-N_1)\sum_{\vec{k}}\int_0^t dt' g_k^2\beta_2^{j'}(t')e^{i(\nu_k+\omega_2)(t'-t)}\\ &-\sum_{\vec{k}}\sum_{j'=N_1+1}^{N}\int_0^t dt' g_k^2\beta_2^{j'}(t')e^{i(\nu_k+\omega_1)t'-i(\nu_k+\omega_2)t-i\vec{k}\cdot(\vec{r}_j-\vec{r}_{j'})}\,.\end{aligned} \tag{2.69}$$

We divide Eq. (2.69) into two parts. The first part is

$$\begin{aligned}①=& -\sum_{\vec{k}}\sum_{j'=1}^{N_1}\int_0^t dt' g_k^2\beta_1^{j'}(t')e^{i(\nu_k-\omega_1)(t'-t)+i\vec{k}\cdot(\vec{r}_j-\vec{r}_{j'})}\\ &-(N_1-1)\sum_{\vec{k}}\int_0^t dt' g_k^2\beta_1^{j'}(t')e^{i(\nu_k+\omega_1)(t'-t)}\\ &-\sum_{\vec{k}}\sum_{j'=1,j'\neq j}^{N_1}\int_0^t dt' g_k^2\beta_1^{j'}(t')e^{i(\nu_k+\omega_1)(t'-t)-i\vec{k}\cdot(\vec{r}_j-\vec{r}_{j'})}\,.\end{aligned} \tag{2.70}$$

According to the theoretical model in Sec. 2.1 which was originally developed in Ref. [67], we know that

$$①=-\gamma\beta_1^j(t)+i\gamma\sum_{j'\neq j,j'=1}^{N_1}\frac{\exp(k_0|r_j-r_{j'}|)}{k_0|\vec{r}_j-\vec{r}_{j'}|}\beta_1^{j'}(t)\,, \tag{2.71}$$

where $k_0 = \frac{\omega_1+\omega_2}{2c}$, c is the velocity of the light in the vacuum. The second part of Eq. (2.69)

$$\begin{aligned}
② = &- \sum_{\vec{k}} \sum_{j'=N_1+1}^{N} \int_0^t dt' g_k^2 \beta_2^{j'}(t') e^{i(\nu_k-\omega_2)t' - i(\nu_k-\omega_1)t + i\vec{k}\cdot(\vec{r}_j - \vec{r}_{j'})} \\
&- (N-N_1) \sum_{\vec{k}} \int_0^t dt' g_k^2 \beta_2^{j'}(t') e^{i(\nu_k+\omega_2)(t'-t)} \\
&- \sum_{\vec{k}} \sum_{j'=N_1+1}^{N} \int_0^t dt' g_k^2 \beta_2^{j'}(t') e^{i(\nu_k+\omega_1)t' - i(\nu_k+\omega_2)t - i\vec{k}\cdot(\vec{r}_j - \vec{r}_{j'})} \,. \qquad (2.72)
\end{aligned}$$

Assuming $e^{i(\omega_1-\omega_2)t'} \simeq e^{i(\omega_1-\omega_2)t}$ which is justified provided the decay time of the state is much larger than the time of photon flight through the atomic cloud, we derive

$$② = i\gamma e^{i\phi t} \sum_{j'=N_1+1}^{N} \frac{\exp(ik_0|\vec{r}_j - \vec{r}_{j'}|)}{k_0|\vec{r}_j - \vec{r}_{j'}|} \beta_2^{j'}(t) \,, \qquad (2.73)$$

where $\phi = \omega_1 - \omega_2$.

Then we obtain

$$\begin{aligned}
\frac{\partial \beta_1^j(t)}{\partial t} = &- \gamma \beta_1^j(t) + i\gamma \sum_{j'\neq j, j'=1}^{N_1} \frac{\exp(ik_0|\vec{r}_j - \vec{r}_{j'}|)}{k_0|\vec{r}_j - \vec{r}_{j'}|} \beta_1^{j'}(t) \\
&+ i\gamma e^{i\phi t} \sum_{j'=N_1+1}^{N} \frac{\exp(ik_0|\vec{r}_j - \vec{r}_{j'}|)}{k_0|\vec{r}_j - \vec{r}_{j'}|} \beta_2^{j'}(t) \,. \qquad (2.74)
\end{aligned}$$

We do a similar simplification for $\beta_2^j(t)$ and derive

$$\begin{aligned}
\frac{\partial \beta_2^j(t)}{\partial t} = &- \gamma \beta_2^j(t) + i\gamma \sum_{j'\neq j,, j'=N_1+1}^{N} \frac{\exp(ik_0|\vec{r}_j - \vec{r}_{j'}|)}{k_0|\vec{r}_j - \vec{r}_{j'}|} \beta_2^{j'}(t) \\
&+ i\gamma e^{-i\phi t} \sum_{j'=1}^{N_1} \frac{\exp(ik_0|\vec{r}_j - \vec{r}_{j'}|)}{k_0|\vec{r}_j - \vec{r}_{j'}|} \beta_1^{j'}(t) \,. \qquad (2.75)
\end{aligned}$$

Next we assume that initially the system is prepared in an eigenstate, that is

$$\beta_1^j(t) = \beta_1^j e^{(-\lambda_n + \frac{i}{2}\phi)t}, \;\; \beta_2^j(t) = \beta_2^j e^{(-\lambda_n - \frac{i}{2}\phi)t} \,, \qquad (2.76)$$

where λ_n is the eigenvalue and $\mathrm{Re}(\lambda_n) > 0$. Substituting Eq. (2.76) into Eqs. (2.74) and (2.75) yields the following eigenvalue equation:

$$\left(-\lambda_n + \frac{i}{2}\phi\right) \beta_1^j = - \gamma \beta_1^j + i\gamma \sum_{j'\neq j, j'=1}^{N_1} \frac{\exp(ik_0|\vec{r}_j - \vec{r}_{j'}|)}{k_0|\vec{r}_j - \vec{r}_{j'}|} \beta_1^{j'}$$

$$+ i\gamma \sum_{j'=N_1+1}^{N} \frac{\exp(ik_0|\vec{r}_j - \vec{r}_{j'}|)}{k_0|\vec{r}_j - \vec{r}_{j'}|}\beta_2^{j'} , \tag{2.77}$$

$$\left(-\lambda_n - \frac{i}{2}\phi\right)\beta_2^j = -\gamma\beta_2^j + i\gamma \sum_{j'\neq j,,j'=N_1+1}^{N} \frac{\exp(ik_0|\vec{r}_j - \vec{r}_{j'}|)}{k_0|\vec{r}_j - \vec{r}_{j'}|}\beta_2^{j'}$$

$$+ i\gamma \sum_{j'=1}^{N_1} \frac{\exp(ik_0|\vec{r}_j - \vec{r}_{j'}|)}{k_0|\vec{r}_j - \vec{r}_{j'}|}\beta_1^{j'} . \tag{2.78}$$

For a dense cloud in which there are many atoms in volume $\lambda^3\,(\lambda = 2\pi c/\omega_0)$ one can go to the continuous limit and replace summation over j' by integration. We should notice that in the summation we divide the atoms into two "teams" depending on the transitions. If we want to replace the summation by integration, the integration should be performed over the whole sample volume. Actually, the atoms of the two "teams" are distributed across the entire sample volume, but their densities are reduced by a factor $1/2$ if we consider $N_1 \approx N/2$. Based on this, the eigenvalue equations (2.77) and (2.78) read

$$\left(-\lambda_n + \frac{i}{2}\phi\right)\beta_1^j = -\gamma\beta_1^j + \frac{i}{2}\gamma \sum_{j'\neq j,j'=1}^{N} \frac{\exp(ik_0|\vec{r}_j - \vec{r}_{j'}|)}{k_0|\vec{r}_j - \vec{r}_{j'}|}\beta_1^{j'}$$

$$+ \frac{i}{2}\gamma \sum_{j'\neq j,j'=1}^{N} \frac{\exp(ik_0|\vec{r}_j - \vec{r}_{j'}|)}{k_0|\vec{r}_j - \vec{r}_{j'}|}\beta_2^{j'} , \tag{2.79}$$

$$\left(-\lambda_n - \frac{i}{2}\phi\right)\beta_2^j = -\gamma\beta_2^j + \frac{i}{2}\gamma \sum_{j'\neq j,j'=1}^{N} \frac{\exp(ik_0|\vec{r}_j - \vec{r}_{j'}|)}{k_0|\vec{r}_j - \vec{r}_{j'}|}\beta_2^{j'}$$

$$+ \frac{i}{2}\gamma \sum_{j'\neq j,j'=1}^{N} \frac{\exp(ik_0|\vec{r}_j - \vec{r}_{j'}|)}{k_0|\vec{r}_j - \vec{r}_{j'}|}\beta_1^{j'} . \tag{2.80}$$

By replacing the summations in the eigenvalue equations (2.77) and (2.78), we obtain the eigenvalue equations in a integral form

$$\left(-\lambda_n + \frac{i}{2}\phi\right)\beta_1(\vec{r}) = -\frac{\gamma}{2}\beta_1(\vec{r}) + i\gamma\int \frac{\exp(ik_0|\vec{r} - \vec{r}'|)}{k_0|\vec{r} - \vec{r}'|}\beta_1(\vec{r}')\rho_1(\vec{r}')d\vec{r}$$

$$+ \frac{\gamma}{2}\beta_2(\vec{r}) + i\gamma\int \frac{\exp(ik_0|\vec{r} - \vec{r}'|)}{k_0|\vec{r} - \vec{r}'|}\beta_2(\vec{r}')\rho_2(\vec{r}')d\vec{r}, \tag{2.81}$$

$$\left(-\lambda_n - \frac{i}{2}\phi\right)\beta_2(\vec{r}) = -\frac{\gamma}{2}\beta_2(\vec{r}) + i\gamma\int \frac{\exp(ik_0|\vec{r} - \vec{r}'|)}{k_0|\vec{r} - \vec{r}'|}\beta_2(\vec{r}')\rho_2(\vec{r}')d\vec{r}$$

$$+\frac{\gamma}{2}\beta_1(\vec{r})+i\gamma\int\frac{\exp(ik_0|\vec{r}-\vec{r}\,'|)}{k_0|\vec{r}-\vec{r}\,'|}\beta_1(\vec{r}\,')\rho_1(\vec{r}\,')d\vec{r}\,, \quad (2.82)$$

where $\rho_1(r)=\rho_2(r)=\frac{N}{2V}$.

Next we simplify the eigenvalue equations (2.81) and (2.82) and obtain

$$\frac{i}{2}\phi\left[\beta_1(\vec{r})+\beta_2(\vec{r})\right]=(\lambda_n-\gamma)\left[\beta_1(\vec{r})-\beta_2(\vec{r})\right]\,, \quad (2.83)$$

$$\left(\lambda_n+\frac{\phi^2}{4(\lambda_n-\gamma)}\right)\left[\beta_1(\vec{r})+\beta_2(\vec{r})\right]=-i\gamma\frac{N}{V}$$
$$\times\int\frac{\exp(ik_0|\vec{r}-\vec{r}\,'|)}{k_0|\vec{r}-\vec{r}\,'|}\left[\beta_1(\vec{r}\,')+\beta_2(\vec{r}\,')\right]d\vec{r}\,'\,. \quad (2.84)$$

We introduce the notations

$$\beta(\vec{r})=\beta_1(\vec{r})+\beta_2(\vec{r})\,, \quad (2.85)$$

and

$$\lambda_n'=\lambda_n+\frac{\phi^2}{4(\lambda_n-\gamma)}\,. \quad (2.86)$$

Substituting Eqs. (2.85) and (2.86) into Eq. (2.84) yields

$$\lambda_n'\beta(\vec{r})=-i\gamma\frac{N}{V}\int d\vec{r}\,'\frac{\exp(ik_0|\vec{r}-\vec{r}\,'|)}{k_0|\vec{r}-\vec{r}\,'|}\beta(\vec{r}\,')\,. \quad (2.87)$$

We find that Eq. (2.87) is the same as the eigenvalue equation (2.20) in the two-level system if we substitute λ_n with λ_n' in eigenvalue equation (2.20). In Sec. 2.1 we have already provided the solution of Eq. (2.20) and Eq. (2.87) should have the same solution as Eq. (2.20). This means λ_n' is the eigenvalue of the system in the absence of the magnetic field. Now we write the solution in the complex form $\lambda_n=\Gamma+iC$, where the real part Γ stands for the decay rate and the imaginary part C represents the collective Lamb shift of the system of N two-level atoms [60, 67] without any magnetic field.

Next let's get the solution for λ_n which is the eigenvalue of the system in the presence of the magnetic field. Rewriting Eq. (2.86) in the form

$$\lambda_n+\frac{\phi^2}{4(\lambda_n-\gamma)}=\Gamma+iC\,, \quad (2.88)$$

then we obtain the solution of the eigenvalue equations (2.81) and (2.82)

$$\lambda_{n\pm}=\frac{\Gamma+\gamma+iC\mp i\sqrt{\phi^2+[C-i(\Gamma-\gamma)]^2}}{2}\,. \quad (2.89)$$

We find that the system has two eigenvalues ($\lambda_+,\ \lambda_-$). If the system is prepared initially in an excited eigenstate, we can obtain the spectrum of the radiation

photon from Eq. (2.65)

$$\frac{\partial \gamma_{\vec{k}}}{\partial t} = -ig_k \int d\vec{r}' \rho_1(\vec{r}')\beta_1(\vec{r}')e^{-\lambda_n + i(\nu_k + \frac{\phi}{2} - \omega_1)t - i\vec{k}\cdot\vec{r}'} - ig_k \int d\vec{r}' \rho_2(\vec{r}')\beta_2(\vec{r}')e^{-\lambda_n + i(\nu_k - \frac{\phi}{2} - \omega_2)t - i\vec{k}\cdot\vec{r}'} . \tag{2.90}$$

Next we focus on the problem of an uniformly excited sample and consider the initial condition as

$$\beta_1^j + \beta_2^j = \sqrt{\frac{1}{N}} e^{i\vec{k}_0\cdot\vec{r}_j} , \quad j = 1, 2....N , \tag{2.91}$$

which means

$$\beta_1(\vec{r}) + \beta_2(\vec{r}) = \sqrt{\frac{1}{N}} e^{i\vec{k}_0\cdot\vec{r}} . \tag{2.92}$$

As we know from Ref. [68], the right-hand side of Eq. (2.92) stands for an eigenstate of the system. Substituting Eq. (2.92) to Eq. (2.90) we obtain

$$\gamma_{\vec{k}} = \sqrt{N} g_k \frac{1 - e^{i(v_k - \omega_0)t - \lambda_n t}}{(v_k - \omega_0) + i\lambda_n} \frac{\int d\vec{r}' e^{i(\vec{k}_0 - \vec{k})\cdot\vec{r}'}}{V} . \tag{2.93}$$

In the following we pay attention to the case that $R \ll \lambda$. In the limit of $R \ll \lambda$, we make the approximation that

$$e^{i(\vec{k}_0 - \vec{k})\cdot\vec{r}'} \approx e^{i(\vec{k}_0 - \vec{k})\cdot\vec{r}_0} , \tag{2.94}$$

where $\vec{r}_0$ can be considered as the central position of the atoms. With this approximation we find

$$\gamma_{\vec{k}} = \sqrt{N} g_k e^{i(\vec{k}_0 - \vec{k})\cdot\vec{r}_0} \frac{1 - e^{i(v_k - \omega_0)t - \lambda_n t}}{(v_k - \omega_0) + i\lambda_n} . \tag{2.95}$$

Now we have deduced the spectrum of the emitted radiation when the system is initially in the eigenstate. Next we investigate the case that the system is initially in a mixed state. Let us define

$$|\psi_1\rangle = \frac{1}{\sqrt{N/2}} \sum_{j=1}^{N/2} e^{i\vec{k}_0\cdot\vec{r}_j} |g_1 g_2 ... e_j ... g_{N/2} ... g_N\rangle |0\rangle , \tag{2.96}$$

$$|\psi_2\rangle = \frac{1}{\sqrt{N/2}} \sum_{j=N/2+1}^{N} e^{i\vec{k}_0\cdot\vec{r}_j} |g_1 ... g_{N/2} g_{N/2+1} ... e_j ... g_N\rangle |0\rangle . \tag{2.97}$$

Initially the system is in a mixed state which has a 50% probability to be in state $|\psi_1\rangle$ and a 50% chance to be in state $|\psi_2\rangle$. We mark the two eigenstates of the system as $|E_+\rangle$ and $|E_-\rangle$, corresponding to the eigenvalues λ_+ and λ_-. We

introduce the notations

$$|E_+\rangle = \sum_{j=1}^{N/2} \beta_{1+}^j(t)|g_1 g_2 ... e_j ... g_{N/2} ... g_N\rangle|0\rangle + \sum_{j=N/2+1}^{N} \beta_{2+}^j(t)|g_1 ... g_{N/2} g_{N/2+1} ... e_j ... g_N\rangle|0\rangle \,, \tag{2.98}$$

$$|E_-\rangle = \sum_{j=1}^{N/2} \beta_{1-}^j(t)|g_1 g_2 ... e_j ... g_{N/2} ... g_N\rangle|0\rangle + \sum_{j=N/2+1}^{N} \beta_{2-}^j(t)|g_1 ... g_{N/2} g_{N/2+1} ... e_j ... g_N\rangle|0\rangle \,. \tag{2.99}$$

Next we transform the system into the representation of eigenstates. Assume that the system has a probability to be a in the eigenstate $|E_+\rangle$ initially. We know from Eqs. (2.85)-(2.87) that

$$\beta_{1+}(r) + \beta_{2+}(r) = \beta_{1-}(r) + \beta_{2-}(r) \,, \tag{2.100}$$

which yields

$$\beta_{1+}(r) + \beta_{2+}(r) = \sqrt{\frac{1}{N}} e^{i\vec{k}_0 \cdot \vec{r}} \,, \tag{2.101}$$

$$\beta_{1-}(r) + \beta_{2-}(r) = \sqrt{\frac{1}{N}} e^{i\vec{k}_0 \cdot \vec{r}} \,. \tag{2.102}$$

In the following we show how to derive the probability a. From the initial condition we have

$$\beta_1(r) = \beta_2(r) \,. \tag{2.103}$$

From Eq. (2.83) we find

$$[\beta_{1+}(r) - \beta_{2+}(r)] = \frac{i\phi}{2(\lambda_+ - \gamma)} [\beta_{1+}(r) + \beta_{2+}(r)] \,, \tag{2.104}$$

$$[\beta_{1-}(r) - \beta_{2-}(r)] = \frac{i\phi}{2(\lambda_- - \gamma)} [\beta_{1-}(r) + \beta_{2-}(r)] \,. \tag{2.105}$$

According to Eq. (2.103), we know that

$$a\beta_{1+}(r) + (1-a)\beta_{1-}(r) = a\beta_{2+}(r) + (1-a)\beta_{2+}(r) \,. \tag{2.106}$$

Then we derive

$$\left[a \frac{i\phi}{2(\lambda_+ - \gamma)} + (1-a) \frac{i\phi}{2(\lambda_- - \gamma)} \right] [\beta_{1+}(r) + \beta_{2+}(r)] = 0 \,, \tag{2.107}$$

and

$$a \frac{i\phi}{2(\lambda_+ - \gamma)} + (1-a) \frac{i\phi}{2(\lambda_- - \gamma)} = 0 \,. \tag{2.108}$$

Finally we obtain

$$a = \frac{\lambda_+ - \gamma}{\lambda_+ - \lambda_-}\,. \tag{2.109}$$

We turn now to the emitted radiation. Taking into account Eq. (2.95) we find in this case

$$\gamma_{\vec{k}} = \sqrt{N} g_k e^{i(\vec{k}_0 - \vec{k})\cdot\vec{r}_0} \left(\frac{\lambda_+ - \gamma}{\lambda_+ - \lambda_-} \frac{1 - e^{i(v_k - \omega_0)t - \lambda_+ t}}{(v_k - \omega_0) + i\lambda_+} - \frac{\lambda_- - \gamma}{\lambda_+ - \lambda_-} \frac{1 - e^{i(v_k - \omega_0)t - \lambda_- t}}{(v_k - \omega_0) + i\lambda_-} \right). \tag{2.110}$$

Upon introducing the field state [69]

$$|\gamma_0\rangle = \sum_{\vec{k}} \sqrt{N} g_k e^{i(\vec{k}_0 - \vec{k})\cdot\vec{r}_0} \left(\frac{A_+}{v_k - \omega_0 + i\lambda_+} + \frac{A_-}{v_k - \omega_0 + i\lambda_-} \right) |1_{\vec{k}}\rangle\,, \tag{2.111}$$

where $A_\pm = \pm(\lambda_\pm - \gamma)/(\lambda_+ - \lambda_-)$, we have $|\psi(t)\rangle \to |g_1 g_2 ... g_N\rangle|\gamma_0\rangle$ for times long compared to the superradiance decay $t \gg \Gamma^{-1}$. Here the index '0' in $|\gamma_0\rangle$ reminds that this state corresponds to the situation when all atoms can be considered located at position r_0 in the limit of $R \ll \lambda$. This is a linear superposition of the single-photon states with different wave vectors associated with them. Next we will discuss some more details about the field state $|\gamma_0\rangle$.

2.2.2 Discussion in the limit $k_0 R \ll 1$

We may define the amplitude of the radiation emitted by the photon in mode $\vec{k}$ as follows

$$\sigma_k = \frac{A_+}{\delta - i\lambda_+} + \frac{A_-}{\delta - i\lambda_-}\,, \tag{2.112}$$

where $\delta = \omega_0 - v_k$, assuming that the coupling constant $\sqrt{N} g_k e^{i(\vec{k}_0 - \vec{k})\cdot\vec{r}_0}$ does not change. This is very reasonable to suppose because the frequency of the radiated photon is around the resonant energy. Then the field state $|\gamma_0\rangle$ can be written as

$$|\gamma_0\rangle = -g \sum_{\vec{k}} \sigma_k |1_{\vec{k}}\rangle\,. \tag{2.113}$$

Actually the amplitude defined in Eq. (2.112) can be considered as the atomic response of the system. σ_k is a function of the complex variable δ which has two poles

$$\delta_\pm = i\lambda_\pm = \frac{1}{2}\left(-C + i(\Gamma + \gamma) \pm \sqrt{\phi^2 + [C - i(\Gamma - \gamma)]^2} \right). \tag{2.114}$$

These poles produce the resonant contributions to the amplitude and hence can be attributed to the effective states with frequencies and dephasing rates by the real and imaginary parts of $\delta_\pm$, respectively. The amplitude is presented as a superposition of two resonant responses associated with the transitions from the ground state to the corresponding eigenstates. ϕ is the energy difference between the two resonant transitions of the single atom caused by Zeeman effect. However,

with N atoms the situation changes due to the collective effects. For instance, the resonant energy difference equals $\sqrt{\phi^2 + C^2}$ when $\Gamma - \gamma = 0$ according to Eq. (2.114). In the following we demonstrate an eigenstate-based analysis for different parameter regimes.

2.2.2.1 Collective Lamb shift equals zero

In the case that collective Lamb shift equals zero, $C = 0$, both the amplitudes and positions of the eigenstates depend on a single respective parameter. Namely, the amplitudes are defined by $x = (\Gamma - \gamma)/\phi$ (we assume $\phi > 0$), and the positions are defined by $y = \sqrt{\phi^2 + 4\Gamma\gamma}/(\Gamma + \gamma)$. In terms of these parameters, the following expression can be written:

$$A_{\pm} = 0.5 \pm i \frac{x}{2\sqrt{1 - x^2}}\,, \tag{2.115}$$

and

$$\delta_{\pm} = 0.5(\Gamma + \gamma)\left(i \pm \sqrt{y^2 - 1}\right)\,. \tag{2.116}$$

Significant superradiance

According to Eq. (2.114), the real parts of the poles describe the positions of the eigenstates. In the case of significant superradiance which means $\Gamma \gg \gamma$ and $0 < y < 1$, the real parts $\mathrm{Re}(\delta_{\pm}) = 0$. Hence, both resonances are centered at the resonant transition energy ω_0 in the absence of the magnetic field. This means in this case the transition line is no longer split by ϕ as the traditional Zeeman effect. In turn, the imaginary parts of the poles describe the widths of the eigenstates.

In the limit $x \gg 1$, the poles according to Eqs. (2.116) can be approximately written as

$$\delta_{+} = i\left(\Gamma - \frac{\phi^2}{4(\Gamma - \gamma)}\right)\,, \tag{2.117}$$

and

$$\delta_{-} = i\left(\gamma + \frac{\phi^2}{4(\Gamma - \gamma)}\right)\,. \tag{2.118}$$

We find that one of the eigenstate is broad and the other is narrow. In the finite range $\Gamma\gamma \leq \phi^2/4 < (\Gamma - \gamma)^2$, the radiation spectrum which is the sum of broad and the narrow poles results in the characteristic feature of EIT (see Fig. 2.1). This spectrum is no longer the sum of the two Lorentzians split by ϕ with the effective width $(\Gamma + \gamma)/2$. In fact the transparency feature originates from the difference of two Lorentzians centered at the same position, rather than the summation of two Lorentzians shifted by ϕ, which clearly reflects the importance of interference.

Significant energy difference ϕ

In the limit $x \ll 1$, the poles can be approximately written as

$$\delta_{\pm} = \pm\left(\frac{\phi}{2} - \frac{(\Gamma - \gamma)^2}{4\phi}\right) + i\frac{(\Gamma + \gamma)}{2}\,, \tag{2.119}$$

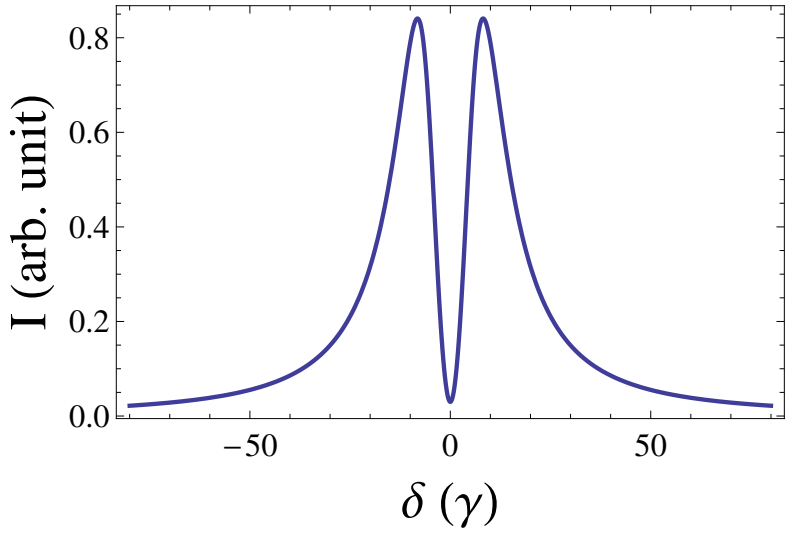

Figure 2.1: The radiation spectrum in the regime of EIT. The numerical values for the parameters used were the following: $\Gamma = 12\,\gamma\,, \phi = 15\,\gamma$.

and

$$A_{\pm} = \frac{1}{2} \pm \frac{\Gamma - \gamma}{2\phi}\,. \tag{2.120}$$

As a result, in this case the spectrum can be approximately considered as the summation of two Lorentzians split by ϕ with the width $(\Gamma + \gamma)/2$. It is similar to the traditional Zeeman effect for a single atom (see Fig. 2.2).

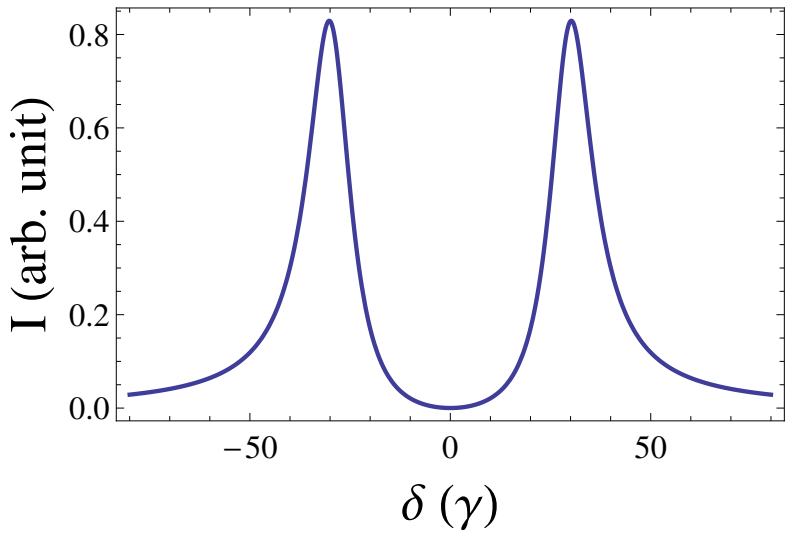

Figure 2.2: The radiation spectrum in the case of $\phi \gg (\Gamma - \gamma)$. The used numerical parameters were the following: $\Gamma = 12\,\gamma\,, \phi = 60\,\gamma$.

Bifurcation point

A bifurcation point is a special case for which $x = 1$, where the spectrum has a pole of the second order:

$$\sigma_k = \frac{\delta - i\gamma}{\left(\delta - i\frac{(\Gamma+\gamma)}{2}\right)^2} \,. \tag{2.121}$$

In this degenerate case, the presentation of the spectrum as a superposition of two Lorentzians is no longer valid. Fig. 2.3 shows the spectrum at the bifurcation point where EIT occurs.

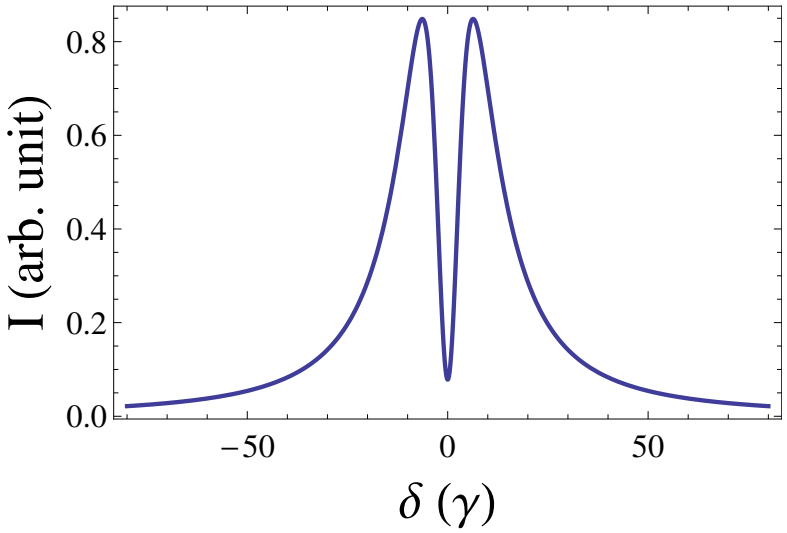

Figure 2.3: The radiation spectrum at the bifurcation point. The following numerical parameters were used: $\Gamma = 12\,\gamma\,, \phi = 11\,\gamma$.

2.2.2.2 Significant Collective Lamb shift

In the case that $C \gg (\Gamma - \gamma)$ and $\phi \gg (\Gamma - \gamma)$, we can derive that

$$\delta_+ = \frac{1}{2}\left[-C + i\left(\Gamma + \gamma - \frac{C(\Gamma-\gamma)}{\sqrt{\phi^2 + C^2}}\right) + \sqrt{\phi^2 + C^2}\right] , \tag{2.122}$$

and

$$\delta_- = \frac{1}{2}\left[-C + i\left(\Gamma + \gamma + \frac{C(\Gamma-\gamma)}{\sqrt{\phi^2 + C^2}}\right) - \sqrt{\phi^2 + C^2}\right] . \tag{2.123}$$

Now the spectrum can be treated as the summation of two Lorentzians which do not overlap. The Lorentzians are split by $\sqrt{\phi^2 + C^2}$, not ϕ any more, see Fig. 2.4. The gap between the peaks of the radiation spectrum demonstrated in Fig. 2.4 is about 33.5γ which is equal to $\sqrt{C^2 + \phi^2}$ not ϕ. In the limit of $C \gg \phi$, the gap is even close to the collective Lamb shift C. The ratio of these two peaks also changes. It is not close to 1 as the traditional Zeeman effect for a single atom.

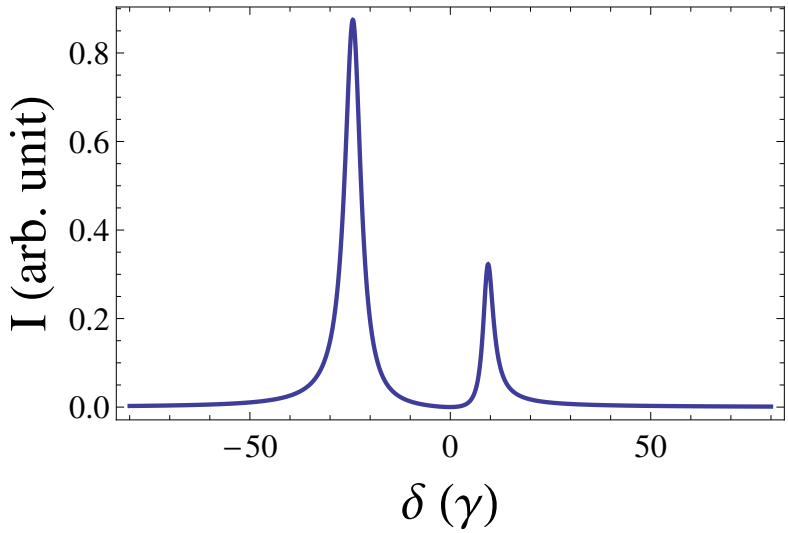

Figure 2.4: The radiation spectrum when $C \gg (\Gamma - 2\gamma)$ and $\phi \gg (\Gamma - 2\gamma)$. The following numerical parameters were used: $C = 15\,\gamma\,, \Gamma = 3\,\gamma\,, \phi = 30\,\gamma$.

Chapter 3

Field control of single x-ray photon superradiance in nuclear forward scattering

In the previous Chapter, we have investigated the problem of a single-photon cooperative emission from a cloud of N atoms. The cooperative radiation spectrum of the single photon has been obtained based on the timed Dicke state. Now we want to observe this cooperative emission in some specific systems, for instance, SR light scattered by a nuclear ensemble in the forward direction. Mössbauer nuclei are used as nuclear targets, for instance, ^{57}Fe. Due to the recoilless nature of the Mössbauer nuclear transition in solid-state nuclear targets, a delocalized, collective excitation (in literature referred to as nuclear exciton [70]) will be created by the single resonant photon. Since there is at most one resonant x-ray photon in s SR pulse, we can consider the case as a single x-ray photon emission from a large number of nuclei. However, the thickness of the nuclear ensemble is usually on the scale of micrometers and the wavelength of the resonant x-ray photon is less than 1 Ångstrom. The thickness of the nuclear ensemble is much larger than the wavelength of the x-ray photon, so the excitation probabilities for all nuclei within the ensemble are no longer the same. Although there is only one resonant photon entering the ensemble, the timed Dicke state

$$|\psi_0\rangle = \frac{1}{\sqrt{N}} \sum_{j=1}^{N} e^{ik_0 \cdot \vec{r}_j} |g_1 g_2 ... e_j ... g_N\rangle |0\rangle \,. \tag{3.1}$$

can not be generated. The model introduced in the previous Chapter is not applicable in this case.

In this Chapter we study the collective emission of single x-ray photon in NFS. We are interested in the parameter regime $R \gg \lambda$ complementary to the one discussed in the previous Chapter 2. In order to derive the time response in NFS, we adapt the Maxwell-Bloch equations (MBE) known from quantum optics to describe the resonant light pulse propagation through a nuclear medium. Means to coherently control single x-ray photons in resonant scattering of light off nuclei by electric or magnetic fields are investigated theoretically. Two types of time-dependent perturbations of NFS are considered for coherent control of the resonantly scattered x-ray quanta. First, the simultaneous coherent propagation of two pulses through the nuclear sample is addressed. We find that the signal of

a weak pulse can be enhanced or suppressed by a stronger pulse simultaneously propagating through the sample in counter-propagating geometry. Second, the effect of a time-dependent hyperfine splitting is investigated and we put forward a scheme that allows parts of the spectrum to be shifted forward in time. This is the inverse effect of coherent photon storage and may become a valuable technique if single x-ray photon wavepackets are to become the information carriers in future photonic circuits.

3.1 Introduction

Recent experimental developments of coherent light sources have opened the x-ray parameter regime for fascinating coherent control concepts originally developed in quantum optics. Thus, new fields such as x-ray quantum optics [12] and nuclear quantum optics [71] emerge. The interest in nuclear systems is sustained by the recent commissioning of XFEL facilities [13–17] and the development of x-ray optics devices [72–78] which bring into play higher photon frequencies. Nuclei with low-lying collective states therefore become candidates for nuclear quantum optics [28, 71, 79–81] or nuclear coherent population transfer [82, 83].

Coherent control tools based on nuclear cooperative effects [11, 18–20, 84] are known also from NFS experiments with third-generation light sources. The underlying physics here relies on the delocalized nature of the nuclear excitation produced by SR light, i.e., the formation of so-called nuclear excitons. NFS setups offer a framework for control of single x-ray photons, which might become a useful tool for optics and quantum information applications at shorter wavelengths on the way towards more compact photonic devices [24]. Phase-sensitive storage and π phase modulation for single hard x-ray photons in a NFS setup have been recently proposed [25], as well as the generation of a nuclear polariton with two entangled counter-propagating branches [26] comprising a single x-ray photon.

3.2 Theoretical approach: Maxwell-Bloch Equations

In a typical NFS experiment, monochromatized light pulses shine perpendicular to a sample containing Mössbauer nuclei, usually ^{57}Fe. The delayed nuclear response is then recorded by observing the resonantly scattered light in the forward direction, as illustrated schematically in Fig. 3.1(a). The interval between successive light pulses is chosen long enough to facilitate the nuclear response detection, typically larger than $1/\Gamma$, where Γ denotes the nuclear spontaneous decay rate. The driven magnetic dipole (M1) nuclear transition connects the ^{57}Fe ground state characterized by spin $I_g = 1/2$ to the first excited state at 14.413 keV with $I_e = 3/2$. The hyperfine-split level scheme of ^{57}Fe for the states of interest is depicted in Fig. 3.1(b). The resonant scattering occurs via an excitonic state, i.e., an excitation coherently spread out over a large number of nuclei. In case of coherent scattering, the nuclei return to their initial state, such that the scattering path and the number of occurred events are unknown. This leads to the cooperative emission, with scattering only in forward direction (except for the case of Bragg

scattering [85–88]) and decay rates modified by the formation of sub- and superradiant states as key signatures. The observed decay signal is therefore far from being exponential, as can be seen in the example presented in Fig. 3.1(c).

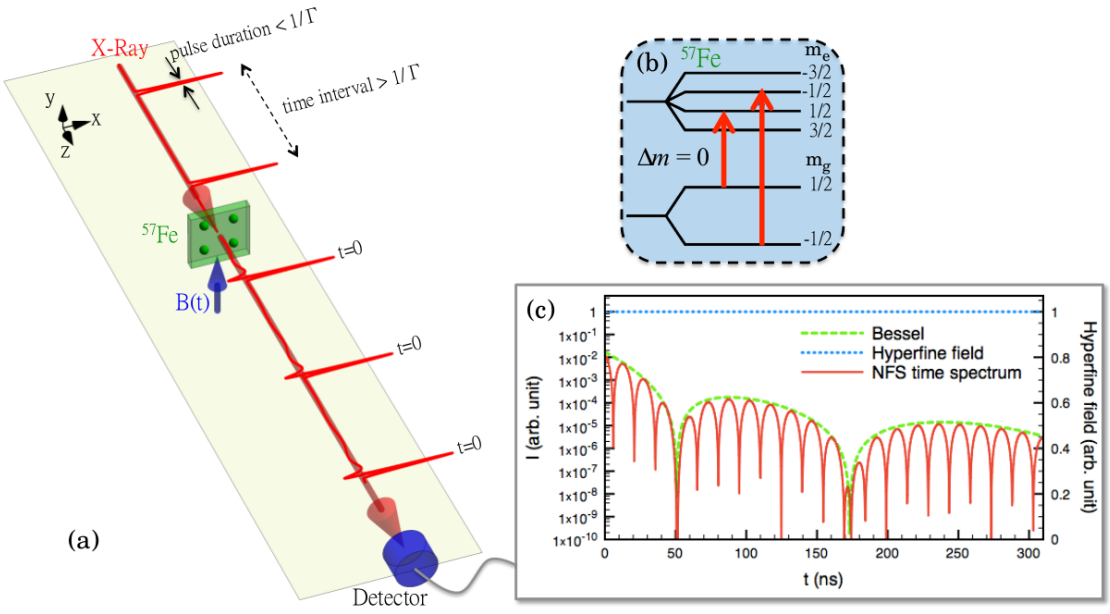

Figure 3.1: (a) Typical NFS setup. The resonant x-ray pulse shines perpendicularly to the nuclear sample depicted by the green rectangle. After each pulse, the delayed nuclear response in the forward direction is recorded by the detector. The blue thick vertical arrow shows the applied magnetic field $\mathbf{B}(t)$. (b) ^{57}Fe ground and first excited state nuclear hyperfine levels. In this example, the $\Delta m = 0$ transitions are driven by linearly polarized x-rays. (c) Intensity of the coherently scattered light in the forward direction (red solid line) for an incident field driving the $\Delta m = 0$ transitions. The envelope given by the Bessel function for the degenerate states case is shown by the green long-dashed line. The hyperfine magnetic field depicted by the blue short-dashed line is kept constant during the scattering for this example [89].

In the previous Chapter we derive the radiation spectrum in the limit case in which the size of the sample is much smaller than the wavelength of the photon. Here, although the exciton picture [19, 86, 90] justifies the coherently scattered radiation proceeding in the forward direction, it does not provide a straightforward manner to correctly derive the scattering spectrum. The model in Sec. 2.1 invalidates and the scattering spectrum can be rather achieved by means of the wave equation for the time-dependent field propagation which reveals the field intensity at the exit from the sample. The ansatz of forward emission of the resonantly scattered light is however related to the exciton picture and enters the MBE phenomenologically.

In quantum optics, the light-nuclei interaction is typically described by monitoring the quantum time evolution of the density operator $\hat{\rho}$, given by the master equation [69]

$$\partial_t \hat{\rho} = \frac{1}{i\hbar}[\hat{H}, \hat{\rho}] + \hat{\rho}_s \,. \tag{3.2}$$

Here, $\hat{H}$ is the interaction Hamiltonian between the matter and the incident electromagnetic field and $\hat{\rho}_s$ describes decoherence processes such as spontaneous decay. For a two-level system corresponding to a single nuclear resonance with ground state $|g\rangle$ and excited state $|e\rangle$, the interaction Hamiltonian is given by

$$\hat{H} = -\frac{\hbar}{2}\begin{pmatrix} 0 & \Omega_p^* \\ \Omega_p & 2\Delta_p \end{pmatrix}, \tag{3.3}$$

where $\hbar$ is the reduced Planck constant, and Δ_p is the detuning (i.e., mismatch) between the field and nuclear transition frequencies. Furthermore, Ω_p denotes the Rabi frequency defined as

$$\Omega_p = \frac{1}{\hbar}\langle e|\hat{H}|g\rangle\,. \tag{3.4}$$

By using the Coulomb gauge for the vector potential $\vec{A}(z,t)$ and the rotating wave approximation, we can obtain a useful expression of the reduced interaction matrix element,

$$\begin{aligned}\langle e|\hat{H}|g\rangle &= -\langle e|\hat{\vec{j}}(\vec{k})\cdot\hat{\vec{A}}(z,t)|g\rangle \\ &= E(z,t)\sqrt{2\pi}\sqrt{\frac{L+1}{L}}\frac{k^{L-1}}{(2L+1)!!}\sqrt{B(\varepsilon/\mu L,|g\rangle\rightarrow|e\rangle)} \\ &\equiv E(z,t)\alpha(\varepsilon/\mu L,|g\rangle\rightarrow|e\rangle)\,,\end{aligned} \tag{3.5}$$

where $\hat{\vec{j}}(\vec{k})$ is the current density operator in momentum representation, $E(z,t)$ is the electric field envelope, L is the angular momentum of the transition, ε/μ the transition type (electric/magnetic), and $B(\varepsilon/\mu L,|g\rangle\rightarrow|e\rangle)$ the nuclear reduced transition probability [91]. For the equation above we have considered the case of a single nuclear transition from a degenerate ground state. Typically, in atomic quantum optics only electric dipole transitions are of interest and $\alpha(\varepsilon 1,|g\rangle\rightarrow|e\rangle)$ stands then for the electric dipole moment. In our case, we have written in Eq. (3.5) the general expression of the Rabi frequency involving the electromagnetic multipole moment $\alpha(\varepsilon/\mu L,|g\rangle\rightarrow|e\rangle)$.

With the notation $\rho_{mn} = \langle m|\hat{\rho}|n\rangle$ with $\{m,n\}\in\{e,g\}$ we obtain the Bloch equations

$$\begin{aligned}\partial_t\rho_{gg} &= \Gamma\rho_{ee} - \frac{i}{2}(\Omega_p\rho_{ge} - \Omega_p^*\rho_{eg})\,, \\ \partial_t\rho_{eg} &= -\left(i\Delta_p + \frac{\Gamma}{2}\right)\rho_{eg} - \frac{i}{2}\Omega_p(\rho_{ee}-\rho_{gg})\,, \\ \partial_t\rho_{ee} &= -\Gamma\rho_{ee} + \frac{i}{2}(\Omega_p\rho_{ge} - \Omega_p^*\rho_{eg})\,,\end{aligned} \tag{3.6}$$

where the spontaneous decay rate Γ comprises the radiative and the internal conversion channel.

By coupling the equations above for the density matrix to the Maxwell wave equation, we can describe the dynamics of both matter and radiation field, i.e., the propagation of a light pulse through the resonant medium taking into account also the sample response. In the following we consider an electromagnetic wave with the polarization vector $\vec{e}_x$, frequency ω and wave number $k_0 = \omega/c$ with a slowly varying envelope

$$\vec{E}(z,t) = E(z,t)e^{-i(\omega t - k_0 z)}\vec{e}_x\,. \tag{3.7}$$

Considering only unidirectional propagation in the forward direction according to our ansatz, the wave equation

$$\left(\frac{\partial^2}{\partial z^2} - \frac{1}{c^2}\frac{\partial^2}{\partial t^2}\right)\vec{E}(z,t) = \frac{4\pi}{c^2}\frac{\partial}{\partial t}\vec{I}(z,t) \tag{3.8}$$

for the electric field intensity has as source term the macroscopic current density $\vec{I}(z,t)$ induced by the radiation in the system of resonant nuclei. The induced current density can be written as

$$\vec{I}(z,t) = I(z,t)e^{-i(\omega t - k_0 z)}\vec{e}_x\,. \tag{3.9}$$

We consider the parameter regime for which $|\frac{\partial E(z,t)}{\partial t}|,\ |c\frac{\partial E(z,t)}{\partial z}| \ll |\omega E(z,t)|$ holds. In the slowly varying envelope approximation, the wave equation reduces to

$$\frac{\partial E(z,t)}{\partial z} + \frac{1}{c}\frac{\partial E(z,t)}{\partial t} = -\frac{2\pi}{c}I(z,t)\,. \tag{3.10}$$

The crucial step here is to express the current density with the help of the density matrix in order to couple the Bloch and Maxwell equations. For a two-level system interacting with the field in atomic quantum optics, the current can be expressed with the help of the coherence ρ_{eg} and the dipole moment $\alpha(\varepsilon 1, |g\rangle \to |e\rangle)$. Following the argument presented in Ref. [92], the current density for a single nuclear resonance is obtained by summing over all nuclei participating in the coherent scattering and tracing over $\hat{\vec{j}}(\vec{k})e^{ik_0 z}\hat{\rho}$. Taking into account the alternative form of the Hamiltonian with the vector potential written in the Coulomb gauge, $\hat{H} = i\hat{\vec{j}}(\vec{k})\cdot\vec{e}_x e^{ik_0 z}E(z,t)/\omega$, we can relate to the matrix element in Eq. (3.5) and express the current in the simplified form

$$\begin{aligned} I(z,t) &= N\langle e|\hat{\vec{j}}(\vec{k})e^{ik_0 z}|g\rangle\rho_{eg} \\ &= \frac{\omega}{i}N\alpha(\varepsilon/\mu L, |g\rangle \to |e\rangle)\rho_{eg}\,, \end{aligned} \tag{3.11}$$

where N is the particle number density and we take into account all nuclei over which the excitation is coherently shared. Combining Eqs. (3.5), (3.10) and (3.11) we obtain the following wave equation involving the Rabi frequency,

$$\frac{1}{c}\partial_t\Omega_p(z,t) + \partial_z\Omega_p(z,t) = i\frac{2\pi\omega N[\alpha(\varepsilon/\mu L, |g\rangle \to |e\rangle)]^2}{\hbar c}\rho_{eg}\,. \tag{3.12}$$

Together with the three Bloch equations (3.6), we now have arrived at the MBE for the Rabi frequency. The scattered field is then proportional to Ω_p and the scattered intensity $I \propto |\Omega_p|^2$. We proceed now with some changes of notation in order to facilitate the comparison with established NFS results. The expression of the radiative nuclear decay rate Γ_γ is also connected to the reduced transition probabilities $B(\varepsilon/\mu L, |e\rangle \to |g\rangle)$ via

$$\Gamma_\gamma = \frac{8\pi(L+1)}{L[(2L+1)!!]^2}\left(\frac{E_0}{\hbar c}\right)^{2L+1} B(\varepsilon/\mu L, |e\rangle \to |g\rangle)\,, \tag{3.13}$$

where E_0 denotes the transition energy and

$$B(\varepsilon/\mu L, |e\rangle \to |g\rangle) = \frac{2I_g+1}{2I_e+1} B(\varepsilon/\mu L, |g\rangle \to |e\rangle)\,. \tag{3.14}$$

The resonant cross section can also be expressed as

$$\sigma = \frac{2\pi}{k_0^2}\frac{2I_e+1}{2I_g+1}\frac{\Gamma_\gamma}{\Gamma} = [\alpha(\varepsilon/\mu L, |g\rangle \to |e\rangle)]^2 \frac{8\pi k}{\hbar\Gamma}\,, \tag{3.15}$$

where Γ is the spontaneous decay rate. Introducing the dimensionless effective thickness $\xi = N\sigma L/4$ [92] with L the length of the sample, we can rewrite the wave equation (3.12) in the MBE as

$$\frac{1}{c}\partial_t \Omega_p(z,t) + \partial_z \Omega_p(z,t) = i\eta\rho_{eg}(z,t)\,, \tag{3.16}$$

with $\eta = \frac{\xi\Gamma}{L}$.

As initial conditions for the MBE we now consider

$$\begin{aligned} \rho_{mn}(z,0) &= \delta_{mg}\delta_{ng}\,, \\ \Omega_p(z,0) &= 0\,, \\ \Omega_p(0,t) &= \Omega_{0p}\delta(t-\tau)\,, \end{aligned} \tag{3.17}$$

where τ marks the arrival of the incident resonant light pulse. In the following we set the detuning Δ_p to zero. Taking the incident pulse as a small perturbation such that $\Omega_p \ll \Gamma$ and no Rabi oscillations may occur, we obtain in first order perturbation theory from Eqs. (3.6) and (3.16) only two coupled equations for Ω_p,

$$\begin{aligned} \partial_t \rho_{eg} &= -\frac{\Gamma}{2}\rho_{eg} + \frac{i}{2}\Omega_p\,, \\ \frac{1}{c}\partial_t \Omega_p + \partial_z \Omega_p &= i\eta\rho_{eg}\,. \end{aligned} \tag{3.18}$$

Performing a change of variable and using the Fourier transform, the dispersion

relation of the system can be obtained [93],

$$k(\omega) = \frac{\omega}{c} - \frac{\eta}{2\omega} - i\frac{\Gamma}{2c}\,. \tag{3.19}$$

The solution for the Rabi frequency can be found by inverse Fourier transform

$$\begin{aligned}\Omega_p(z,t) &= \frac{1}{2\pi}e^{-\frac{\Gamma}{2}[\frac{z}{c}+(t-\tau)]}\int_{-\infty}^{\infty} e^{-i[(\frac{\omega}{c}-\frac{\eta}{2\omega})z-\omega(t-\tau)]}d\omega \\ &= \left\{\delta\left[\frac{z}{c}-(t-\tau)\right] - \frac{\xi\Gamma z}{L}\frac{J_1\left[2\sqrt{(\frac{\xi\Gamma z}{L})(t-\tau-\frac{z}{c})}\right]}{2\sqrt{(\frac{\xi\Gamma z}{L})(t-\tau-\frac{z}{c})}}\right\} e^{-\frac{\Gamma}{2}(\frac{z}{c}+t-\tau)}\,,\end{aligned} \tag{3.20}$$

where $J_1(z)$ is the Bessel function of the first kind. The terms z/c are typically negligible because L/c is much smaller than $(t-\tau)$. With this, the result above reproduces the expression of the dynamical beat [85, 86, 92, 94] known from the time-dependent theory of NFS for a single nuclear resonance. An illustration of the dynamical beat for a test case is given by the green dashed line in Fig. 3.1(c).

The MBE become more complicated for the case of the resonant driving of several nuclear resonances in a hyperfine-split, multi-level system. The typical example is ^{57}Fe in a hyperfine magnetic field which has two ground ($I_g = 1/2$) and four excited ($I_e = 3/2$) magnetic sublevels. The hyperfine levels are coupled by six transitions, depending on the magnetic field geometry and polarization of the incident SR or XFEL field. Let us first consider the x-ray pulse is linearly polarized and the direction of polarization is parallel to the x axis. The magnetic field $\mathbf{B}$(t) that sets the quantization axis for the nuclear ground and excited state spin projections m_g and m_e is parallel to the z axis. In this scenario, the two $\Delta m = m_e - m_g = 0$ magnetic dipole transitions will be driven by the incident pulse. The MBE include then a number of Clebsch-Gordan coefficients that quantify the individual couplings between the four states,

$$\partial_t\rho_{11} = \Gamma(C_{14}^2\rho_{44} + C_{15}^2\rho_{55}) - \frac{i}{2}C_{15}(\Omega_p\rho_{15} - \Omega_p^*\rho_{51})\,,$$

$$\partial_t\rho_{22} = \Gamma(C_{24}^2\rho_{44} + C_{25}^2\rho_{55}) - \frac{i}{2}C_{24}(\Omega_p\rho_{24} - \Omega_p^*\rho_{42})\,,$$

$$\partial_t\rho_{42} = -\frac{1}{2}(2i\Delta_{p,4\to2} + C_{14}^2\Gamma + C_{24}^2\Gamma)\rho_{42} - \frac{i}{2}C_{24}\Omega_p(\rho_{44} - \rho_{22})\,,$$

$$\partial_t\rho_{44} = -\Gamma(C_{14}^2 + C_{24}^2)\rho_{44} + \frac{i}{2}C_{24}(\Omega_p\rho_{24} - \Omega_p^*\rho_{42})\,,$$

$$\partial_t\rho_{51} = -\frac{1}{2}(2i\Delta_{p,5\to1} + C_{15}^2\Gamma + C_{25}^2\Gamma)\rho_{51} - \frac{i}{2}C_{15}\Omega_p(\rho_{55} - \rho_{11})\,,$$

$$\partial_t \rho_{55} = -\Gamma(C_{15}^2 + C_{25}^2)\rho_{55} + \frac{i}{2} C_{15}(\Omega_p \rho_{15} - \Omega_p^* \rho_{51}) \,,$$

$$\frac{1}{c}\partial_t \Omega_p + \partial_z \Omega_p = i\eta'(a_{51}\rho_{51} + a_{42}\rho_{42}) \,. \tag{3.21}$$

In the above equations, the states $|1\rangle$ and $|2\rangle$ denote the two ground states with $m_g = 1/2$ and $m_g = -1/2$, respectively, and $|3\rangle$, $|4\rangle$, $|5\rangle$ and $|6\rangle$ the four excited states with $m_e = -3/2$, $m_e = -1/2$, $m_e = 1/2$ and $m_e = 3/2$, respectively. The shortened notation used for the Clebsch-Gordan coefficients [95] is $C_{ij} = C(I_g\, I_e\, 1; m_g\, m_e\, M)$ where $i \in \{1, 2\}$ sets the value of m_g and $j \in \{3, 4, 5, 6\}$ the one of m_e. Furthermore, $\Delta_{p,4\to2} = \omega_{42} - \omega$ and $\Delta_{p,5\to1} = \omega_{51} - \omega$, where ω_{51} and ω_{42} are the resonant frequencies of the $|1\rangle \to |5\rangle$ and $|2\rangle \to |4\rangle$ transitions, respectively. The coefficients η', a_{51} and a_{42} can be deduced by studying the limiting case when the magnetic field $\mathbf{B}(\mathrm{t})$ goes to zero and Eqs. (3.21) should resume the form of (3.6) and (3.16). The last equation in (3.21) then becomes

$$\frac{1}{c}\partial_t \Omega_p + \partial_z \Omega_p = i\eta \left(\frac{\rho_{51}}{C_{15}} + \frac{\rho_{42}}{C_{24}} \right) . \tag{3.22}$$

The MBE is therefore a very convenient method to treat NFS involving multiple resonances since the system of equations can be solved numerically. For completion, the corresponding equations for the case of a circularly polarized pulse driving the four $\Delta m = m_e - m_g = \pm 1$ transitions between the six ground and excited hyperfine levels are given in the following. The fields that drive the transitions $\Delta m = m_e - m_g = 1$ and $\Delta m = m_e - m_g = -1$ are denoted as Ω_p^+ and Ω_p^-, respectively. Using the level notations defined before, we obtain the Bloch equations

$$\partial_t \rho_{11} = \Gamma(C_{14}^2 \rho_{44} + C_{15}^2 \rho_{55} + C_{16}^2 \rho_{66}) - \frac{i}{2}[C_{14}(\Omega_p^- \rho_{14} - \text{c.c.}) + C_{16}(\Omega_p^+ \rho_{16} - \text{c.c.})] \,,$$

$$\partial_t \rho_{22} = \Gamma(C_{23}^2 \rho_{33} + C_{24}^2 \rho_{44} + C_{25}^2 \rho_{55}) - \frac{i}{2}[C_{23}(\Omega_p^- \rho_{23} - \text{c.c.}) + C_{25}(\Omega_p^+ \rho_{25} - \text{c.c.})] \,,$$

$$\partial_t \rho_{32} = -\frac{1}{2}(2i\Delta_{p,3\to2} + C_{23}^2\Gamma)\rho_{32} - \frac{i}{2} C_{23}\Omega_p^-(\rho_{33} - \rho_{22}) - \frac{i}{2} C_{25}\Omega_p^+ \rho_{35} \,,$$

$$\partial_t \rho_{33} = -C_{23}^2 \Gamma \rho_{33} + \frac{i}{2} C_{23}(\Omega_p^- \rho_{23} - \text{c.c.}) \,,$$

$$\partial_t \rho_{41} = -\frac{1}{2}(2i\Delta_{p,4\to1} + C_{14}^2\Gamma + C_{24}^2\Gamma)\rho_{41} - \frac{i}{2} C_{14}\Omega_p^-(\rho_{44} - \rho_{11}) - \frac{i}{2} C_{16}\Omega_p^+ \rho_{46} \,,$$

$$\partial_t \rho_{44} = -(C_{14}^2 + C_{24}^2)\Gamma \rho_{44} + \frac{i}{2} C_{14}(\Omega_p^- \rho_{14} - \text{c.c.}) \,,$$

$$\partial_t \rho_{52} = -\frac{1}{2}(2i\Delta_{p,5\to2} + C_{15}^2\Gamma + C_{25}^2\Gamma)\rho_{52} - \frac{i}{2} C_{25}\Omega_p^+(\rho_{55} - \rho_{22}) - \frac{i}{2} C_{23}\Omega_p^- \rho_{53} \,,$$

$$\partial_t\rho_{53} = -\frac{1}{2}(2i\Delta_{p,5\to2} - 2i\Delta_{p,3\to2} + C_{15}^2\Gamma + C_{25}^2\Gamma + C_{23}^2\Gamma)\rho_{52} - \frac{i}{2}C_{23}\Omega_p^-\rho_{52} + \frac{i}{2}C_{25}\Omega_p^+\rho_{23}\,,$$

$$\partial_t\rho_{55} = -(C_{15}^2 + C_{25}^2)\Gamma\rho_{55} + \frac{i}{2}C_{25}(\Omega_p^+\rho_{25} - \text{c.c.})\,,$$

$$\partial_t\rho_{61} = -\frac{1}{2}(2i\Delta_{p,6\to1} + C_{16}^2\Gamma)\rho_{32} - \frac{i}{2}C_{16}\Omega_p^+(\rho_{66} - \rho_{11}) - \frac{i}{2}C_{14}\Omega_p^-\rho_{64}\,,$$

$$\partial_t\rho_{64} = -\frac{1}{2}(2i\Delta_{p,6\to1} - 2i\Delta_{p,4\to1} + C_{14}^2\Gamma + C_{16}^2\Gamma + C_{24}^2\Gamma)\rho_{64} - \frac{i}{2}C_{14}\Omega_p^-\rho_{61} + \frac{i}{2}C_{16}\Omega_p^+\rho_{14}\,,$$

$$\partial_t\rho_{66} = -C_{16}^2\Gamma\rho_{66} + \frac{i}{2}C_{16}(\Omega_p^+\rho_{16} - \text{c.c.})\,, \tag{3.23}$$

with the Maxwell equations for the Rabi frequencies Ω_p^+ and Ω_p^- of the two components given by

$$\begin{aligned}\frac{1}{c}\partial_t\Omega_p^+ + \partial_z\Omega_p^+ &= i\frac{\eta}{2}\left(\frac{\rho_{61}}{C_{16}} + \frac{\rho_{52}}{C_{25}}\right)\,,\\ \frac{1}{c}\partial_t\Omega_p^- + \partial_z\Omega_p^- &= i\frac{\eta}{2}\left(\frac{\rho_{41}}{C_{41}} + \frac{\rho_{32}}{C_{23}}\right)\,.\end{aligned} \tag{3.24}$$

Comparison of theoretical and experimental NFS results for SR show very good agreement. The produced excitation is very weak, such that typically either no photon or one photon is resonantly scattered per pulse and the spectra describe the propagation of a single-photon wavepacket. However, most theoretical approaches, including the MBE discussed here, rely on the classical Maxwell equation to describe the scattered field. The legitimate question may arise how come does the classical field correctly describe the behavior of single photons? This would be the case if the photon state under investigation were a coherent state, $C_0|0\rangle + C_1|1\rangle + C_2|2\rangle + \ldots$ where $|n\rangle$ is the n-photon Fock state and $|C_0|^2 \gg |C_1|^2 \gg |C_2|^2 \gg \ldots$. After the incident pulse passes through a nuclear target, mostly no nuclear response is detected, and only few single-photon events are registered, such that the coherent state condition is fulfilled.

3.3 Two resonantly propagating pulses

Let us consider the case of two resonant x-ray pulses interacting simultaneously with a nuclear target containing ^{57}Fe Mössbauer nuclei. We choose the counter-propagating geometry as shown schematically in Fig. 3.2(a) such that the two signals can be easily separated experimentally. The recent development of normal-incidence x-ray mirrors [75, 76] is an important step allowing such more complex setup geometries. For simplicity we assume a single nuclear transition with the two light pulses which reach the target from opposite directions at $z = 0$ and $z = L$. We consider the case of two pulses both with zero detuning Δ but of different

intensity. A weak pulse of Rabi frequency Ω_w is perturbed and controlled by the simultaneous passage of a stronger pulse Ω_s through the sample. The physical case behind such a setup may involve a weaker pulse which produces a single-photon excitation that can in turn be controlled by a more intense XFEL pulse. In order to describe the fields in the counter-propagating geometry we consider a backward-forward decomposition of the radiation field [96],

$$\vec{E}(z,t) = E_w(z,t)e^{-i(\omega t - k_0 z)}\vec{e_x} + E_s(z,t)e^{-i[\omega t - k_0(L-z)]}\vec{e_x}\,. \tag{3.25}$$

In our case, since for each pulse only the respective forward scattering wave is taken into account, each term in the equation above represents the contribution of one of the pulses. For the numerical calculation we use the same decomposition also for the coherence terms

$$\rho_{eg}(z,t) = \rho_{egw}(z,t)e^{-i(\omega t - k_0 z)} + \rho_{egs}(z,t)e^{-i[\omega t - k_0(L-z)]}\,, \tag{3.26}$$

and the Rabi frequencies,

$$\Omega(z,t) = \Omega_w(z,t) + \Omega_s(z,t)\,. \tag{3.27}$$

Writing separately the wave equations for the forward and backward Rabi frequencies, we obtain the MBE

$$\begin{aligned}
\partial_t\rho_{ee} &= -\Gamma\rho_{ee} + \frac{i}{2}\left[(\Omega_w\rho_{gew} - \text{c.c.}) + (\Omega_s\rho_{ges} - \text{c.c.})\right.\\
&\quad \left. + (\Omega_w\rho_{ges}e^{-ik_0L+i2k_0z} - \text{c.c.}) + (\Omega_s\rho_{gew}e^{ik_0L-i2k_0z} - \text{c.c.})\right]\,,\\
\partial_t\rho_{gg} &= \Gamma\rho_{ee} - \frac{i}{2}[(\Omega_w\rho_{gew} - \text{c.c.}) + (\Omega_s\rho_{ges} - \text{c.c.})\\
&\quad + (\Omega_w\rho_{ges}e^{-ik_0L+i2k_0z} - \text{c.c.}) + (\Omega_s\rho_{gew}e^{ik_0L-i2k_0z} - \text{c.c.})]\,,\\
\partial_t\rho_{egw} &= -\left(i\Delta + \frac{\Gamma}{2}\right)\rho_{egw} - \frac{i}{2}\Omega_1(\rho_{ee} - \rho_{gg})\,,\\
\partial_t\rho_{egs} &= -\left(i\Delta + \frac{\Gamma}{2}\right)\rho_{egs} - \frac{i}{2}\Omega_2(\rho_{ee} - \rho_{gg})\,,\\
&\frac{1}{c}\partial_t\Omega_w + \partial_z\Omega_w = i\eta\rho_{egw}\,,\\
&\frac{1}{c}\partial_t\Omega_s - \partial_z\Omega_s = i\eta\rho_{egs}\,.
\end{aligned} \tag{3.28}$$

The MBE above can be solved numerically. For numerical efficiency, we consider instead of incident delta pulses in Eq. (3.17) a Gaussian pulse shape $\Omega(z,t) = \Omega_0 e^{-\frac{(t-\tau)^2}{\sigma^2}}$ with $\sigma = 1$ ns, which is still much shorter than the nuclear decay time

scale of hundreds of ns (the nuclear spontaneous decay rate is $\Gamma = 1/141$ GHz). As numerical example, the weak pulse with initial Rabi frequency $\Omega_{w0} = \Gamma/10$ reaches the sample ($z = 0$) at τ_w in the presence of a stronger pulse ($\Omega_{s0} = 200\Gamma$) arriving at other end of the sample ($L = 10$ μm) at τ_s with positive or negative time delay and propagating through the sample in the opposite direction. The effective thickness of the sample was chosen $\xi = 15$. The results for positive and negative time delay are presented in Figs. 3.2 and 3.5.

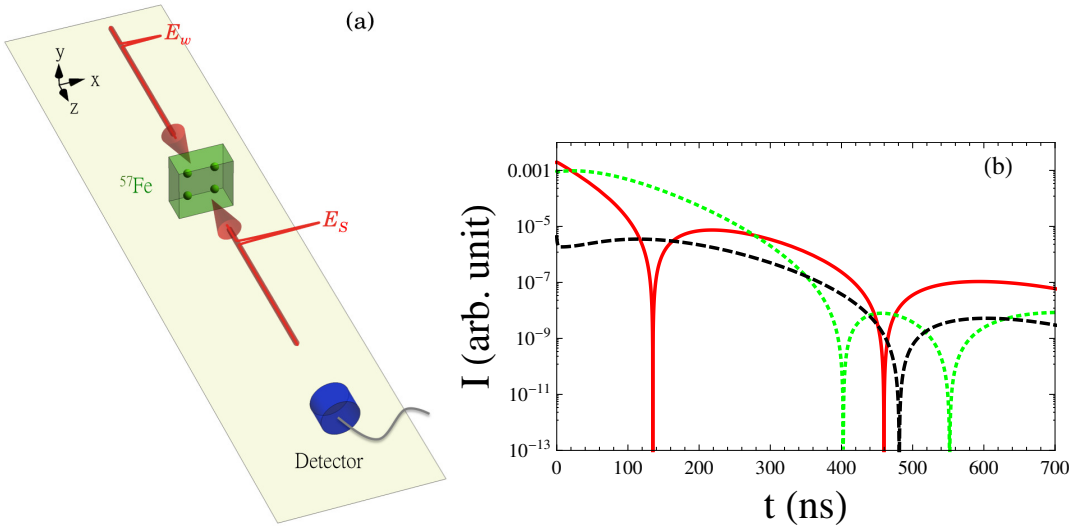

Figure 3.2: (a) Counter-propagating pulses setup with the strong pulse reaching the sample prior to the weak pulse. (b) NFS time spectra $I \propto |\Omega_w|^2$ for the weak pulse in the absence (red solid line) or presence of a stronger counter-propagating pulse Ω_s. The latter reaches the sample prior to the weak pulse. The time delay $\Delta\tau = \tau_s - \tau_w$ between the two pulses is -10 ns (green dotted line) and -50 ns (black dashed line). The time origin is set by the center of the incident weak pulse reaching the sample at $z = 0$.

We see that the presence of the stronger pulse plays an important role on the propagation of the weaker resonant pulse. In the following, we address the two situations of positive and negative pulse delay separately.

3.3.1 $\Delta\tau < 0$

The strong pulse passes the nuclear sample prior to the weak pulse. This situation is depicted in Fig. 3.2. We see that in this case the weak pulse signal can be suppressed by several orders of magnitude depending on the delay time $\Delta\tau$. The underlying mechanism for this suppression relies on two aspects: (i) the diminished nuclear ground state population left available for the later arriving weaker pulse and (ii) the building up of the weak pulse coherence term ρ_{egw}. The strong pulse produces a significant population of the excited states at $t = 0$ and the population dynamics is still ongoing by the time the weaker pulse reaches the sample. This is illustrated in Fig. 3.3 where the contour plot of the time-dependent excited state population produced by the strong pulse as a function of position in the sample z is presented. We see that at $t = 10$ ns and $t = 50$ ns after the passing of

the strong pulse, a still large amount of excitation is present in the sample and correspondingly fewer ground states are available for excitation by the weak pulse. However, this does not directly explain why the arrival of the weak pulse with 50 ns delay time leads to a more suppressed signal in Fig. 3.2(b) than the case of 10 ns delay, since the excited state population is higher in the latter case. A study of the MBE for the two counter-propagating pulses (3.28) reveals in the equation for the coherence ρ_{egw} that it is the population inversion $(\rho_{ee} - \rho_{gg})$ which is decisive for the intensity of the scattered signal. Indeed, the weak pulse itself can produce only a weak excitation such that $\rho_{ee} - \rho_{gg} \simeq -1$. The imaginary part of the coherence at $t = 0$ is then given by the product between the incident (here Gaussian) pulse and the difference $(\rho_{ee} - \rho_{gg})$. However, with the strong pulse arriving prior to the weak pulse, the nuclear population is first pumped in the excited state and $(\rho_{ee} - \rho_{gg})$ changes sign. A contour plot of the population inversion produced by the strong pulse is presented in Fig. 3.4. At $t = 10$ ns when the weak pulse reaches the sample, the population inversion is approx. 0.8, leading to a smaller absolute value of the imaginary part of the initial coherence ρ_{egw} for the weak pulse and a suppressed signal. If the weak pulse arrival is delayed up to 50 ns, the population inversion cancels with $\rho_{ee} - \rho_{gg} \simeq 0$ over most of the sample. The coherence $\mathrm{Im}[\rho_{egw}]$ and consequently the weak pulse signal is even more strongly suppressed. We note that the change of sign for the coherence term at $t = 0$ does not play a role here since it only affects the initial phase of the scattered electric field and not its intensity.

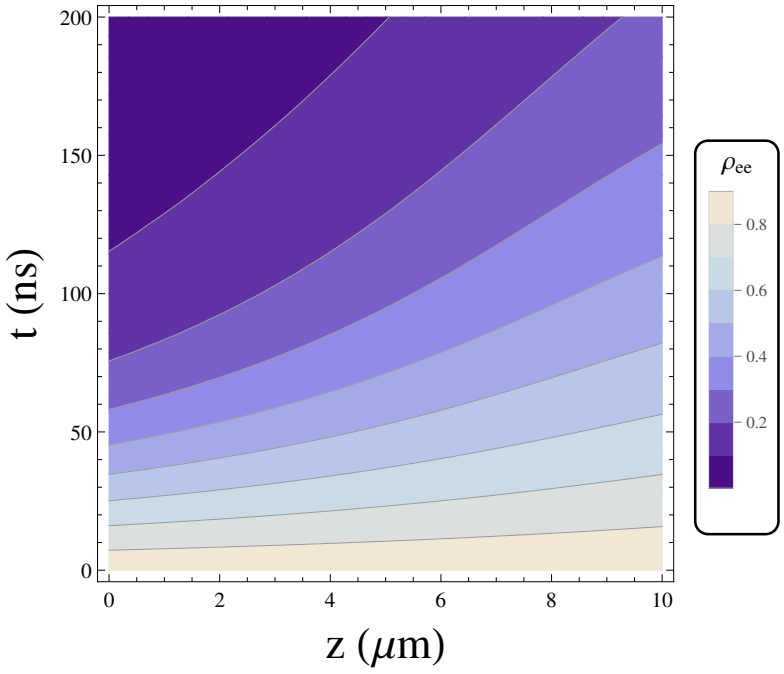

Figure 3.3: Excited state population ρ_{ee} produced solely by the strong pulse as a function of time (here $t = 0$ denotes the center of the strong pulse entering the sample) and position z in the sample.

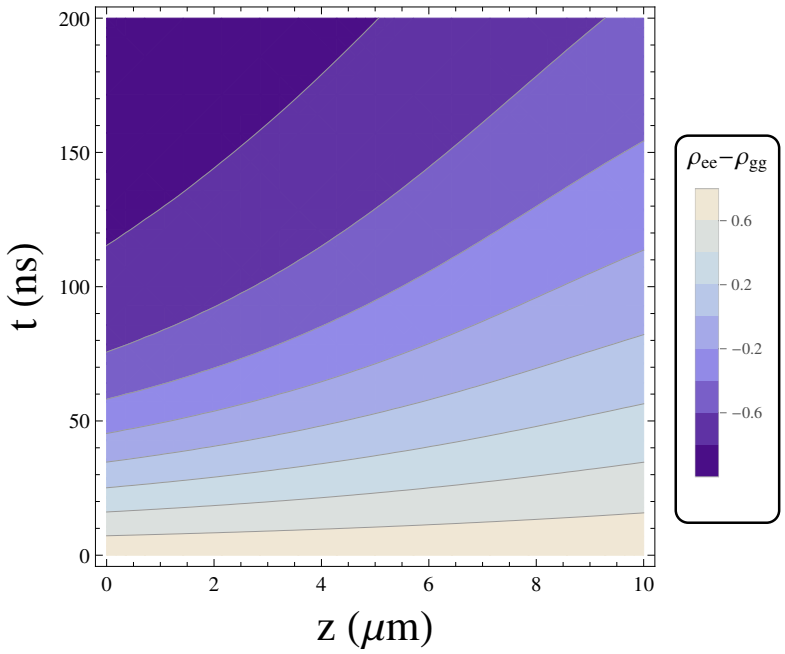

Figure 3.4: Population inversion ($\rho_{ee}-\rho_{gg}$) produced solely by the strong pulse as a function of time (here $t = 0$ denotes the center of the strong pulse entering the sample) and position z in the sample.

3.3.2 $\Delta\tau > 0$

The strong pulse arrives during the weak pulse propagation through the sample as shown in Fig. 3.5(a). Our results for this situation are depicted in Fig. 3.5(b). In this case the effect of the strong pulse arriving with a delay after the weak pulse is a substantial increase of the response of the latter. Similar arguments related to the strong-pulse-induced population inversion and coherence hold also in this case. However, the main difference now is that the weak pulse evolves first unperturbed and the coherence term ρ_{egw} is non-zero and decreases when the strong pulse arrives. Thus, unlike in the previous situation discussed above, a sudden change in the sign of the population inversion will produce now an increase of ρ_{egw} and consequently also an increase of the weaker pulse signal $|\Omega_w|^2$. The population inversion for both $\Delta\tau = 10$ ns and $\Delta\tau = 50$ ns has similar values leading to a comparable enhancements of the weak pulse signal for the green and the black curves in 3.5(b).

In order to further test our understanding of the two-pulse propagation dynamics in the nuclear sample, we have also considered a hypothetical modified setup where the effect of the strong pulse on the excited state population for the weak pulse vanishes. The concrete example is a three-level V-type system where the two pulses each couple only to one of the two transitions, leading to the population of two different excited states. The population inversion relevant for the weak pulse is therefore never changing sign, since $\rho_{eew} \ll \rho_{gg}$ at all times. As expected, we observe the suppression of the weak pulse signal for all (positive and negative) delay times, with no enhancement observed.

To summarize, prior arrival of a strong pulse can suppress while a later arrival

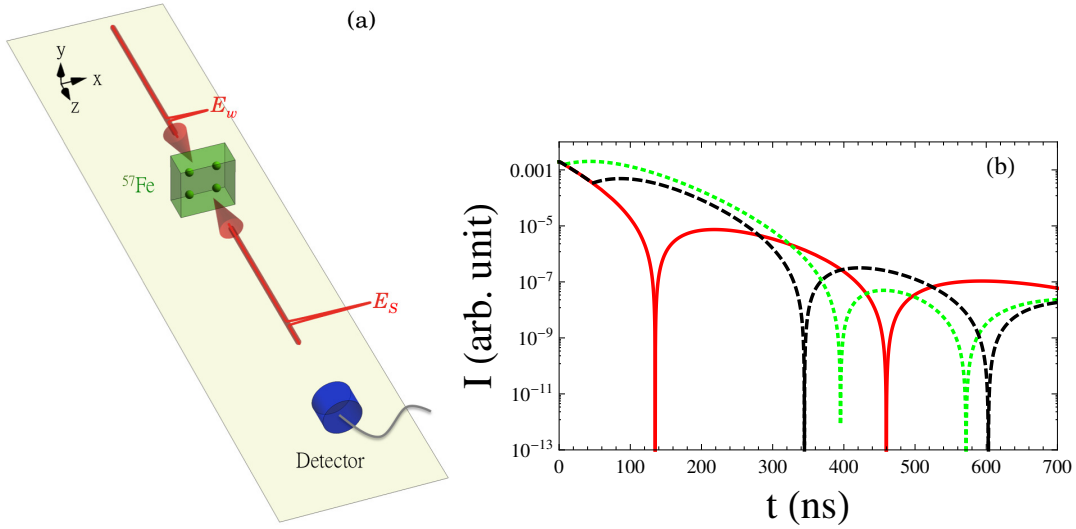

Figure 3.5: (a) Counter-propagating pulses setup with the weak pulse reaching the sample prior to the strong pulse. (b) NFS time spectra $I \propto |\Omega_w|^2$ for the weak pulse in the absence (red solid line) or presence of a stronger counter-propagating pulse Ω_s. The weak pulse reaches the sample first and $\Delta\tau = 10$ ns (green dotted line) and 50 ns (black dashed line). The time origin is again set by the center of the incident weak pulse reaching the sample at $z = 0$.

can enhance significantly the NFS signal of a weak pulse. This can have exciting applications in the framework of single-photon signal processing, for instance to enhance detection of single-photon wave packets. The key phenomenon here is the significant modification of the population inversion in the sample by the strong pulse. Obviously, in order to achieve the effects under investigation here, a certain intensity is required for the strong pulse. The value assumed here of $\Omega_{s0} = 200\Gamma$ corresponds to a peak intensity of 1.8×10^{22} W/cm^2, which is not far from present XFEL intensity values considering excellent focus [97]. However, a narrower bandwidth would be required which may be available only at future seeded XFEL facilities. For comparison, we present here our results also for a $\Omega_{s0} = 100\Gamma$ for $\Delta\tau = \pm 10$ ns in Fig. 3.6. In this case, the suppression and enhancement effects are visible but already less spectacular.

3.4 Forwarding the nuclear response in time

We now investigate the case when only one pulse propagates resonantly through the sample, however under the action of a time-dependent magnetic field. In the absence of the magnetic field, the ^{57}Fe nuclei behave as two-level systems. If the magnetic field is switched on, the introduced hyperfine splitting renders six transitions possible. We consider in the following a setup for which the incident pulse polarization and the geometry of the magnetic field, when present, allow only for the driving of the two $\Delta m = 0$ transitions. As further parameters, the magnetic field intensity of B=17.2 T and an effective thickness for the two-level nuclear system of $\xi = 40$ are envisaged. The hyperfine splitting effectively produces in this

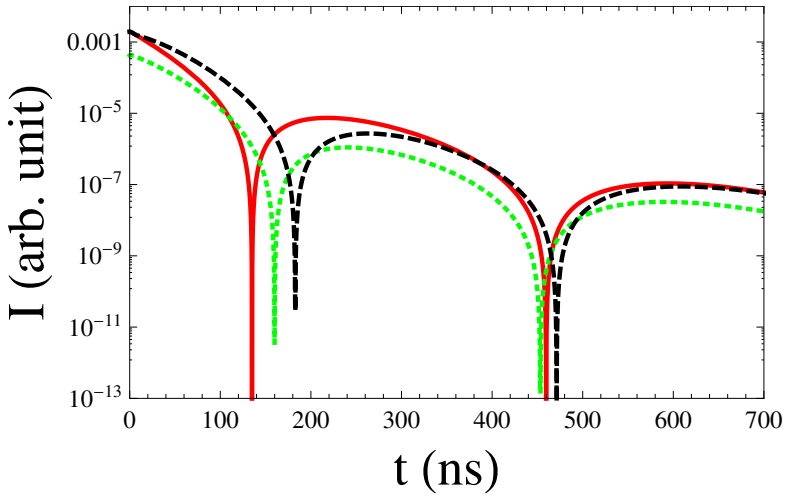

Figure 3.6: NFS spectra $|\Omega_w(L,t)|^2$ unperturbed (solid red line) and in the presence of a counter-propagating strong pulse with $\Omega_{s0} = 100\Gamma$ reaching the sample with the pulse delay $\Delta\tau = 10$ ns (green dotted line) and $\Delta\tau = -10$ ns (black dashed line).

case a shift to a smaller value of ξ since the ground state population distributes half-half over the two hyperfine-split ground states with $m_g = -1/2$ and $m_g = 1/2$. This is illustrated by the shapes of the dynamical beat in the NFS time spectra for the two cases in the presence and absence of the magnetic field presented in Fig. 3.7. The envelope of the quantum beat follows here the dynamical beat corresponding to $\xi = 20$.

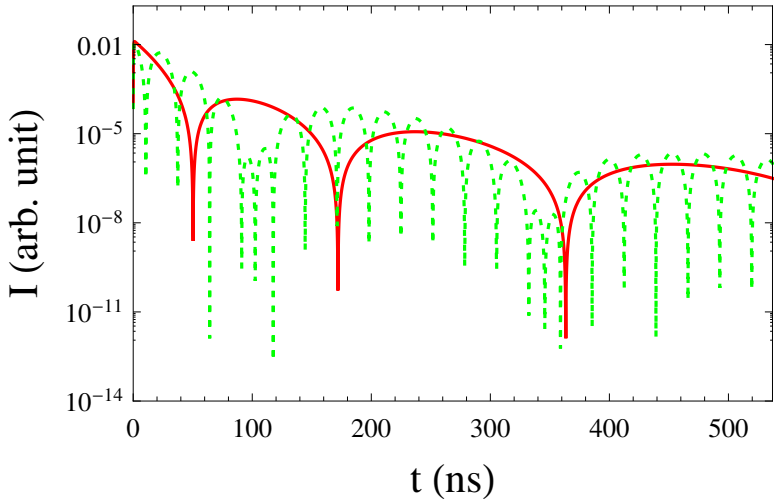

Figure 3.7: Intensity of the coherent scattered light for a single nuclear transition in the absence of hyperfine splitting and for an effective thickness of $\xi = 40$ (solid red line). In the presence of the magnetic field, the two $\Delta m = 0$ transitions interfere and introduce a quantum beat in the spectrum (green dotted line).

We now attempt to switch between the degenerate and non-degenerate nuclear level systems by turning the magnetic field on or off. Coherent storage of nuclear excitation has been theoretically shown to be possible when the magnetic field

present at $t = 0$ when the incident SR or XFEL pulse arrived is switched off at certain times. A by-product of the coherent storage is that the NFS signal appears to be shifted backwards in time. Here, we investigate the opposite situation. Initially, the incident pulse hits the ^{57}Fe sample in the absence of any hyperfine magnetic field. The magnetic field is switched on later, in our first example at $t_0 = 50$ ns, when the minimum of the dynamical beat is reached. Quantum beats then appear in the NFS spectrum as a result of the two hyperfine transitions that can constructively or destructively interfere. This situation is illustrated in Fig. 3.8(a) by the black line. The signal for $t < 50$ ns can be described by $\xi[J_1(2\sqrt{\xi\Gamma t})]^2 e^{-\Gamma t}/(\Gamma t)$ where $\xi = 40$. Later on, after the hyperfine magnetic field has been switched on, the envelope illustrated in Figs. 3.8(b) by the red curve can be described as $[\xi'[J_1(2\sqrt{\xi'\Gamma(t+t_0)})]^2 e^{-\Gamma t}/(\Gamma(t+t_0))$ where $\xi' = \xi/2$. The comparison between the case with magnetic field at all times and magnetic field only after $t = 50$ ns is presented for the NFS spectra and the real and imaginary parts of the coherence term ρ_{42} in Figs. 3.8(a), (c) and (d).

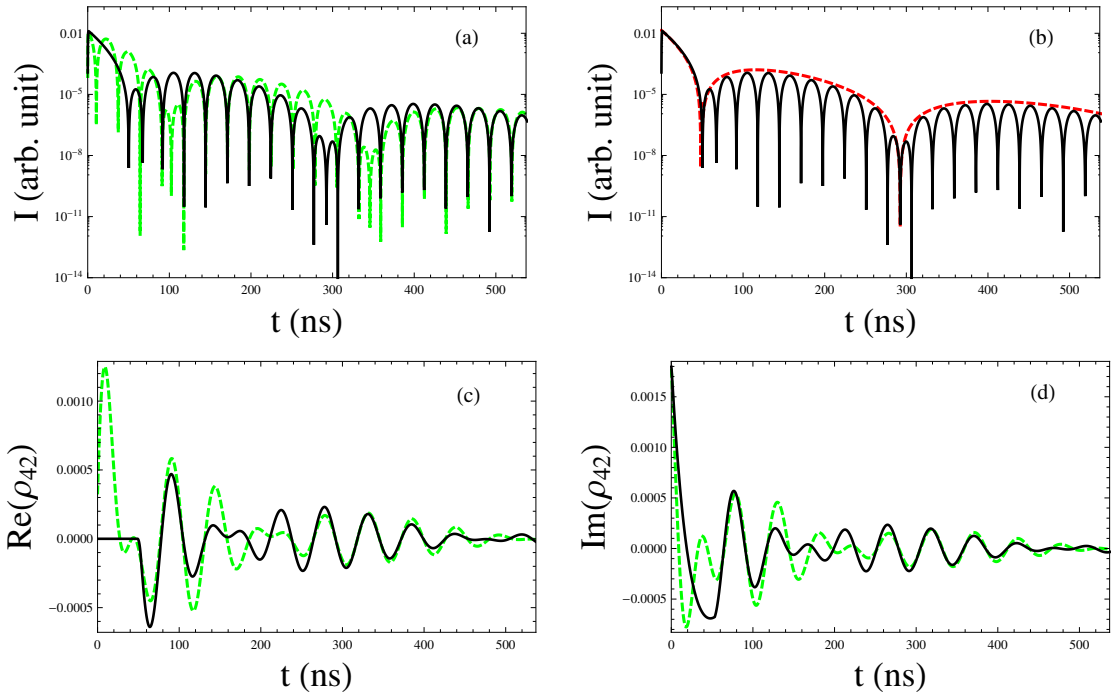

Figure 3.8: NFS time spectra (a,b) and the real (c) and imaginary (d) parts of the coherence term ρ_{42}. The dashed green line depicts the case of scattering in the presence of a magnetic field at all times, while the black line presents the case of the magnetic field being switched on rapidly at $t = 50$ ns. Correspondingly a 50 ns shift of the signal can be observed. The red solid line in (b) illustrates for comparison the dynamical beat envelope for $\xi = 20$ as discussed in the text.

The surprising feature of the two NFS spectra in the presence of magnetic field in Figs. 3.8 is that the system dynamics, including both the scattered signal and the coherence terms, is identical and just *shifted in time* up to the effect of the exponential spontaneous decay. Indeed, a numerical comparison of the unperturbed

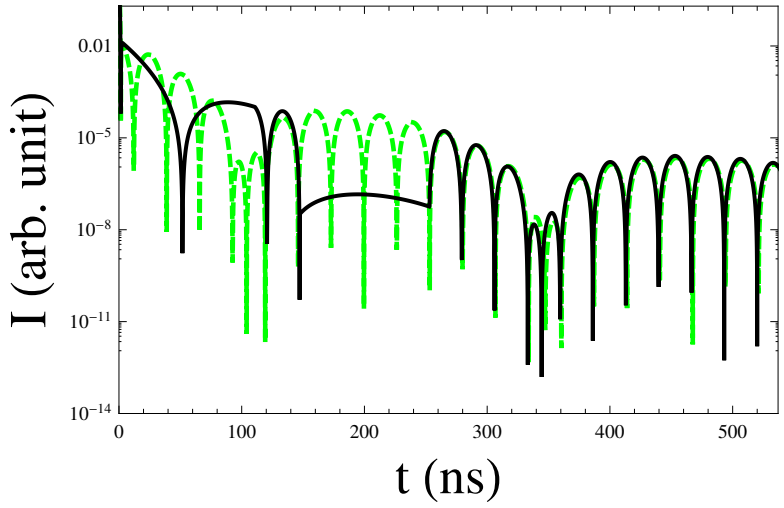

Figure 3.9: NFS time spectra for a hyperfine splitting constant in time (green dashed line) compared to the switching scheme turning the magnetic field on ($t_1 = 105$ ns), off ($t_2 = 145$ ns), and on again ($t_3 = 251$ ns), described in the text (black line).

and shifted spectra shows that they coincide when considering the 50 ns time shift and accounting for the corresponding spontaneous decay. Turning on of the magnetic field after the incident radiation pulse thus displaces the signal forward by the same time interval Δt=50 ns compared to the spectrum with constant hyperfine splitting. This is the opposite effect compared to the coherent photon storage presented in Ref. [25]. In order to demonstrate this, we design a succession of four manipulations on the magnetic field in order to produce the forward shift of the signal and the coherent storage. The results are illustrated in Fig. 3.9. The incident pulse reaches the nuclear sample at $t_0 = 0$ when there is no magnetic field present and no hyperfine splitting in the sample. Later on, at $t_1 = 105$ ns, the magnetic field is switched on rapidly and the quantum beats occur. At a later time, when a quantum beat minimum is reached ($t_2 = 145$ ns), the magnetic field is switched off again and coherent storage [25] is achieved. The effect of the coherent storage is to shift now the signal backwards, i.e., towards longer scattering times, thus canceling the effect of the first signal shift forward in time. Finally, at $t_3 = 251$ ns the magnetic field is switched on and we retrieve the NFS signal which matches exactly the situation when the magnetic field was on during the whole scattering period, as shown in Fig. 3.9. The shifts forwards and backwards in time cancel each other since $t_0 - t_1 \simeq t_3 - t_2$. We would like to emphasize here that, just as in the case of coherent photon storage [25], shifting the signal forwards in time occurs preserving the phase information, i.e., we witness the phase-sensitive shift of the signal in time.

Thus, temporal signal control can be achieved via fast switching on and off of the magnetic field. The experimental challenges for the control on ns time scale of strong magnetic fields have been first addressed in Ref. [25]. The most promising solution involves a material with no intrinsic nuclear Zeeman splitting like stainless steel $Fe_{55}Cr_{25}Ni_{20}$ [88, 98]. The challenge is to turn off and on the external magnetic

fields of few Tesla on the ns time scale. According to the calculations presented in Ref. [25], the raising time of the **B** field should be shorter than 50 ns (the raising time was considered 4 ns for all presented cases). This could be achieved by using small single- or few-turn coils and a moderate pulse current of approximately 15 kA from low-inductive high-voltage "snapper" capacitors [99]. Another mechanical solution, e.g., the lighthouse setup [100] could be used to move the excited target out of and into a region with confined static **B** field. The nuclear lighthouse setup is based on a rotating sample. This changes the direction of the coherently emitted photon which is always in the forward direction with respect to the sample, thus explaining the name "lighthouse effect". The rotation can be used to bring the sample in and outside a region with confined static magnetic field. The switching time is then given by the time needed for the rotation of the sample from the edge of the confined magnetic field region to the outside, magnetic-field free region. With the setup illustrated in Fig. 3.10, we estimate that a rotor with rotational frequencies ω_R of up to 70 kHz and a diameter of few mm [100] is fast enough to rotate the sample out a depth of few μm in a few tens of ns. If mastered, this fast magnetic-field switching would allow elaborated coherent control over the nuclear excitation in NFS and accordingly over the dynamics of single x-ray photon wave packets.

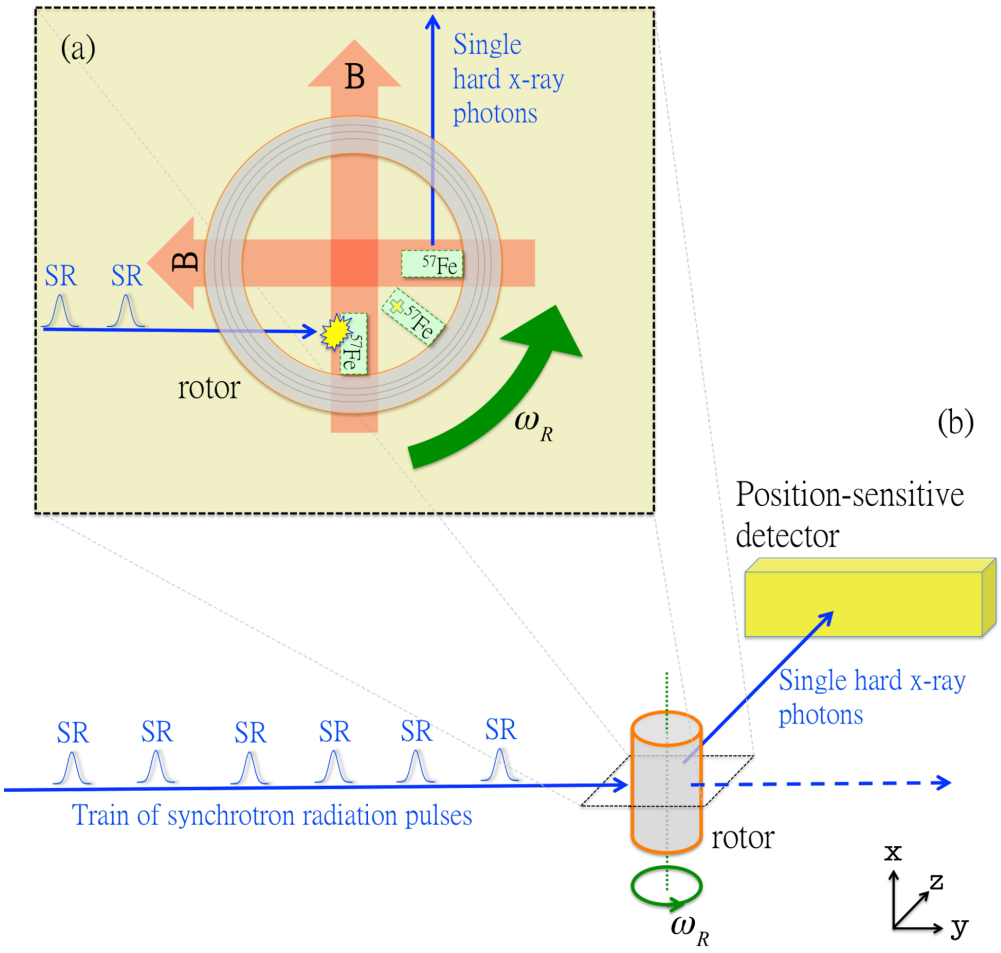

Figure 3.10: Sketch of the lighthouse setup for the coherent storage of hard x-ray single photons [89, 93]. (a) Bird view of the lighthouse setup. Gray area depicts the side view of the rotor rotating with angular frequency ω_R, the two red wide arrows illustrate the regions with confined static magnetic field $\mathbf{B}$ and the blue arrows are the trajectories of SR and emitted single hard x-ray photons. The light green rectangles depict snapshots of the rotating ^{57}Fe target attached on the inner surface of the rotor. (b) The geometric arrangement of the lighthouse scheme.

Chapter 4

Collective magnetic hyperfine splitting in single x-ray photon superradiance

In Chapter 3, we studied the coherent control tools of single x-ray photon superradiance in NFS. Due to the large thickness of the sample, the timed Dicke state can not be generated and the effects predicted in Chapter 2 are not valid in this regime. In this Chapter, a thin-film x-ray cavity with embedded ^{57}Fe nuclei probed by x-ray pulse at grazing incidence is investigated. The thickness of the nuclear layer is on the scale of several nanometers and it is much smaller than the wavelength of the cavity field. This means this case is similar to the limit case of $R \ll \lambda$ which has been studied in Chapter 2. Here, we introduce another model to describe the dynamics of the thin-film cavity system, following the approach in Ref. [33]. It is shown that the eigenvalues of the thin-film cavity system obtained by this new model are consistent with the ones derived in Sec. 2.2. Moreover, we can reproduce the results obtained in Sec. 2.2. We show that the main effects in Sec. 2.2, such as the EIT-like spectrum and the broadened magnetic hyperfine splitting, are observable in the thin-film x-ray cavity with embedded nuclei under experimental parameters available already today.

4.1 Motivation and introduction

4.1.1 Motivation

In Sec. 2.2, we have presented some interesting effects based on the collective magnetic hyperfine splitting in single-photon superradiance. However, it is not easy to observe such effects in an ensemble of atoms. The most recent experiment that observed the collective Lamb shift was performed in a thin-film x-ray cavity using nuclear ensembles [11]. In that experiment, a ^{57}Fe layer was placed at the antinode of the standing wave in the cavity as shown in Fig. 4.1. The limit $R \ll \lambda$ can be transformed to $R_t \ll \lambda_0$ where R is the size of the sample, λ is the wavelength of the photon, R_t is the thickness of the sample and λ_0 is the wavelength of the cavity field. It is obvious that this limit is true in the setup in Fig. 4.1. The ensemble is so thin that the excitation probabilities for all nuclei within the

ensemble are practically the same. Therefore the timed Dicke state [60]

$$|\psi_0\rangle = \frac{1}{\sqrt{N}} \sum_{j=1}^{N} e^{i\vec{k}_C \cdot \vec{r}_j} |g_1 g_2 ... e_j ... g_N\rangle |0\rangle \,. \tag{4.1}$$

can be produced by the resonant probe x-ray pulse. The position of the excited nucleus is given by $\vec{r}^{(j)}$ and $\vec{k}_C$ represents the total wave vector for the cavity field.

4.1.2 Introduction to the thin-film x-ray cavity

X-rays can be guided through small channels of low electron density material embedded in a cladding material with higher electron density. A thin-film x-ray cavity is typically built by a heap of stratified materials. A low-density guiding layer is coated on a substrate with higher electron density in a planar geometry. The electron density can be replaced by the refractive index upon the incidence of the x-ray light. Refractive-index modulations guide the reflection at the confining boundaries and result in a propagation mode in the structure. The thickness of the guided layers is on the order of a few nanometers. A representative system is shown in Fig. 4.1(a). A material of low electron density (carbon) is sandwiched between two layers of high electron density (palladium). The specific parameters for the cavity are Pd(5 nm)/C(20 nm)/^{57}Fe(1 nm)/C(20 nm)/Pd. The layers of Pd act as mirrors and the incident x-rays under a grazing angle are repeatedly reflected at the boundaries. Due to the multi-beam interference between the incident and the reflected waves, a standing wave forms at a given incidence angel [see Fig. 4.1(b)]. Depending on the film thickness, a certain number of guided modes can be excited at different incidence angles where the reflectivity reaches a deep minimum [see Fig. 4.1(c)]. In Fig. 4.1(a), a thin ensemble of ^{57}Fe nuclei is placed at the center of carbon at the antinode of the standing wave under an incidence angle of $\varphi = 3.47\,\text{mrad}$. As shown in Fig. 4.1(c), a substantial intensity enhancement is achieved at the antinode of the standing wave. This makes the cavity a very useful platform to study both x-rays and the resonant nuclear transition of ^{57}Fe.

4.2 Theoretical model for the thin-film x-ray cavity

In this Section, we introduce a quantum model for describing the dynamics of one ^{57}Fe layer placed in the thin-film cavity probed by hard x-rays at grazing incidence [33]. An externally applied magnetic field which is perpendicular to the propagation direction $\hat{k}$ induces the hyperfine splitting of the ground and excited ^{57}Fe nuclear states [22]. The input-output formalism [101] is also presented.

4.2.1 Collective nuclear states

A single ^{57}Fe layer placed in a planar cavity for hard x-rays similar to the setup in Ref. [11] is probed by the x-ray pulse at grazing incidence, as shown in Fig. 4.2. We envisage a hyperfine magnetic field perpendicular to the x-ray propagation direction $\hat{k}$ that induces the hyperfine splitting of the ground and excited ^{57}Fe

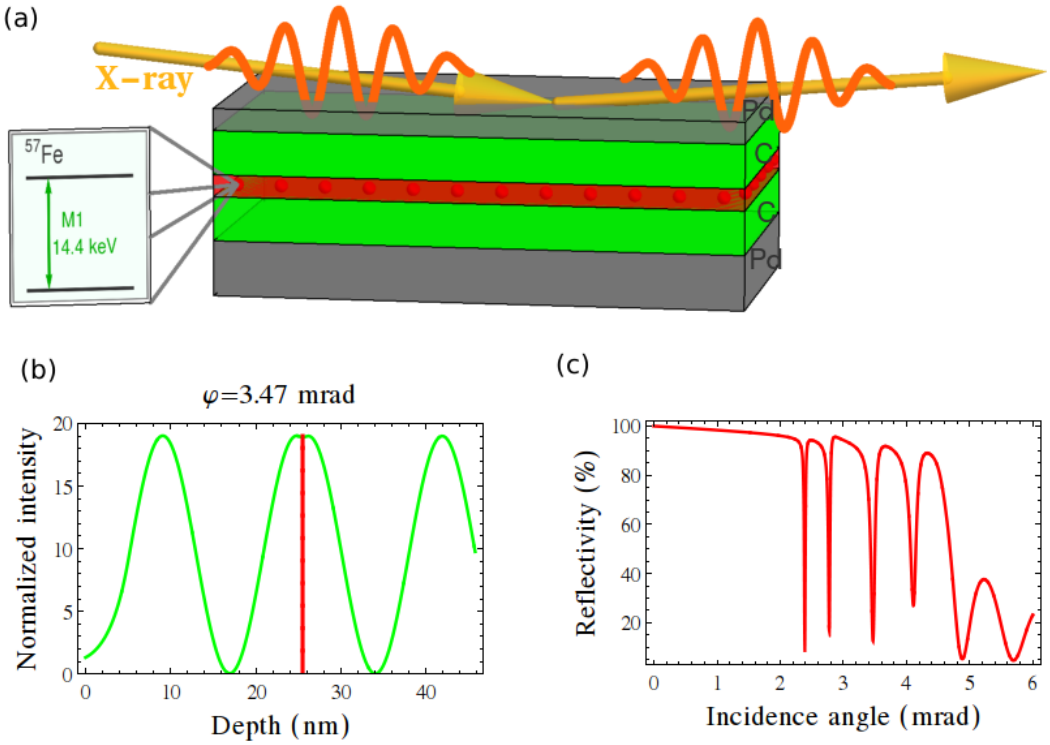

Figure 4.1: (a) Schematic of the setup: A thin-film cavity containing resonant $^{57}\mathrm{Fe}$ nuclei is probed by x-ray pulses under grazing incidence. (b) The normalized intensity of the field as a function of the position in the cavity under the incidence angle $\varphi = 3.47\,\mathrm{mrad}$. The red line stands for the position of the nuclear layer. (c) The reflection curve of the thin-film x-ray cavity as a function of the incidence angle φ. The dips represent the resonant cavity modes. For example, the third cavity mode is resonant when the incidence angle is $3.47\,\mathrm{mrad}$.

nuclear states [22]. The stable ground state of ^{57}Fe (nuclear spin $I_g = 1/2$) is then split into a doublet with $m_g = \pm 1/2$ and the first excited state at 14.4 keV (nuclear spin $I_e = 3/2$, mean lifetime τ_0=141 ns) into a quadruplet with $m_e = \pm 1/2, \pm 3/2$. Depending on the polarization of the incident light, specific transitions between the six hyperfine-split nuclear states will be driven. In the following, we consider a linearly polarized x-ray pulse such that only the two $\Delta m = m_e - m_g = 0$ transitions can be driven.

We describe the hyperfine level scheme in terms of the collective states of the N-nuclei ensemble in the cavity. Initially, the nuclei are in the collective ground state

$$|G\rangle = \underbrace{|g_1^{(1)}\rangle \dots |g_1^{(N_1)}\rangle}_{N_1} \underbrace{|g_2^{(N_1+1)}\rangle \dots |g_2^{(N)}\rangle}_{N_2}, \tag{4.2}$$

where $|g_1\rangle$ and $|g_2\rangle$ denote the two ground magnetic sublevels and N_i is the number of nuclei in the ground state $|g_i\rangle$ $(i \in 1, 2)$, $N_1 + N_2 = N$ and $N_1 \approx N_2$ at room temperature. Current experiments employing the 14.4 keV resonance line in ^{57}Fe are mostly performed at modern SR light sources. Typically, in SR pulses at most only one photon will be resonant to the ^{57}Fe nuclear transition. We define the excited state as a timed Dicke state [60]

$$|E_\mu\rangle = \frac{1}{\sqrt{N_\mu}} \sum_j^{N_\mu} e^{i\vec{k}_C \cdot \vec{r}^{(j)}} |g_1^{(1)}\rangle \dots |e_\mu^{(n)}\rangle \dots |g_2^{(N)}\rangle \tag{4.3}$$

in which the nth atom has been excited by the transition μ, with the notation $\mu = 1$ for the transition $m_g = -1/2 \to m_e = -1/2$ and $\mu = 2$ for $m_g = 1/2 \to m_e = 1/2$, depending on the initial ground state spin projection m_g. The excited state in Eq. (4.3) is treated as the initial state in Sec. 2.2 and the radiation spectrum obtained in Sec. 2.2 are based on this state. The two $\Delta m = 0$ transitions are equivalent in this system to the two transitions $|3\rangle \to |1\rangle$ and $|3\rangle \to |2\rangle$, where we have used the notation $|3\rangle$ for $|G\rangle$, $|1\rangle$ for $|E_1\rangle$ and $|2\rangle$ for $|E_2\rangle$, respectively, as illustrated in the inset panel in Fig. 4.2. The two transitions experience vacuum-mediated coupling by spontaneously generated coherence terms [22, 23].

4.2.2 Density matrix formalism

We use the master equation to describe the dynamics of the system [33]

$$\frac{d}{dt}\rho = -i[H_M + H_N, \rho] + L_M[\rho] + L_{SE}[\rho]. \tag{4.4}$$

The Hamiltonian consists of two parts: one is the interaction between the incident pulse and the cavity H_M and the other is the interaction between the cavity and the resonant nuclei H_N. Moreover, $L_M[\rho]$ accounts for the loss of the cavity and $L_{SE}[\rho]$ for the spontaneous emission, respectively. In the interaction picture, the Hamiltonian corresponding to the x-ray-cavity interaction can be written as follows

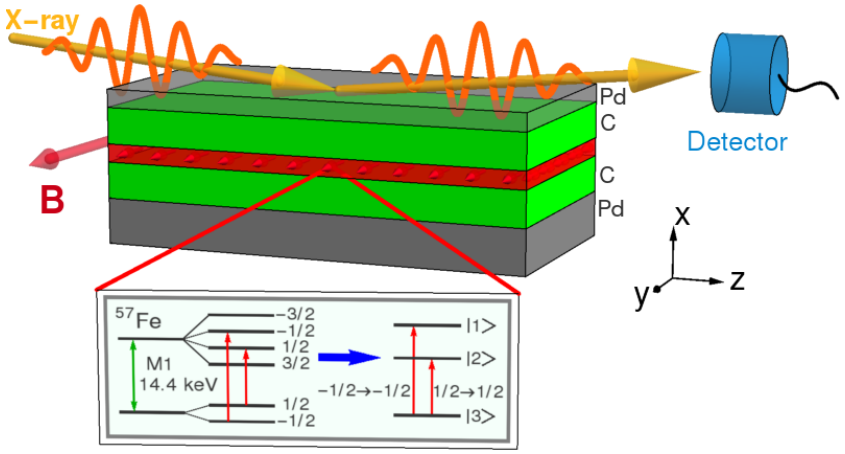

Figure 4.2: Thin-film planar cavity setup with x-ray grazing incidence. The cavity consists of a sandwich of Pd and C layers with a 1 nm layer containing ^{57}Fe placed at the antinode of the cavity. The nuclei experience a hyperfine magnetic field B (red horizontal arrow). Inset panel: ^{57}Fe level scheme with hyperfine splitting. This is equivalent with a V-like three-level scheme comprising the common ground state (4.2) and the two excited states (4.3).

[33]:

$$H_M = \Delta_C a_1^+ a_1 + \Delta_C a_2^+ a_2 + i\sqrt{2\kappa_R}[(\hat{a}_1^* \cdot \hat{a}_{in}) a_{in} a_1^+ - (\hat{a}_{in}^* \cdot \hat{a}_1) a_{in}^* a_1 + (\hat{a}_2^* \cdot \hat{a}_{in}) a_{in} a_2^+ - (\hat{a}_{in}^* \cdot \hat{a}_2) a_{in}^* a_2] \,. \tag{4.5}$$

Here, Δ_C is the cavity detuning, a (a^+) is the photon annihilation (creation) operator and a_1, a_2 represent the two different modes defined according to the polarization state of the photon. Furthermore, κ_R denotes the x-ray coupling strength into the cavity mode, and a_{in} characterizes the driving field of the cavity mode by the external (classical) x-ray field. The products $(\hat{a}_i^* \cdot \hat{a}_j)$ are scalar products between two different polarization unit vectors.

On the other hand, the cavity-nucleus interaction Hamiltonian reads

$$H_N = -\Delta \sum_\mu |E_\mu\rangle\langle E_\mu| - \sum_\mu \Delta_\mu |E_\mu\rangle\langle E_\mu| + \sum_{j=1}^{2} \sum_\mu \left[(\hat{d}_\mu^* \cdot \hat{a}_j) c_\mu \sqrt{N_\mu} g |E_\mu\rangle\langle G| \, a_j + (\hat{a}_j^* \cdot \hat{d}_\mu) c_\mu \sqrt{N_\mu} g^* a_j^+ |G\rangle\langle E_\mu| \right] . \tag{4.6}$$

In the expression above, Δ is the detuning between the x-ray field and the bare transition energy of the nuclei, and Δ_μ is the energy difference induced by the hyperfine splitting. The normalized dipole moment $\hat{d}_\mu$ of transition μ is defined with respect to the quantization axis of nuclei, i.e., the orientation of the magnetic hyperfine field B. Furthermore, g is the coupling strength between the ensemble and the cavity and c_μ denotes the corresponding Clebsch-Gordan coefficient.

The thin-film cavity considered in this work has a low quality factor which means the decay rate of the cavity κ is much larger than the atom-field coupling strength g. Thus, we can eliminate the cavity modes adiabatically, i.e., we set $\frac{d}{dt} a_j = 0$.

The Heisenberg equation of motion for the operator a_j then reads

$$\frac{d}{dt}a_j = i[H_M + H_N, a_j] - \kappa a_j = 0\,. \tag{4.7}$$

Introducing the expressions (4.5) and (4.6) into Eq. (4.7), we obtain

$$a_j = \frac{\sqrt{2\kappa_R}(\hat{a}_j^*\cdot\hat{a}_{in})a_{in} - i\sum_\mu(\hat{a}_j^*\cdot\hat{d}_\mu)c_\mu\sqrt{N_\mu}g^*|G\rangle\langle E_\mu|}{\kappa + i\Delta_C}\,. \tag{4.8}$$

Inserting the expression (4.8) into the Hamiltonian terms (4.5) and (4.6), we can obtain the master equation (4.4) in another form (see also [33])

$$\frac{d}{dt}\rho = -i[H_0 + H_\Omega + H_{LS}, \rho] + L_{cav}[\rho] + L_{SE}[\rho]\,, \tag{4.9}$$

with the following notations

$$H_0 = -\Delta\sum_\mu|E_\mu\rangle\langle E_\mu| - \sum_\mu\Delta_\mu|E_\mu\rangle\langle E_\mu|\,,$$

$$H_\Omega = \Omega\sum_\mu(\hat{d}_\mu^*\cdot\mathbb{1}_\perp\cdot\hat{a}_{in})c_\mu\sqrt{N_\mu}g|E_\mu\rangle\langle G| + H.c.\,,$$

$$H_{LS} = \delta_{LS}\sum_{\mu,\nu}(\hat{d}_\mu^*\cdot\mathbb{1}_\perp\cdot\hat{d}_\nu)c_\mu c_\nu|g|^2\sqrt{N_\mu N_\nu}|E_\mu\rangle\langle E_\nu|\,,$$

$$L_{cav}[\rho] = -\zeta_S\sum_{\mu,\nu}(\hat{d}_\mu^*\cdot\mathbb{1}_\perp\cdot\hat{d}_\nu)c_\mu c_\nu|g|^2\sqrt{N_\mu N_\nu}L[\rho, |E_\mu\rangle\langle G|, |G\rangle\langle E_\nu|\,]\,,$$

$$L_{SE}[\rho] = -\frac{\gamma}{2}\sum_\mu L[\rho, |E_\mu\rangle\langle G|, |G\rangle\langle E_\mu|\,]\,. \tag{4.10}$$

The Lindblad operator $L[\rho, O^+, O^-]$ introduced in Eq. (4.10) is defined as

$$L[\rho, O^+, O^-] = (O^+O^-\rho + \rho O^+O^- - 2O^-\rho O^+)\,, \tag{4.11}$$

where O^+ and O^- are arbitrary operators. Here, $\mathbb{1}_\perp = \hat{a}_1\hat{a}_1^* + \hat{a}_2\hat{a}_2^*$ with the mode operators connected by an outer product rather than a scalar product. The transition dipole moments are thus not coupled to the polarization of the external beam by a direct scalar product. The direction vectors are mediated via the tensor $\mathbb{1}_\perp$ which reflects the intermediate light propagation in the two eliminated modes. γ is the spontaneous decay rate and the other parameters in Eqs. (4.10) are defined as

$$\Omega = \frac{\sqrt{2\kappa_R}a_{in}}{\kappa + i\Delta_C}\,,$$

$$\delta_{LS} = -\frac{\Delta_C}{\kappa^2 + \Delta_C^2}\,,$$

$$\zeta_S = \frac{\kappa}{\kappa^2 + \Delta_C^2}\,. \tag{4.12}$$

4.2.3 Input-output relations

In an experiment, the reflected (a_{out}) and transmitted (b_{out}) beams can be observed. We can calculate these output field operators by using the input-output formalism. Assuming polarization-sensitive detection with detector polarization a_{out}, the observable operators read [33]

$$a_{out} = -a_{in}(\hat{a}^*_{out}\cdot\hat{a}_{in}) + \sqrt{2\kappa_R}[(\hat{a}^*_{out}\cdot\hat{a}_1)a_1 + (\hat{a}^*_{out}\cdot\hat{a}_2)a_2]\,, \tag{4.13}$$

$$b_{out} = \sqrt{2\kappa_T}[(\hat{a}^*_{out}\cdot\hat{a}_1)a_1 + (\hat{a}^*_{out}\cdot\hat{a}_2)a_2]\,. \tag{4.14}$$

With the introduced output field operators, we can easily calculate the reflection or the transmission coefficients by

$$R = \langle a_{out}\rangle / a_{in}\,, \tag{4.15}$$

$$T = \langle b_{out}\rangle / a_{in}\,. \tag{4.16}$$

Focusing on the reflectivity, the reflection coefficient can be simplified as follows [33]

$$R = \left(\frac{2\kappa_R}{\kappa + i\Delta_C} - 1\right)\hat{a}^*_{out}\cdot\hat{a}_{in} - \frac{i}{a_{in}}\frac{\sqrt{2\kappa_R}}{\kappa + i\Delta_C}\sum_\mu(\hat{a}^*_{out}\cdot\mathbb{1}_\perp\cdot\hat{d}_\mu)c_\mu\sqrt{N_\mu}g^*\langle E_\mu|\rho|G\rangle\,. \tag{4.17}$$

The reflected (or transmitted) intensity $|R|^2$ ($|T|^2$) in the thin-film cavity system can be detected in the experiment.

4.3 Collective magnetic hyperfine splitting of nuclei

In this Section, we use the theoretical model introduced in Sec. 4.2 to derive the collective effects of single x-ray photon superradiance with magnetic hyperfine splitting in the thin-film cavity system. The main results here are consistent with those we have already obtained in a more general in Sec. 2.2.

4.3.1 Collective Lamb shift and superradiance in the absence of magnetic field

We only consider the two $\Delta m = 0$ transitions and the Clebsch-Gordan coefficient for these two transitions is $\sqrt{2/3}$. We assume the ground-state populations are equal at room temperature. Then the Hamiltonian and the incoherent decay of

the system in Eq. (4.10) read

$$H_0 = -(\Delta+\phi)|E_1\rangle\langle E_1| - (\Delta-\phi)|E_2\rangle\langle E_2|\,,$$

$$H_\Omega = \sqrt{\frac{N}{3}}g\Omega\left(|E_1\rangle\langle G| + |E_2\rangle\langle G|\right) + H.c.\,,$$

$$H_{LS} = \frac{N}{3}|g|^2\delta_{LS}\left(|E_1\rangle\langle E_1| + |E_2\rangle\langle E_2| + |E_1\rangle\langle E_2| + |E_2\rangle\langle E_1|\right)\,,$$

$$L_{cav}[\rho] = -\frac{N}{3}|g|^2\zeta_S\left(L[\rho, |E_1\rangle\langle G| + |E_2\rangle\langle G|, |G\rangle\langle E_1| + |G\rangle\langle E_2|\,]\right)\,,$$

$$L_{SE}[\rho] = -\frac{\gamma}{2}\left(L[\rho, |E_1\rangle\langle G|, |G\rangle\langle E_1|\,] + L[\rho, |E_2\rangle\langle G|, |G\rangle\langle E_2|\,]\right)\,, \tag{4.18}$$

where $\phi = \frac{1}{2}(\delta_g + \delta_e)$. Here δ_g (δ_e) denotes the energy difference between two adjacent ground (excited) sub-states.

The theoretical model presented here can be also used to study the case without hyperfine splitting [33]. In the absence of the magnetic field, in fact there is no hyperfine splitting. However, we can still consider there are two $\Delta m = 0$ transitions in this case and the energy difference between the two transitions is zero. Corresponding to the Hamiltonian in Eq. (4.18), it means the parameter ϕ is zero. Introduce the state [33]

$$|+\rangle = \sqrt{\frac{1}{2}}|E_1\rangle + \sqrt{\frac{1}{2}}|E_2\rangle\,, \tag{4.19}$$

and we obtain [33]

$$H_\Omega = \sqrt{\frac{2}{3}N}\Omega g|+\rangle\langle G| + H.c.\,,$$

$$H_{LS} = \frac{2}{3}N\delta_{LS}|g|^2|+\rangle\langle +|\,,$$

$$L_{cav}[\rho] = -\frac{2}{3}N|g|^2\zeta_S L[\rho, |+\rangle\langle G|, |G\rangle\langle +|]\,. \tag{4.20}$$

We assume the populations are in the linear response $|G\rangle\langle G| = 0$ and $|+\rangle\langle +| = 0$. The assumption is reasonable because the x-ray pulse is very weak. Then we obtain the reflection coefficient given by Eq. (4.17) [33]

$$R = \left(\frac{2\kappa_R}{\kappa + i\Delta_C} - 1\right)\hat{a}^*_{out}\cdot\hat{a}_{in}$$

$$- \frac{i}{a_{in}}\frac{\sqrt{2\kappa_R}}{\kappa + i\Delta_C}\frac{(\hat{a}^*_{out}\cdot\hat{a}_{in})\frac{2}{3}N|g|^2\Omega}{\Delta - \frac{2}{3}N|g|^2\delta_{LS} + i\left(\frac{\gamma}{2} + \frac{2}{3}N|g|^2\zeta_S\right)}\,. \tag{4.21}$$

The first term of the reflection coefficient in Eq. (4.21) is caused by electronic scattering from the cavity. The second term stands for the reflection from the nuclei. We introduce the notations

$$C = \frac{2}{3}N|g|^2|\delta_{LS}\,,$$

$$\gamma_S = \gamma + \frac{4}{3}N|g|^2\zeta_S\,. \tag{4.22}$$

We find that C represent a frequency shift of the nuclei which is the collective Lamb shift [33, 60] and γ_S is the enhanced spontaneous decay rate [7]. Both the collective Lamb shift C and the superradiance decay rate γ_S have been observed experimentally in the thin-film x-ray cavity system [11]. We have obtained the values of the collective Lamb shift and the superradiance decay in the absence of the magnetic field. The next step is to derive the eigenvalues of the system in terms of these two values.

4.3.2 Eigenvalues of the system

Let us now consider the eigenvalues of the thin-film cavity with the embedded ^{57}Fe nuclear layer. We neglect the parts which denotes the contribution to the Hamiltonian (4.10) by the x-ray pulse, because the probe pulse is so weak that it will not change the eigenstates and eigenvalues of the system. When we calculate the eigenvalues of the system, we take into account not only the Hamiltonian but also the incoherent part $L_{cav}[\rho]$ and $L_{SE}[\rho]$ (4.10). We define the non-Hermitian operator of the thin-film cavity system

$$S_{\text{system}} = -iH' - \frac{\gamma_S}{2}\left(|E_1\rangle\langle E_1| + |E_2\rangle\langle E_2|\right) - \frac{\gamma_S - \gamma}{2}\left(|E_1\rangle\langle E_2| + |E_2\rangle\langle E_1|\right)\,, \tag{4.23}$$

where

$$H' = -\sum_{\mu}\Delta_\mu|E_\mu\rangle\langle E_\mu| + \delta_{LS}\sum_{\mu,\nu}(\hat{d}^*_\mu\cdot\mathbb{1}_\perp\cdot\hat{d}_\nu)c_\mu c_\nu|g|^2\sqrt{N_\mu N_\nu}|E_\mu\rangle\langle E_\nu|\,. \tag{4.24}$$

The eigenvalues of the operator S_{system} are

$$\lambda_g = 0\,,$$

$$\lambda_\pm = -\frac{1}{2}\left(\frac{1}{2}(\gamma_S+\gamma) + i\frac{2}{3}N|g|^2|\delta_{LS} \pm \sqrt{(2\phi)^2 + \left[\frac{2}{3}N|g|^2\delta_{LS} - i\frac{1}{2}(\gamma_S-\gamma)\right]^2}\right)\,. \tag{4.25}$$

Here λ_g is the eigenvalue of the ground state and $\lambda_\pm$ are the eigenvalues of the excited states. Upon the substitution of C in Eq. (4.22) and $\Gamma = \gamma_S/2\,,\ \gamma_0 = \gamma/2$ in Eq. (4.25) and we obtain

$$\lambda_\pm = \frac{\Gamma + \gamma_0 + iC \pm \sqrt{(2\phi)^2 + \left[C - i(\Gamma - \gamma_0)\right]^2}}{2}\,. \tag{4.26}$$

We notice that the eigenvalues above are the same with the eigenvalues in Eq. (2.89). Two different theoretical models derive the same eigenvalues.

We define a full non-Hermitian operator taking into account the contribution of the incident x-ray pulse

$$S = -iH - \frac{\gamma_S}{2}\left(|E_1\rangle\langle E_1| + |E_2\rangle\langle E_2|\right) - \frac{\gamma_S - \gamma}{2}\left(|E_1\rangle\langle E_2| + |E_2\rangle\langle E_1|\right) , \quad (4.27)$$

where $H = H_0 + H_\Omega + H_{LS}$ is the Hamiltonian of the whole system. H_0, H_Ω and H_{LS} are defined in Eq. (4.10). Then the time evolution of the system is governed by the non-Hermitian operator S. The master equation (4.4) can be written in another form

$$\frac{d}{dt}\rho = S\rho - \rho S\,. \quad (4.28)$$

Comparing the system in this Section with the one in Sec. 2.2, the x-ray pulse can be considered to bump the system to the excited state (4.3). Then the timed Dick state has been prepared and this is the initial condition in Sec. 2.2. The emission of the excited state follows the way described in Sec. 2.2. In the following we show that the effects discussed in Sec. 2.2 maybe observed in the thin-film cavity system with experimental parameters available already today.

4.3.3 Numerical results

4.3.3.1 Introduction to CONUSS software package

We benchmark our numerical results with CONUSS. CONUSS stands for coherent nuclear resonant scattering by single crystals and it is a software for the interpretation of time or energy spectra from coherent elastic nuclear resonant scattering, for instance, forward scattering, Bragg/Laue scattering and grazing incidence scattering [102]. This program was created for the nuclear resonant scattering of SR in 1988 by W. Sturhahn and E. Gerdau. It has been continuously improved with the experimental studies of coherent nuclear resonant scattering. Forward scattering was added in 1992 and a graphical display was included in 2009. Grazing incidence scattering geometry and simplified input files for improved user experience were added in 2015. CONUSS is written in Fortran90 and has been implemented on several UNIX-like operating systems: Sun's Solaris, Apple's Mac OS X, Redhat-Enterprise Linux, and Fedora Linux. It has been used for the parameterization of experimental data in numerous publications [103–110]. In grazing incidence scattering, theoretical predictions by CONUSS have proven to agree extremely well with experimental results [11, 20, 22, 23, 111].

4.3.3.2 Numerical results

The structure of the cavity is shown in Table 4.1. In the thin-film cavity system, the collective Lamb shift is proportional to the ratio $\Delta_C/(\kappa^2 + \Delta_C^2)$. For small angular deviations from the resonance angle φ_0, the cavity detuning depends on the x-ray photon incidence angle φ as $\Delta_C = -\omega\varphi_0\Delta\varphi$, with ω the incident radiation frequency and $\Delta\varphi = \varphi - \varphi_0$ [33]. Thus, if the incidence angle is exactly on

resonance, then the collective Lamb shift equals zero, $C = 0$. The superradiance decay rate changes with the ratio $\kappa/(\kappa^2 + \Delta_C^2)$. We can modulate the values of the collective Lamb shift and superradiance decay rate by changing the incidence angle.

Table 4.1: Parameters of the cavity structure.

Material	Thickness (nm)
Pd	5
C	20
^{57}Fe	1
C	20
Pt	30

When the probe pulse is incident at the resonant angle, the collective Lamb shift C is zero. We consider two cases. The first case is that the single-nucleus magnetic hyperfine splitting 2ϕ is significant. This means the energy difference between the two transitions is much larger than the superradiance decay rate which can be shown as follows

$$2\phi \gg (\Gamma - \gamma_0)\,. \tag{4.29}$$

Then the spectrum in the reflection direction (see Fig. 4.3) can be considered as the summation of two Lorentzians. This corresponds to the case in Sec. 2.2.2.1. The second case is that the superradiance is significant as discussed in Sec. 2.2.2.1. We use the same cavity structure but apply a smaller hyperfine magnetic field. In this case, the reflection spectrum is no longer the summation of two Lorentzians. As shown in Fig. 4.4, an EIT-like spectrum is obtained.

In the off-resonant case, the collective Lamb shift decreases by $1/\Delta_C$ and the superradiance decay rate decreases by $1/\Delta_C^2$. Therefore the collective Lamb shift can be much larger than the superradiance decay rate. Applying an appropriate magnetic field, the effect in Sec. 2.2.2.2 can be observed. The magnetic field B we use here is 6.4 T and the hyperfine splitting $\phi = 6\gamma$. As a result, two dips appear in Fig. 4.5. In order to understand this, we rewrite the reflection coefficient as follows

$$R = R_C + R_N\,, \tag{4.30}$$

where

$$R_C = \frac{2\kappa_R}{\kappa + i\Delta_C} - 1\,, \tag{4.31}$$

and

$$R_N = -\frac{i}{a_{in}} \frac{\sqrt{2\kappa_R}}{\kappa + i\Delta_C} \frac{\frac{2}{3}N|g|^2\Omega}{\Delta - \frac{2}{3}N|g|^2\delta_{LS} + i\left(\frac{\gamma}{2} + \frac{2}{3}N|g|^2\zeta_S\right)}\,. \tag{4.32}$$

R_C represents the cavity contribution to the reflection coefficient and R_N is the resonant nuclear reflection. We find that the reflection spectrum is composed of the interference between a continuum cavity channel and a bound state contribution.

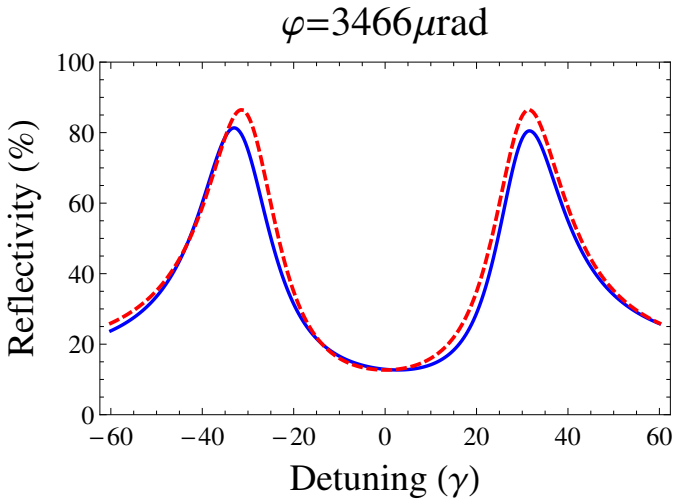

Figure 4.3: Reflectivity spectra calculated with CONUSS (solid blue line) and the quantum cavity model (dashed red line) for an incidence angle $\varphi = 3466\,\mu$rad. The hyperfine magnetic field is B=33.3 T.

This leads to Fano interference [111, 112]. The two dips in Fig. 4.5 represent the resonant positions of the two transitions. The gap between the two dips is around 14.6γ. However, the energy gap between the two transitions in the single-nucleus splitting is 12γ. This means not only the energy levels are shifted by the collective Lamb shift but also the gap between the energy levels is enhanced in the collective magnetic hyperfine splitting. This effect has also been presented in Sec. 2.2.2.2. Further parameter values used in the quantum model are

$$\kappa_R = 3.1 \cdot 10^5\gamma,\ \kappa = 4.6 \cdot 10^5\gamma,\ \sqrt{N}|g| = 2500\gamma\,.$$

All the parameters we have used in this section are available in the experiment today. Thus, the collective magnetic hyperfine-splitting effects in single photon superradiance which is presented in Sec. 2.2 could be demonstrated in a thin-film x-ray cavity embedded a ^{57}Fe nuclei layer.

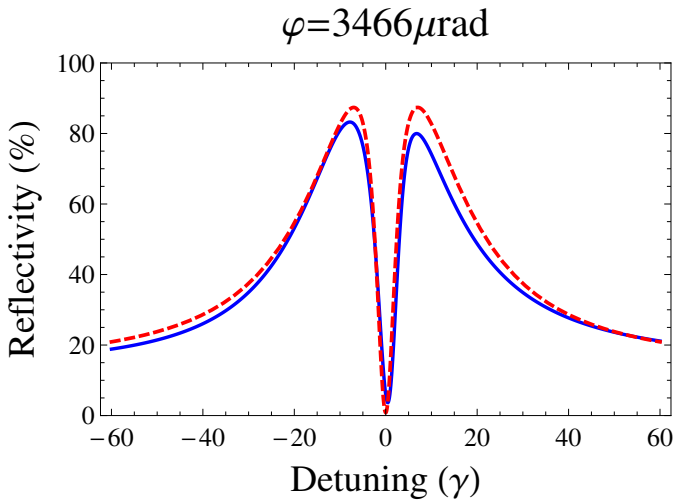

Figure 4.4: Reflectivity spectra calculated with CONUSS (solid blue line) and the quantum cavity model (dashed red line) for an incidence angle $\varphi = 3466\,\mu$rad. The hyperfine magnetic field is B=6.4 T.

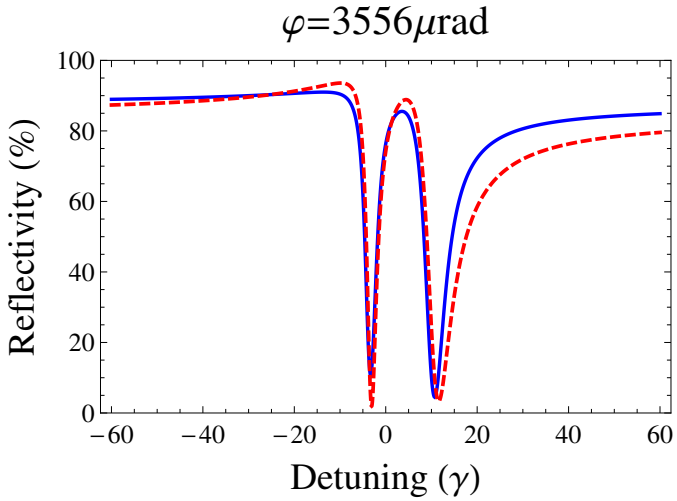

Figure 4.5: Reflectivity spectra calculated with CONUSS (solid blue line) and the quantum cavity model (dashed red line) for an incidence angle $\varphi = 3556\,\mu$rad. The hyperfine magnetic field is B=6.4 T.

Chapter 5

Stopping narrow-band x-ray pulses in nuclear media

In this Chapter, we present more details about the EIT-like spectrum in Fig. 4.4 obtained in the thin-film cavity with embedded layers containing nuclei with a transition resonant to the x-ray pulse. Based on this effect, we demonstrate from the theory side that a spectrally narrow x-ray pulse can be mapped and stored as nuclear coherence in a thin-film planar x-ray cavity. The storage mechanism relies on the formation of a dark-state polariton [113] rather than the absorption of x-rays in the nuclear medium, as a consequence of destructive interference of two possible resonant transitions between the hyperfine-split nuclear ground and excited states. Coherent control over the matter and radiation parts of the polariton is provided by manipulation of the magnetic field. We lay out the theoretical formalism for describing this system and show that despite the very different level scheme, the dynamics of the x-ray cavity with an embedded nuclear layer in the presence of a hyperfine magnetic field is governed by equations reminding of EIT in atomic media [35]. Our results prove that a spectrally narrow x-ray pulse can be completely mapped onto nuclear coherences and retrieved at later times, with storage time determined by the nuclear excited state mean lifetime, on the order of hundred ns. Our scheme is based on a different operation principle than previously implemented or proposed storage setups [114, 115], with the two major advantages that (i) it is more reliable and much easier to implement experimentally and (ii) it works for a broader spectrum of parameters, e.g., storage times or variable pulse width. We anticipate this setup can become a versatile tool for control of spectrally narrow x-ray pulses.

5.1 Motivation of controlling hard x-rays

Recent years have witnessed the commissioning of coherent x-ray sources opening the new field of x-ray quantum optics [12]. While not yet as advanced as its optical counterpart, the latter may enable coherent control of x-rays, with potential applications for the fields of metrology, material science, quantum information, biology and chemistry. The desirable properties of x-rays are deeper penetration, better focus, no longer limited by an inconvenient diffraction limit as for optical photons, correspondingly spatial resolution, robustness, and the large momentum transfer they may produce. A peculiar circumstance is that x-rays are resonant to either inner shell electron transitions in (highly) charged ions [116–118], or

transitions in atomic nuclei [20, 71]. First experiments towards the demonstration of nonlinear phenomena with x-rays have been performed with atoms [119–122] and nuclei [11, 20, 22, 23, 111, 123, 124]. Nonlinear interactions between x-rays and nuclei are a promising candidate to control x-ray pulses, which remains challenging so far [20, 23, 111, 114].

Photonic qubits are essential for the development of many devices in quantum information technology. Until now, we can only control optical and infrared photons to be employed as flying qubits. High-performance control over x-rays is compulsory if also x-ray qubit applications in quantum information or cryptography are to be realized [124, 125], such as, for instance, preparation of entangled ensembles [126], generation of squeezed states [127], quantum memories [128, 129] or photonic circuits [130–133], already accomplished in the long-wavelength regime. Main difficulties compared to the optical regime are the lack of high quality factor cavities and of suitable level schemes that would facilitate established control schemes.

5.2 EIT-like spectrum

EIT is a quantum interference effect that can be used to render a resonant opaque medium transparent. Typically, EIT can be achieved in a so-called Λ three-level system driven simultaneously by a strong control and a weaker probe pulse. Due to the control field, the medium becomes transparent for the probe pulse in a narrow window around the resonance frequency [35]. In the optical regime, EIT can be used to slow down [134–136] and even to stop light in an atomic medium [36–40] by a sudden turning off of the control field. However, due to the lack of two-color x-ray sources [41, 42] and the proper nuclear three-level systems, the traditional optical EIT scenario is not available at present for x-rays. So far, an alternative setup with two nuclear layers in a thin-film planar x-ray cavity has reported EIT-like behavior with nuclear transitions [20]. In addition, in a recent work [23] slow light was observed in the hard x-ray regime by introducing a steep linear dispersion in the nuclear optical response.

In Sec. 4.2, we introduce the theoretical formalism used to investigate the system which is shown in Fig. 4.2. The dynamics of the system is described by the master equation [69] in Eq. (4.9) which has proved to be very successful in modeling the interaction of SR with nuclei in bulk samples or thin-film cavities [33, 89, 137]. The observable in the system is the reflectivity which is obtained in the bad-cavity limit, i.e., the decay rate of the cavity κ is much larger than the atom-field cavity coupling strength g. In resonant case, the cavity contribution to the reflection coefficient in Eq. (4.17) is very small and the reflection coefficient is mainly determined by the resonant nuclei. In order to understand the EIT-like effect, we neglect the small cavity contribution to the reflection coefficient and we obtain

$$R \approx R_N = -\frac{i}{a_{in}} \frac{\sqrt{2\kappa_R}}{\kappa + i\Delta_C} \sum_\mu (\hat{a}^*_{out} \cdot \mathbb{1}_\perp \cdot \hat{d}_\mu) c_\mu \sqrt{N_\mu} g^* \langle E_\mu | \rho | G \rangle \,. \tag{5.1}$$

We find the reflection coefficient is proportional to the coherence terms $\langle E_\mu|\rho|G\rangle$.

Under the steady-state conditions [33], we have

$$\frac{d}{dt}\rho = -i[\hat{H},\rho] + \mathcal{L}[\rho] = 0\,. \tag{5.2}$$

In order to simplify the calculation, we assume the populations are in the linear response $|G\rangle\langle G| = 0$ and $|E_\mu\rangle\langle E_\mu| = 0$. Then the sum of the two relevant coherences in the system is given by

$$\rho_{23} + \rho_{13} = \frac{i\sqrt{\frac{16}{3}}g\sqrt{N}\Omega(\gamma - 2i\Delta)}{(\gamma - 2i\Delta)(\gamma' - 2i\Delta') + (2\phi)^2}\,, \tag{5.3}$$

where $\gamma' = \gamma + \frac{4}{3}|g|^2 N\zeta_S$, $\Delta' = \Delta - \frac{2}{3}|g|^2 N\delta_{LS}$ and $\phi = \frac{1}{2}(\delta_g + \delta_e)$. Here γ is the nuclear spontaneous emission rate which is connected to the nuclear mean lifetime τ_0 by $\gamma = \hbar/\tau_0$. With $\hbar = 1$, in the following γ is used as both rate and width. δ_g (δ_e) denotes the energy difference between two adjacent ground (excited) substates. Next, we consider the resonant case ($\Delta_C = 0$) in which $\delta_{LS} = 0$. Then we obtain

$$\rho_{23} + \rho_{13} = \frac{i\sqrt{\frac{16}{3}}g\sqrt{N}\Omega(\gamma - 2i\Delta)}{(\gamma - 2i\Delta)(\gamma' - 2i\Delta) + (2\phi)^2}\,. \tag{5.4}$$

Numerical results for the reflectivity of the cavity presented in Fig. 4.2 in an external hyperfine magnetic field with B =6.4 T for the resonant case ($\Delta_C = 0$, corresponding to $\varphi = \varphi_0 = 3466$ μrad) as a function of the x-ray detuning are presented in Fig. 4.4. The hyperfine magnetic field introduces the energy splitting $\phi = 6\gamma$. A dip very similar to the well-known EIT absorption spectra in the atomic case and to the x-ray EIT results presented in Ref. [20] can be observed. We note that for the resonant case, $\delta_{LS} = -\frac{\Delta_C}{\kappa^2 + \Delta_C^2} = 0$, $\Delta' = \Delta$ and with $\gamma' \gg \gamma$, the expression of the coherence sum $\rho_{21} + \rho_{31}$ in Eq. (5.4) is very similar to the EIT coherence [35], as discussed in the following Section. Here the magnetic field plays the role of the control field in the EIT case. Thus, the reflectivity of the thin-film cavity behaves analogously to the EIT absorption and the transmission is the equivalent to atomic medium transparency. The comparison in Fig. 4.4 shows that the quantum formalism used is very reliable in describing the transparency window. The numerical results in Fig.4.4 includes the cavity contribution to the reflection coefficient.

5.3 Comparison with traditional EIT in a Λ three-level system

Traditional EIT in atomic media occurs in a Λ three-level system with an upper state $|a\rangle$ and two ground states $|b\rangle$ and $|c\rangle$ (see Fig. 5.1(a)). Initially the atoms are all in the ground state $|b\rangle$ and we assume that the control field is resonant with the transition $|c\rangle \rightarrow |a\rangle$. The coherence between state $|a\rangle$ and state $|b\rangle$ is given by [69]:

$$\rho_{ab} = \frac{i\Omega_p(\Gamma_{bc} + i\delta_p)}{(\Gamma_{ab} + i\delta_p)(\Gamma_{bc} + i\delta_p) + \Omega_c^2/4}, \tag{5.5}$$

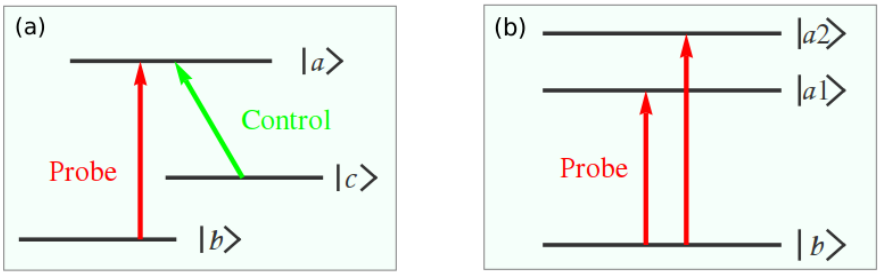

Figure 5.1: (a) A Λ three-level system driven by two laser fields. (b) An equivalent V-like three-level scheme.

where δ_p is the detuning between the resonant frequency of transition $|b\rangle \rightarrow |a\rangle$ and the probe pulse, and Γ_{ab} and Γ_{bc} are dephasing rates for the $|b\rangle \rightarrow |a\rangle$ and $|b\rangle \rightarrow |c\rangle$ transitions, respectively. Typically, a condition for EIT is that $\Gamma_{ab} \gg \Gamma_{bc}$. Moreover, Ω_p is the Rabi frequency of the probe pulse and Ω_c is the Rabi frequency of the control field. We note here that the structure of the expression above is identical to the one presented in Eq. (5.4).

The coherence as a function of the complex variable δ_p has two poles [138],

$$\delta_{\pm} = \frac{1}{2}\left(i\Gamma_{ab} + i\Gamma_{bc} \pm \sqrt{\Omega_c^2 - (\Gamma_{ab} + \Gamma_{bc})^2}\right). \tag{5.6}$$

Then the coherence ρ_{ab} can be presented as a superposition of two resonant responses associated with the transitions from the ground state to the corresponding decaying dressed states [138]:

$$\rho_{ab} = \frac{\Omega_p A_+}{\delta_p - \delta_+} + \frac{\Omega_p A_-}{\delta_p - \delta_-}, \tag{5.7}$$

where $A_{\pm}$ are defined as

$$A_{\pm} = \pm\frac{\delta_{\pm} - i\Gamma_{bc}}{\delta_+ - \delta_-}. \tag{5.8}$$

Thus, the control field splits the upper level $|a\rangle$ and the probe pulse drives both transitions between ground state $|b\rangle$ and the two split upper levels $|a_1\rangle$ and $|a_2\rangle$. An equivalent schematic diagram is presented in Fig. 5.1(b). The interference between the two transitions results in the characteristic feature of EIT in the range of the control field intensities $4\Gamma_{ab}\Gamma_{bc} \leq \Omega_c^2 < 4(\Gamma_{ab} - \Gamma_{bc})^2$ [138]. In the thin-film x-ray cavity system, the EIT-like effect occurs due to the interference between the two $\Delta m = 0$ transitions under the presence of vacuum-mediated coupling between the two upper states. The splitting of the excited states in the two systems depicted are generated by the strong control field and the magnetic field, respectively.

5.4 Stopping x-ray pulses

Now we investigate how to store an x-ray pulse exploiting the EIT-like features of the setup. The expression in Eq. (5.4) reveals that the energy difference between

the two transitions 2ϕ plays the role of control field from the traditional EIT case. In analogy with the atomic case where switching off the control field leads to pulse storage, we study the case when the hyperfine magnetic field in our cavity system disappears. First let us derive the propagation equation for the x-ray pulse in the cavity.

The evolution of the coherences is described by the Heisenberg equations

$$\frac{\partial(\rho_{31}+\rho_{32})}{\partial t} = i\sqrt{\frac{4}{3}N}g\Omega - \left(\frac{\gamma'}{2}+i\Delta\right)(\rho_{31}+\rho_{32}) - i\phi(\rho_{31}-\rho_{32})\,,$$

$$\frac{\partial(\rho_{31}-\rho_{32})}{\partial t} = -\left(\frac{\gamma}{2}+i\Delta\right)(\rho_{31}-\rho_{32}) - i\phi(\rho_{31}+\rho_{32})\,. \tag{5.9}$$

Disregarding the slow decay γ, we may derive

$$\rho_{31}+\rho_{32} = \frac{i}{\phi}\frac{\partial(\rho_{31}-\rho_{32})}{\partial t}\,,$$

$$\rho_{31}-\rho_{32} = \frac{\sqrt{\frac{4}{3}N}g\Omega}{\phi} + \frac{i}{\phi}\left(\frac{\gamma'}{2}+\frac{\partial}{\partial t}\right)\left[\frac{i}{\phi}\frac{\partial(\rho_{31}-\rho_{32})}{\partial t}\right]. \tag{5.10}$$

The change of the hyperfine magnetic field leads to a time-dependent function $\phi(t)$. We assume a sufficiently slow change of $\phi(t)$ and simplify the equations using adiabatic conditions. In this limit, we obtain

$$\rho_{31}(z,t)-\rho_{32}(z,t) = \frac{\sqrt{\frac{4}{3}N}g\Omega(z,t)}{\phi(t)}\,. \tag{5.11}$$

Finally we arrive at the propagation equation of the x-ray pulse in the perturbative and the adiabatic limit

$$\left(\frac{\partial}{\partial t}+c\frac{\partial}{\partial z}\right)\Omega(z,t) = -\frac{2g^2N}{3\phi(t)}\frac{\partial}{\partial t}\frac{\Omega(z,t)}{\phi(t)}\,. \tag{5.12}$$

The group velocity of the x-ray pulse is smaller than the light velocity in vacuum c according to $v_g = c/(1+\frac{2g^2N}{3\phi^2})$. Such subluminal x-ray propagation in thin-film cavities has been confirmed experimentally in Ref. [23]. We may introduce here the dark-state polariton originally studied in the atomic case [113]

$$\Psi(z,t) = \cos\theta(t)\Omega(z,t) - \sin\theta(t)\sqrt{\frac{2N}{3}}\left[\rho_{31}(z,t)-\rho_{32}(z,t)\right]\,, \tag{5.13}$$

with $\cos\theta(t) = \frac{\phi(t)}{\sqrt{\phi^2(t)+\frac{2}{3}g^2N}}$ and $\sin\theta(t) = \frac{g\sqrt{\frac{2}{3}N}}{\sqrt{\phi^2(t)+\frac{2}{3}g^2N}}$. The polariton dynamics is governed by the expression

$$\left[\frac{\partial}{\partial t}+c\cos^2\theta(t)\frac{\partial}{\partial z}\right]\Psi(z,t) = 0\,, \tag{5.14}$$

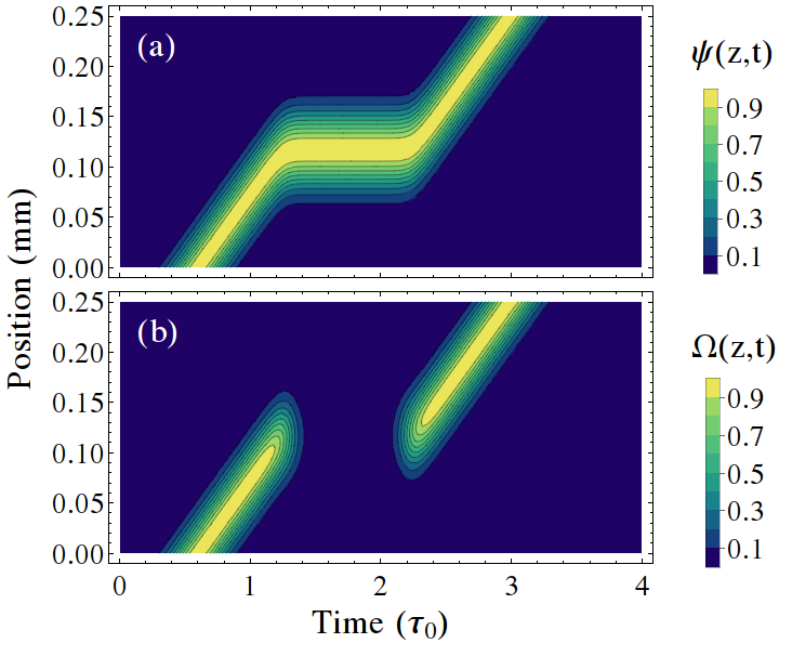

Figure 5.2: Propagation dynamics of the polariton field Ψ (a) and the Rabi frequency Ω of the pulse (b). The magnetic field is switched off at $t = 1.3\tau_0$ and switched back on at $t = 2.2\tau_0$.

which describes a shape-preserving propagation with velocity $v = v_g = c\cos^2\theta(t)$ [113],

$$\Psi(z,t) = \Psi\left(z - c\int_0^t \cos^2\theta(\tau)d\tau, t = 0\right) . \tag{5.15}$$

The expression above defines a shape-preserving, polariton-like mixture of electromagnetic field and collective nuclear coherences. If the hyperfine magnetic field is switched off while the x-ray pulse is inside the medium, the propagation velocity of the polariton $v = c\frac{\phi^2(t)}{\phi^2(t)+\frac{2}{3}g^2N}$ reduces to zero. By switching on the magnetic field after some time, the polariton will resume propagation through the sample at the original velocity. The x-ray pulse has been transferred to the nuclear coherences and then back by the external operation on the hyperfine energy splitting in the system.

Numerical results obtained from the evaluation of Eqs. (5.12)-(5.14) are presented in Figs. 5.2. As incoming pulse we choose for illustration purposes a Gaussian-shape pulse $\Omega_p(t,0) = \Omega_{p0}\exp[-(\frac{t}{t_0})^2]$ with a $t_0 = 0.2\tau_0$, i.e., a bandwidth of 2γ. The pulse enters the medium and undergoes spatial compression as the velocity is diminishing from c to v_g via EIT. In order to store the x-ray pulse, we switch off the magnetic field at $t = 1.3\tau_0$ after the entire pulse has entered the medium. As a result, the velocity of the quantum field Ψ reduces to zero and the x-ray pulse is mapped onto the collective nuclear coherences. The process can be reversed by switching back on the hyperfine magnetic field, for instance at $t = 2.2\tau_0$. The polariton then resumes its propagation through the medium at the same velocity as before, as shown in Fig. 5.2(a). The evolution of the photon field part of the polariton is depicted in Fig. 5.2(b) and shows that during the storage,

the pulse is completely mapped onto the nuclear coherences. Note that the storage time is limited by the incoherent nuclear decay rate γ (corresponding to $\tau_0 = 141$ ns) that characterizes the nuclear coherences, leading to an exponential drop of the pulse intensity, for illustration purposes not included in Figs. 5.2.

In practice, spectrally narrow pulses can be produced by a single-line resonant spectral analyzer and mechanical or polarization-based removal of the non-resonant component [23]. Alternatively, a SR Mössbauer source based on a narrow-band, pure nuclear reflection off a $^{57}FeBO_3$ crystal [139–143] could be employed. This source provides ^{57}Fe resonant radiation at 14.4 keV within a bandwidth of 15 neV which is tunable in energy over a range of about ± 0.6 μeV [141]. The temporal profile of the SR Mössbauer pulse is given by the nuclear scattering in $^{57}FeBO_3$ and presents a modulation determined by the Bessel function of the first kind, $\left(\frac{\xi}{\sqrt{\xi\gamma t}} J_1\left[2\sqrt{\xi\gamma t}\right]\right)^2 e^{-\gamma t}$, with ξ the optical depth of the sample as discussed in Chapter 3. Our numerical results show that the exact initial shape of the pulse does not introduce dispersion in the EIT-based storage. In addition, similarly to the atomic case [144, 145], we expect the adiabaticity condition to be relaxed and not restrict the storage experimentally.

Finally, our theoretical simulation considers a switching time of approx. 50 ns for the hyperfine magnetic field. The most promising solution involves a material with no intrinsic nuclear Zeeman splitting like stainless steel $Fe_{55}Cr_{25}Ni_{20}$ [146, 147]. The challenge is to turn off and on the external magnetic fields of few Tesla on the ns time scale. This could be achieved by using small single- or few-turn coils and a moderate pulse current of approximately 15 kA from low-inductive high-voltage "snapper" capacitors [99]. Another mechanical solution, e.g., the lighthouse setup [100] could be used to move the excited target out of and into a region with confined static B field. The details have been presented in Sec. 3.4.

A comparison with other x-ray setups highlights the advantages of our scheme. In the thin-film x-ray cavities experiment in Ref. [20], the EIT-like dip in the reflectivity is created by the presence of a second ^{57}Fe layer in the thin-film cavity. Due to the fixed cavity layer geometry, this setup has no tunable parameters and cannot be used to stop the x-ray pulse in the medium. In Ref. [23], where subluminal x-ray propagation in thin-film cavities was accomplished, the EIT transparency regime was avoided and the hyperfine magnetic field kept constant. Coherent x-ray storage has been pioneeringly demonstrated in a NFS setup [114] almost two decades ago. That scheme works in the absorption regime: the x-ray photon excites a nucleus whose decay is suppressed by a rotation of the hyperfine magnetic field. A similar concept using the complete removal of the hyperfine magnetic field has been proposed in Ref. [115]. Both setups rely on the storage of the x-ray field in a nuclear excited state and the manipulation of the magnetic field at predetermined, fixed times t_s which guarantee destructive interference and suppression of the nuclear decay. However, the latter may still occur prior to $t = t_s$ such that storage is neither deterministic nor really efficient. For example, while waiting for the earliest switching time in Ref. [115], the nuclear excited state has already decayed with 70% probability.

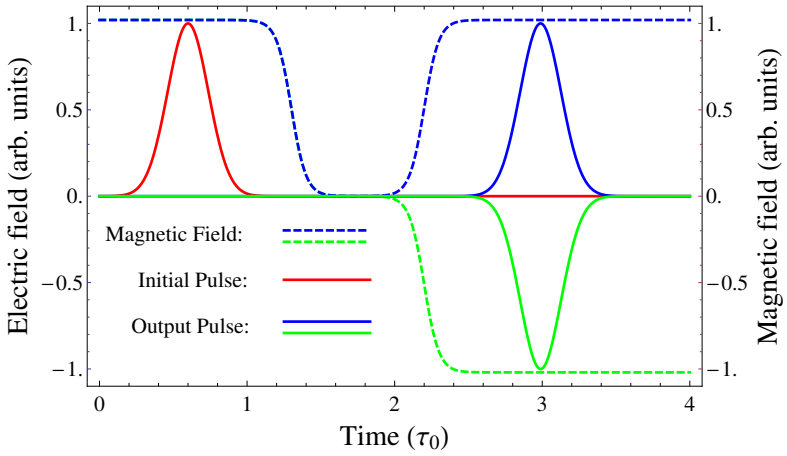

Figure 5.3: The envelope of the electric field of the probe pulse. The two dashed lines denote the different operations of the magnetic field respectively. The red solid line is the electric field of the initial pulse. The blue solid line stands for the electric field of the output pulse in the case that the magnetic field is switched off at $t = 1.3\tau_0$ and turned back on at $t = 2.2\tau_0$ in the same direction. The green solid line is the electric field of the output pulse when we turn off the magnetic field at $t = 1.3\tau_0$ and turn it on again in the opposite direction at $t = 2.2\tau_0$.

5.5 π phase modulation of x-ray pulses

As in the case of atomic EIT, the transparency-based x-ray storage has a number of tunable features. The velocity of the pulse can be controlled by the magnitude of the hyperfine magnetic field B. The orientation of B can decide upon the phase of the x-ray pulse. Next we will present how to modulate the phase of the x-ray pulse with a shift of π . A rotation of the releasing magnetic field compared to the initial direction can lead to a phase modulation of the signal. The most relevant example is a releasing magnetic field orientated antiparallel to the initial one. In Fig. 5.3, we present two operations of the magnetic field. The first is that we turn off the magnetic field at $t = 1.3\tau_0$ and turn on the magnetic field again in the same direction at $t = 2.2\tau_0$ (the blue dashed line). The pulse has been stored for some time and the output pulse is shown in Fig. 5.3 (the blue solid line). The second operation is that we switch off the magnetic field at $t = 1.3\tau_0$ and switch back in the opposite direction at $t = 2.2\tau_0$ (the green dashed line). This is equivalent to a transformation $\cos\theta(t) \to -\cos\theta(t)$. Since the polariton in Eq. (5.13) is shape-preserving, the corresponding equivalent transformation of the electric field leads to $\Omega(z,t) \to -\Omega(z,t)$, which yields a phase modulation of π. This is a π phase shift of the electric field which is presented in Fig. 5.3 (the green solid line). Finally we modulate a π phase shift by comparing the green solid line and green solid line in Fig. 5.3.

We conclude that our storage setup in the transparency window reminiscent of EIT is more flexible and more reliable than existing or proposed storage methods for x-rays. It relies on a different physical mechanism—the mapping of the x-ray pulse onto nuclear coherences, it is deterministic, and can be performed at variable

times. We anticipate that bringing x-ray pulses to a halt will establish concepts used in atomic physics for nuclear physics with x-rays and render possible new applications towards quantum information processing in the x-ray regime.

Chapter 6

Collective strong coupling of x-rays in nuclear media

So far the physics discussed in this thesis was referring to the weak coupling regime. In this Chapter, we focus on the collective strong coupling of single x-ray photons. First we present a theoretical protocol to realize collective strong coupling for x-rays in a coupled x-ray cavities system. We couple the thin-film cavity with embedded ^{57}Fe to an x-ray Fabry-Pérot cavity. The x-ray pulses probes the thin-film cavity at grazing angles and the resonant frequency of the thin-film cavity can be modulated by changing the incidence angles. We show that collective strong coupling in the x-ray regime can be reached in the off-resonant case. Rabi oscillation of x-ray photons is predicted in this case. Following this line, we study a thin-film cavity with two embedded ^{57}Fe nuclear layers. We show that collective strong coupling between the two nuclear layers can be reached when the cavity is off-resonant. Pseudo-Rabi splitting between the two ^{57}Fe nuclear layers occurs which is reminiscent of the Rabi oscillation in strong coupling regime as known from cavity QED. We also figure out the transition from the electromagnetically induced transparency regime to the pseudo-Rabi splitting with x-ray photons.

6.1 Introduction and motivation

Cavity quantum electrodynamics [148–150] has allowed us to reach ultimate control over single atoms or photons and provides an effective construction for quantum networks and fundamental tests of quantum mechanics. Ground-breaking experimental methods with optical and microwave cavities have enabled measuring and manipulation of individual quantum systems, for instance, quantum entanglement between atoms and photons [43], quantum phase transitions [44, 45] and quantum logic gates [46, 47]. Photon blockade and vacuum Rabi resonance in an optical cavity with one trapped atom have also been observed [48, 49]. All these achievements are based on the strong coupling between the atoms and cavity. The desire to extend this success also at higher frequencies was so far hindered by the lack of good cavities in the x-ray regime. High-performance x-ray cavities which have both high quality (Q) factor and small mode volume (V) are so far not available. A Fabry-Pérot cavity for x-rays [151, 152] could be built in a crystal cavity with the high reflectivity x-ray mirrors [153]. Even so, the x-ray mirror reflectivity based on dynamical diffraction is several orders of magnitude lower than for optical photons, reaching up to 0.99 [153]. On the other hand, many pioneering nu-

clear quantum optics experiments have been performed in highly dissipative thin film x-ray cavities, observing for the first time the cooperative Lamb shift [11], electromagnetically induced transparency (EIT) with x-rays [20], spontaneously generated coherence [22] or x-ray slow light [23].

In the previous Chapters, we have discussed about the collective atom-field interaction in the weak coupling regime. On the other side, collective strong coupling of optical photons has been recently investigated in the literature. Examples are the collective strong coupling with ion Coulomb crystals in an optical cavity [50], the observation of coherent many-body Rabi oscillations [51] and the observation of collective excitation of two individual atoms [52]. The collective atom-field coupling in enhanced by a factor $\sim \sqrt{N}$ when compared to a single atom. Even so, it is still very hard to realize strong coupling in the x-ray regime. In Ref. [154], it was shown that coherent polariton dynamics is expected to improve the performance of a dissipative cavity when the latter is coupled to a high-Q but large-V auxiliary cavity via a strong dark state interaction. The auxiliary cavity acts in this case as a storage and delay for the resonant photons which are otherwise rapidly lost from the dissipative cavity. The strong coupling and Rabi oscillations have been predicted theoretically for this case. Here, we investigate a new idea to couple an x-ray Fabry-Pérot cavity with thin-film cavity in Sec. 6.2. In addition, we envisage another alternative to store an x-ray photon within the dissipative cavity by employing a thin film cavity with two layers of resonant ^{57}Fe nuclei in Sec. 6.3. We show that pseudo-Rabi splitting between the two ^{57}Fe layers may occur.

6.2 Collective strong coupling of x-rays in coupled cavites

6.2.1 Introduction of the x-ray Fabry-Pérot cavity

The concept of the x-ray Fabry-Pérot cavity was proposed by Steyerl and Steinhauser in 1979 [155]. The Fabry-Pérot cavity mainly consists of two highly reflecting parallel mirrors. When the gap between the two mirrors is an integer multiple of half of the photon wavelength, constructive interference occurs and the standing wave forms in the cavity. This makes the system transparent. For the Fabry-Pérot cavity for x-rays, the essence is the replacement of the optical mirrors by Bragg back-reflection from parallel crystals [151, 155]. Due to the multiple back-and-forth reflections in the crystal cavity, the x-ray photon can be stored for some time. In 2000, x-ray photon (energy 15.817 keV) were stored experimentally within the x-ray Fabry-Pérot cavity formed by two plates of crystalline silicon [156]. Some signals were still observed after 14 nanoseconds. However, due to the low reflectivity of silicon crystals, the intensity of the reflected beams in this experiment was not high enough for practical applications. The effective storage time was much smaller that one nanosecond. In 2003, with a higher reflectivity of the crystal mirrors, the storage time for 14.315 keV x-ray photons in a Fabry-Pérot cavity was improved to 0.86 nanoseconds [151]. In this case, the reflectivity of the crystal cavity was only 0.85. In 2011, a reflectivity of hard x-rays from diamond

crystals with values better than 99% was achieved [153]. The next problem is how to use this high-reflectivity crystal mirror to build the Fabry-Pérot cavity. If we solve this problem, we could store the x-ray photons for a much longer time.

6.2.2 Theoretical approach

The strong coupling regime of cavity quantum electrodynamics has been reached for atoms in optical and microwave cavities and it brings light-matter interaction to the single-photon level. However, an excellent cavity with both high quality (Q) factor and small mode volume (V) for x-rays does not exist. Recently strong coupling and Rabi oscillations have been presented theoretically in a highly dissipative cavity QED system [154]. Here, we investigate the collective strong coupling in x-ray regime on the level of single x-ray photons in a system of Fabry-Pérot cavity and thin-film coupled cavities (see Fig. 6.1). We show that vacuum Rabi splitting in x-ray regime can be observed due to the strong coupling.

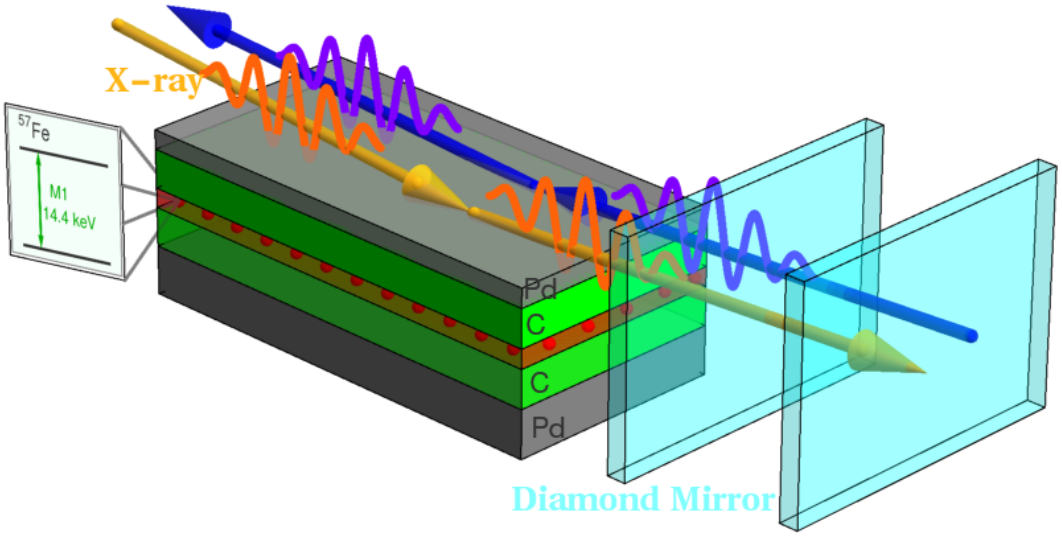

Figure 6.1: Schematic of the thin-film cavity with embedded ^{57}Fe coupled to an x-ray Fabry-Pérot cavity composed of two diamond mirrors. The x-ray pulse probes the thin-film cavity at the grazing incidence. The reflected x-ray beam shines the x-ray Fabry-Pérot cavity at normal incidence. After some time, the x-ray beam probes the thin-film cavity again.

As shown is Fig. 6.1, we consider a cavity QED system consisting of a thin-film x-ray cavity with an embedded ^{57}Fe nuclear ensemble coupled to an x-ray Fabry-Pérot cavity. The x-ray pulse probes the thin-film cavity at the grazing angle and then comes almost perpendicularly to the x-ray Fabry-Pérot cavity. In the rotating wave approximation, the Hamiltonian of the system reads

$$H = \Delta_{c1} a_1^+ a_1 + \Delta_{c1} a_2^+ a_2 + \Delta_{c2} b^+ b + \sqrt{N} g \sum_{j=1}^{2} [(\hat{d}^* \cdot \hat{a}_j)\sigma_+ \, a_j + (\hat{a}_j^* \cdot \hat{d}) a_j^+ \, \sigma_-]$$

$$+ J \sum_{j=1}^{2} [(\hat{D}^* \cdot \hat{a}_j) b^+ \, a_j + (\hat{a}_j^* \cdot \hat{D}) a_j^+ \, b] \, . \tag{6.1}$$

$\Delta_{c1(2)}$ is the detuning between the thin-film (Fabry-Pérot) cavity and the bare transition energy of the nuclei, $a\,[a^+]$ is the photon annihilation (creation) operator in the thin cavity and a_1, a_2 represent different modes. Moreover, $b\,(b^+)$ is the photon annihilation (creation) operator in the x-ray Fabry-Pérot cavity. We introduce the notations $\sigma_+ = |E\rangle\langle G|$ and $\sigma_- = |G\rangle\langle E|$ with $|E\rangle\,(|G\rangle)$ being the collective excited (ground) state of the nuclei ensemble. g is coupling strength between the modes in the thin cavity and the nuclei and J describes the inter-cavity coupling strength between the modes $a_j (j = 1, 2)$ and the mode b . The normalized dipole moment $\hat{d}$ of the transition is defined with respect to the axis of the nuclear ensemble and so does the normalized vector $\hat{D}$. The dynamics of the system is described by the master equation

$$\begin{aligned}\frac{d}{dt}\rho =& - i[H, \rho] - \kappa_1 L[\rho, a_1^+, a_1] - \kappa_1 L[\rho, a_2^+, a_2] - \kappa_2 L[\rho, b^+, b] \\ & - \frac{\gamma}{2} L[\rho, |E\rangle\langle G|, |G\rangle\langle E|\,]\,, \end{aligned} \tag{6.2}$$

where $L[\rho, O^+, O^-]$ is the Lindblad operator defined in Eq. (4.11); κ_1, κ_2 and γ represent the decay rates of the thin-film cavity, the x-ray Fabry-Pérot cavity and the ^{57}Fe nuclei, respectively. The Heisenberg equation of motion for the operator a_j reads

$$\frac{d}{dt} a_j = i[H, a_j] - \kappa_1 a_j\,. \tag{6.3}$$

As we mentioned in Sec. 4.2, the thin cavity has a low quality factor Q, which means the decay constant κ_1 is very large. As κ_1 is much larger than the coupling strength $\sqrt{N}g$ and J, the dynamics of the modes a_1 and a_2 is mainly governed by fast dissipation [33]. We then approximate

$$\frac{d}{dt} a_j = 0\,, \tag{6.4}$$

which leads to

$$a_j = -\frac{i\sqrt{N}g}{\kappa_1 + i\Delta_{c1}}\sigma_- - \frac{iJ}{\kappa_1 + i\Delta_{c1}} b\,. \tag{6.5}$$

Substituting Eq. (6.5) into Eq. (6.1) we rewrite the Hamiltonian as follows

$$H_{\text{eff}} = H_0 + H_{LS}\,, \tag{6.6}$$

where

$$\begin{aligned} H_0 =& (\Delta_{c2} + \delta_{LS} J^2) b^+ b + \delta_{LS} N g^2 \sigma_+ \sigma_-\,, \\ H_{LS} =& \delta_{LS} J \sqrt{N} g (b^+ \sigma_- + \sigma_- b)\,. \end{aligned} \tag{6.7}$$

The parameter in Eq. (6.7) is defined as

$$\delta_{LS} = -\frac{\Delta_{c1}}{\kappa_1^2 + \Delta_{c1}^2}\,. \tag{6.8}$$

Then the effective system Hamiltonian reads

$$H_{\text{eff}} = \Delta_{2,\text{eff}} b^+ b + \Delta_{e,\text{eff}} \sigma_+ \sigma_- + g_{\text{eff}} (b^+ \sigma_- + \sigma_- b) \,. \tag{6.9}$$

where

$$\begin{aligned} g_{\text{eff}} &= \delta_{LS} J \sqrt{N} g \,, \\ \Delta_{2,\text{eff}} &= \Delta_{c2} + \delta_{LS} J^2 \,, \\ \Delta_{e,\text{eff}} &= \delta_{LS} N g^2 \,. \end{aligned} \tag{6.10}$$

Taking a closer look at the Hamiltonian in Eq. (6.9), we find that the form of the Hamiltonian is equivalent to the nuclear ensemble interacting with a new cavity. The effective coupling strength is g_{eff} and the effective detuning equals to $\Delta_{2,\text{eff}} - \Delta_{e,\text{eff}}$. The other parameters of the new system are defined in the following as

$$\begin{aligned} \kappa_{\text{eff}} &= \kappa_2 + \frac{J^2}{\kappa_1^2 + \Delta_{c1}^2} \kappa_1 \,, \\ \gamma_{\text{eff}} &= \gamma + \frac{N g^2}{\kappa_1^2 + \Delta_{c1}^2} \kappa_1 \,. \end{aligned} \tag{6.11}$$

Here κ_{eff} stands for the decay rate of the equivalent new cavity and γ_{eff} represents the collective decay rate of the nuclear ensemble. In the off-resonant case $\Delta_{c1} \gg \kappa_1$, we approximate

$$\frac{1}{\kappa_1^2 + \Delta_{c1}^2} \approx \frac{1}{\Delta_{c1}^2} \,. \tag{6.12}$$

Using this approximation, the effective coupling strength, detuning, decay rates of the cavity field and the nuclear layer, respectively are described by

$$\begin{aligned} g_{\text{eff}} = \beta g \,, \quad \Delta_{\text{eff}} = \Delta_{c2} + (\alpha^2 - \beta^2) \Delta_{c1} \,, \\ \kappa_{\text{eff}} = \kappa_2 + \beta^2 \kappa_1 \,, \quad \gamma_{\text{eff}} = \gamma + \alpha^2 \kappa_1 \,, \end{aligned} \tag{6.13}$$

where the scaled interaction parameters α and β are given by

$$\alpha = \frac{\sqrt{N} g}{|\Delta_{c1}|} \,, \quad \beta = \frac{J}{|\Delta_{c1}|} \,. \tag{6.14}$$

In Eq. (6.13), we notice that the effective coupling strength g_{eff} depends linearly on β while the effective decay rates κ_{eff} and γ_{eff} are quadratic functions of β and α, respectively. Therefore, if $\alpha \ll 1$ and $\beta \ll 1$, the effective coupling strength can be larger than the decay rates, driving the effective interaction into the strong coupling regime. In order to reach the strong coupling, the condition $g_{\text{eff}} > \kappa_{\text{eff}}$ should be satisfied. If $g_{\text{eff}} > \kappa_{\text{eff}}$, then we derive the range for the thin-film cavity detuning

$$\begin{aligned} |\Delta_{c1}| &> \frac{J\sqrt{N} g - \sqrt{N g^2 J^2 - 16 J^2 \kappa_1 \kappa_2 - 16 \kappa_1^2 \kappa_2^2}}{4 \kappa_2} \,, \\ |\Delta_{c1}| &< \frac{J\sqrt{N} g + \sqrt{N g^2 J^2 - 16 J^2 \kappa_1 \kappa_2 - 16 \kappa_1^2 \kappa_2^2}}{4 \kappa_2} \,. \end{aligned} \tag{6.15}$$

If the detuning $|\Delta_{c1}|$ is modified in this range, the effective strong coupling regime can be reached with x-rays.

6.2.3 Numerical results

Vacuum Rabi oscillation is an important signature of strong coupling. In cavity QED, the observation of the vacuum splitting can be used to investigate the nature of matter-light interaction at a quantum-mechanical level. Here we use the coupled cavities system to observe this effect in x-ray regime. We suppose that there is only one x-ray photon in the system. Assume that the coupling strength $g = J$ and the x-ray pulse is resonant with the Fabry-Pérot cavity, which means the effective detuning $\Delta_{\text{eff}} = 0$. Because the thin-film cavity is highly dissipative, we consider there is no photon inside. In order to describe the dynamics of the system, we derive that the eigenstates of the effective Hamiltonian read $|G\rangle|0\rangle_1|0\rangle_2$, $|0\rangle_1|1,\pm\rangle = (|E\rangle|0\rangle_1|0\rangle_2 \pm |G\rangle|0\rangle_1|1\rangle_2)/\sqrt{2}$. The state $|G\rangle|0\rangle_1|1\rangle_2$ means the nuclear ensemble is on the ground state, there is no photon in the thin-film cavity and there is one photon in the Fabry-Pérot cavity. The energy shift between the two excited states $|0\rangle_1|1,\pm\rangle$ is $2g_{\text{eff}}$.

In the time domain, we can directly observe the coherent energy exchange between the nuclei and the cavities. Here we show some numerical results by solving the full quantum master equation. Parameters for the thin-film cavity are taken from the experiment written in Refs. [11, 20]. According to experimental values for x-ray Fabry-Perot cavities [151, 152] with high reflectivity x-ray mirrors [153], we show different results with $\kappa_2 = \gamma$ and $\kappa_2 = 10\gamma$. Initially the nuclear ensemble is assumed to be in the excited state and both the two cavities are in their vacuum states. The numerical results for the time evolution of the photon numbers in the x-ray Fabry-Perot cavity $N_2(t) =< b^+ b >$ and the probability for the nuclear ensemble to be in the excited state $P_e(t)$ are demonstrated in Fig. 6.2 and Fig. 6.3. We also present the frequency spectrum of the system.

It is clear from the figures that the vacuum Rabi oscillation occurs with the Rabi frequency $\Omega_R = 2g_{\text{eff}}$ and the period equals to π/g_{eff} in Fig. 6.2(a). The two peaks in Fig. 6.2(b) represent the two vacuum splitting modes, with the detuning between the two splitting modes $2g_{\text{eff}}$.

Comparing the results in Fig. 6.2 ($\kappa_2 = \gamma$) and Fig. 6.3 ($\kappa_2 = 10\gamma$), there is a small middle peak appearing in Fig. 6.3(b). This is caused by the effective decay of the coupled cavities system κ_{eff}. In our simulation, the effective decay rate κ_{eff} in the case of $\kappa_2 = 10\gamma$ is three times larger than the case when $\kappa_2 = \gamma$. When the effective decay rate becomes large, the probability that the photon just propagates through the system directly increases. This is the reason behind the smaller peak in Fig. 6.3(b).

To summarize, we have presented a protocol for realizing strong coupling in the x-ray regime. We combine the merits of a thin-film cavity and a Fabry-Perot cavity in a highly dissipative situation. In this setup, vacuum Rabi oscillations can be observed on the level of single x-ray photons. We note however that there are several difficulties in the experiment implement of the proposed setup. For instance, the reflectivity of the Fabry-Perot cavity for the energy 14.414 kev which

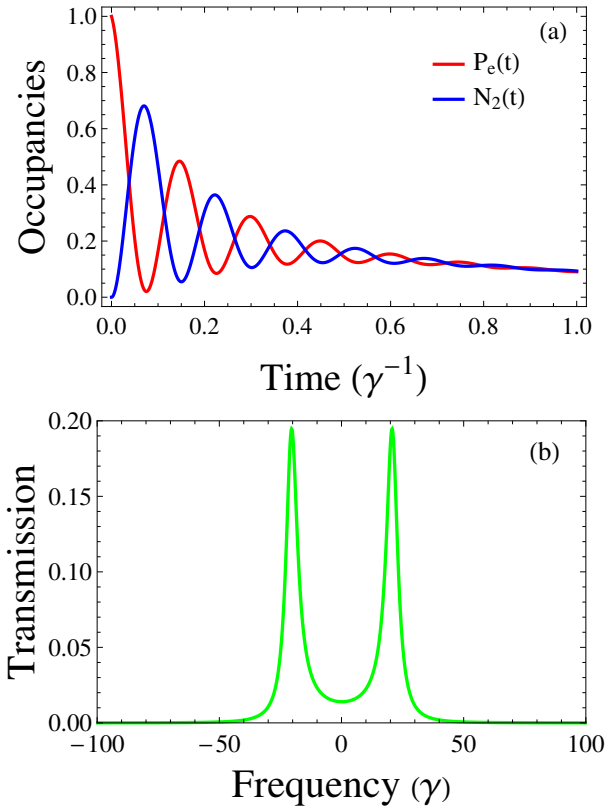

Figure 6.2: $\kappa_2 = \gamma$. (a) Time evolution of the photon numbers $N_2(t)$ and the probability $P_e(t)$. The oscillation is visible. (b) Frequency spectrum of the coupled cavities system.

is the resonant transition energy of ^{57}Fe is 0.879 [157]. This does not fulfill the requirement in our protocol. In addition, it is really difficult to prepare the nuclear ensemble in the excited state. The reflection of the thin-film cavity also plays a role in the system. In the following we will present another scheme to observe the oscillation between two ^{57}Fe nuclear ensembles using a different idea inspired by the setup of the two coupled cavities.

6.3 Collective oscillation of two nuclear ensembles

Coherent polariton dynamics is expected to improve the performance of a dissipative cavity when the latter is coupled to a high-Q but large-V auxiliary cavity via a strong dark state interaction [154]. In Sec. 6.2 we have theoretically shown that strong coupling can be reached on the level of single x-ray photons in a coupled cavities system. The x-ray Fabry-Perot cavity acts in this case as a storage and delay for the resonant photons which are otherwise rapidly lost from the dissipative cavity. Following this line, here we envisage another alternative to store an x-ray photon within the dissipative cavity by employing a thin film cavity with two layers of resonant ^{57}Fe nuclei, as illustrated in Fig. 6.4. Due to the construction of the cavity and the configuration of the field inside the cavity, the top layer placed at a note of the standing wave in the cavity does not interact initially with the

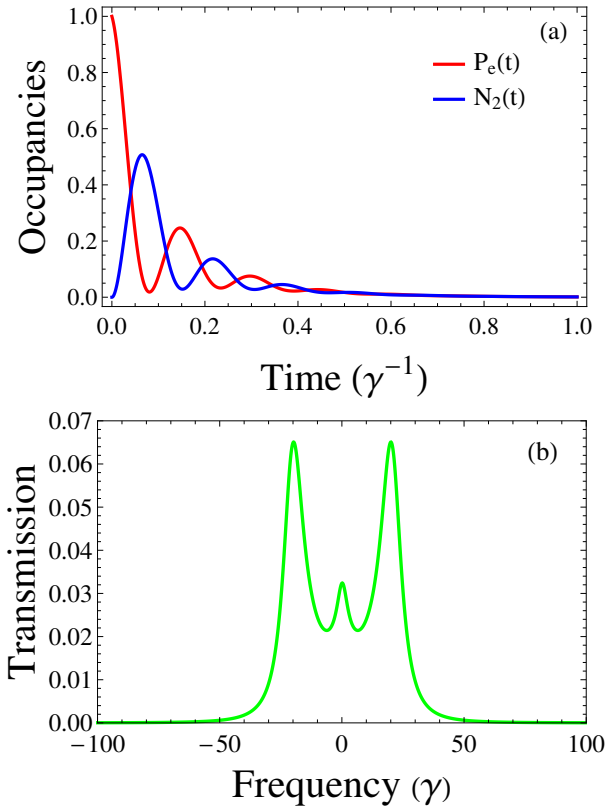

Figure 6.3: $\kappa_2 = 10\gamma$. (a) Time evolution of the photon numbers $N_2(t)$ and the probability $P_e(t)$. (b) Frequency spectrum of the coupled cavities system.

cavity field but can store and delay the photons which have resonantly interacted with the bottom layer, placed at an antinode. We theoretically show in the following that strong coupling between the two ^{57}Fe layers may occur and lead to pseudo-Rabi splitting of a single x-ray photon.

6.3.1 Theoretical approach

A theoretical quantum optics model for treating an ensemble of Mössbauer nuclei embedded in a thin-film waveguide has been developed in Ref. [33] and outlined here in Sec. 4.2. An extension considering multiple nuclear ensembles in the x-ray cavity has been developed in Ref. [34]. We briefly sketch the formalism in the following. The model [34] considers both multiple cavity modes and multiple layers simultaneously. The different cavity modes are distinguished by an upper index $[j]$ in square brackets and the curly brackets l indicate that the respective quantity is related to layer l. Taking into account multiple cavity modes, the Hamiltonian in Eq. (4.5) corresponding to the x-ray-cavity interaction reads

$$H_M = \sum_j \Delta_c^{[j]} \left(a_1^{[j]^+} a_1^{[j]} + a_2^{[j]^+} a_2^{[j]} \right) + i \sum_j \sqrt{2\kappa_R^{[j]}} \left[\left(\hat{a}_1^{[j]^*} \cdot \hat{a}_{in} \right) a_{in} a_1^{[j]^+} - \right.$$

$$\left. \left(\hat{a}_{in}^{[j]^*} \cdot \hat{a}_1^{[j]} \right) a_{in}^{[j]^*} a_1^{[j]} + \left(\hat{a}_2^{[j]^*} \cdot \hat{a}_{in} \right) a_{in} a_2^{[j]^+} - \left(\hat{a}_{in}^{[j]^*} \cdot \hat{a}_2^{[j]} \right) a_{in}^{[j]^*} a_2^{[j]} \right] . \qquad (6.16)$$

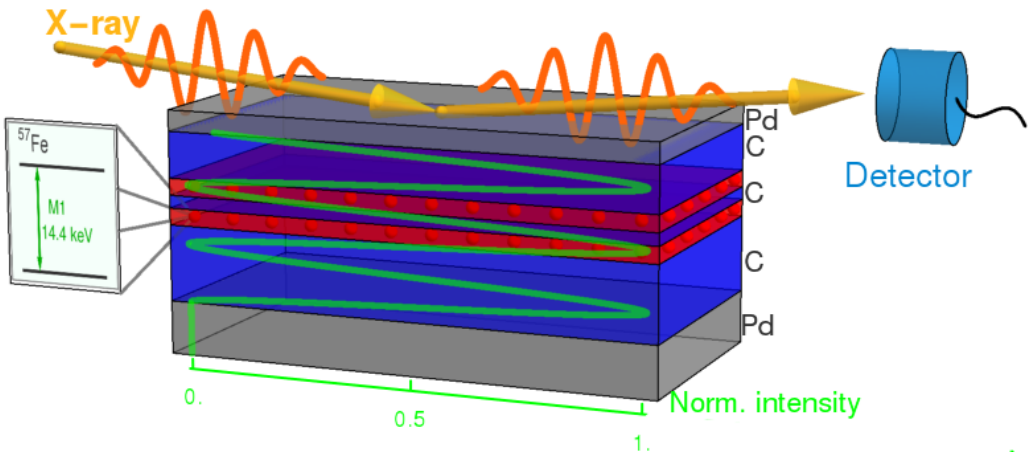

Figure 6.4: Schematic of the x-ray cavity containing two ^{57}Fe layers placed at a node and an antinode of the standing wave.

On the other hand, considering the multiple layers, the Hamiltonian in Eq. (4.6) describing cavity-nuclei interaction can be rewritten as follows

$$H_N = \sum_{l=1,2}\left(-\Delta\sum_{\mu}|E^l_\mu\rangle\langle E^l_\mu| - \sum_{\mu}\Delta_\mu|E^l_\mu\rangle\langle E^l_\mu|\right) + \sum_{l=1,2}\sum_{h=1}^{2}\sum_{\mu}\left[(\hat{d}^*_\mu\cdot\hat{a}_h)c_\mu\sqrt{N_\mu}g|E^l_\mu\rangle\langle G|\,a_h + (\hat{a}^*_h\cdot\hat{d}_\mu)c_\mu\sqrt{N_\mu}g^*a^+_h|G\rangle\langle E^l_\mu|\right]. \tag{6.17}$$

The next step is to use the Heisenberg equation of motion for the operator $a_h^{[j]}$ which reads

$$\frac{d}{dt}a_h^{[j]} = i\left[H_M + H_N, a_h^{[j]}\right] - \kappa^{[j]}a_h^{[j]} = 0\,. \tag{6.18}$$

Solving Eq. (6.18) and substituting the solution into Eqs. (6.16) and (6.17), we obtain the effective Hamiltonian

$$H = \left(\tilde{\Omega}^{\{1\}}|E^{\{1\}}\rangle\langle G| + h.c.\right) + \left(\tilde{\Omega}^{\{2\}}|E^{\{2\}}\rangle\langle G| + h.c.\right) + \left(\tilde{\delta}^{\{1\}} - \Delta\right)|E^{\{1\}}\rangle\langle E^{\{1\}}| + \left(\tilde{\delta}^{\{2\}} - \Delta\right)|E^{\{2\}}\rangle\langle E^{\{2\}}| + \left(\tilde{g}^{\{1,2\}}_{\text{eff}}|E^{\{1\}}\rangle\langle E^{\{2\}}| + h.c.\right), \tag{6.19}$$

where $|G\rangle$ and $|E\rangle$ denote generally the nuclear ensemble ground and excited states. More specifically, $|G\rangle$ denotes the collective ground state

$$|G\rangle = \underbrace{|g_1^{\{1\}}\rangle\ldots|g_{N^{\{1\}}}^{\{1\}}\rangle}_{N^{\{1\}}}\underbrace{|g_1^{\{2\}}\rangle\ldots|g_{N^{\{2\}}}^{\{2\}}\rangle}_{N^{\{2\}}}, \tag{6.20}$$

where, $|g^{\{1\}}\rangle$ and $|g^{\{2\}}\rangle$ are the ground states of individual nuclei in the layers $\{1\}$ and $\{2\}$, respectively, and $N^{\{1\}}$ and $N^{\{2\}}$ are the corresponding numbers of nuclei in the two layers. Current experiments employing the 14.4 keV resonance line in

^{57}Fe are mostly performed at modern synchrotron light sources, which have less than one resonant photon on average per pulse. Accordingly, we assume that only one atom can be excited at a time and define the excited states, for instance for one excited nucleus in layer $\{1\}$, as following:

$$|E^{\{1\}}\rangle = \frac{1}{\sqrt{N^{\{1\}}}} \sum_{n=1}^{N^{\{1\}}} e^{ik_C \cdot R^{(n)}} |g_1^{\{1\}}\rangle \dots |e_n^{\{1\}}\rangle \dots |g_{N^{\{1\}}}^{\{1\}}\rangle |g_1^{\{2\}}\rangle \dots |g_{N^{\{2\}}}^{\{2\}}\rangle \,, \tag{6.21}$$

with $|e_n^{\{1\}}\rangle$ denoting the excited nucleus n in layer $\{1\}$. A similar expression holds for the excited state $|E^{\{2\}}\rangle$ with a single nucleus excited in layer $\{2\}$.

The coefficients in Eq. (6.19) are given by [34]

$$\tilde{\Omega}^{\{l\}} = \sum_j \sqrt{\frac{2}{3}} \Omega^{[j]} g^{[j]\{l\}} \sqrt{N^{\{l\}}} \,, \tag{6.22}$$

$$\tilde{\delta}^{\{l\}} = \sum_j \frac{2}{3} \delta_{LS}^{[j]} |g^{[j]\{l\}}|^2 N^{\{l\}} \,, \tag{6.23}$$

$$\tilde{g}_{\text{eff}}^{\{1,2\}} = \sum_j \frac{2}{3} \delta_{LS}^{[j]} g^{[j]\{1\}} g^{[j]\{2\}^*} \sqrt{N^{\{1\}} N^{\{2\}}} \,, \tag{6.24}$$

where

$$\Omega^{[j]} = \frac{\sqrt{2\kappa_R^{[j]}} a_{in}}{\kappa^{[j]} + i\Delta_C^{[j]}} \,, \tag{6.25}$$

$$\delta_{LS}^{[j]} = \text{Im}\left(\frac{1}{\kappa^{[j]} + i\Delta_C^{[j]}} \right) \,, \tag{6.26}$$

$$\zeta_S^{[j]} = \text{Re}\left(\frac{1}{\kappa^{[j]} + i\Delta_C^{[j]}} \right) \,. \tag{6.27}$$

Here, $\kappa^{[j]}$ stands for the decay rate of cavity mode j, $\kappa_R^{[j]}$ denotes the coupling strength into the cavity mode j and $\Delta_C^{[j]}$ is the detuning between the resonant frequency of cavity mode j and the nuclear transition frequency of an isolated ^{57}Fe nucleus. Furthermore, $g^{[j]\{l\}}$ represents the coupling strength between layer l and cavity mode j.

In the effective Hamiltonian expression (6.19), the first line describes the driving of the two layers, the collective Lamb shift and the detuning are introduced in the second line and the last line represents the coherent coupling between the two layers. The incoherent part of the system is given by [34]:

$$L = -\left(\frac{\gamma}{2} + \tilde{\gamma}^{\{1\}} \right) L[\rho, |E^{\{1\}}\rangle\langle G|, |G\rangle\langle E^{\{1\}}|]$$

$$
\begin{aligned}
&- \left(\frac{\gamma}{2} + \tilde{\gamma}^{\{2\}}\right) L[\rho, |E^{\{2\}}\rangle\langle G|, |G\rangle\langle E^{\{2\}}|] \\
&- \tilde{\gamma}^{\{1,2\}} L[\rho, |E^{\{1\}}\rangle\langle G|, |G\rangle\langle E^{\{2\}}|] \\
&- \tilde{\gamma}^{\{1,2\}^*} L[\rho, |E^{\{2\}}\rangle\langle G|, |G\rangle\langle E^{\{1\}}|] \,. \qquad (6.28)
\end{aligned}
$$

with the coefficients

$$
\tilde{\gamma}^{\{l\}} = \sum_j \zeta_S^{[j]} \frac{2}{3} |g^{[j]\{l\}}|^2 N^{\{l\}} \,, \qquad (6.29)
$$

$$
\tilde{\gamma}^{\{1,2\}} = \sum_j \zeta_S^{[j]} \frac{2}{3} g^{[j]\{1\}} g^{[j]\{2\}^*} \sqrt{N^{\{1\}} N^{\{2\}}} \,. \qquad (6.30)
$$

The first two lines in Eq. (6.28) describe the spontaneous and superradiant decays, while the other two terms represent the incoherent coupling between the two layers which cause spontaneously generated coherence [22].

In Eqs. (6.19) and (6.28), two coupling mechanisms between the two ^{57}Fe layers are present. One is the coherent coupling with coupling strength $\tilde{g}_{\text{eff}}^{\{1,2\}}$. There is also an incoherent coupling part with the coupling strength $\tilde{\gamma}^{\{1,2\}}$. Recently, EIT-like spectra could be observed in the experiment by placing one layer at the node of the standing wave in the cavity and the other at the antinode [20], as shown in Fig. 6.4. In that experiment, the incidence angle was chosen to drive the third cavity mode with the cavity on resonance. For the EIT resonant case, the incoherent coupling strength $\tilde{\gamma}^{\{1,2\}}$ and the decay rate $\tilde{\gamma}^{\{2\}}$ are much larger than the coherent coupling strength $\tilde{g}_{\text{eff}}^{\{1,2\}}$. Thus, it is the incoherent inter-layer coupling process that plays the dominant role in this case.

In the off-resonant case, the incoherent coupling strength and the decay rate decrease by $1/\Delta_C^2$. The collective Lamb shift [11] and the coherent coupling strength decrease by $1/\Delta_C$. Therefore, there is a chance that the coherent coupling strength $\tilde{g}_{\text{eff}}^{\{1,2\}}$ is larger than the decay rate $\tilde{\gamma}^{\{2\}} + \frac{\gamma}{2}$. From Eq. (6.19), we find that there is an effective detuning between the two nuclei layers, $\Delta_{\text{eff}} = \tilde{\delta}^{\{1\}} - \tilde{\delta}^{\{2\}}$. We define a collective Rabi frequency between the two layers as

$$
\Omega_{R12} = \sqrt{4|\tilde{g}_{\text{eff}}^{\{1,2\}}|^2 + \Delta_{\text{eff}}^2} \,. \qquad (6.31)
$$

When the decay rates $2\tilde{\gamma}^{\{1\}} + \gamma < \Omega_{R12}$ and $2\tilde{\gamma}^{\{2\}} + \gamma < \Omega_{R12}$, we can observe the oscillation between the two nuclear layers. We note that the oscillation is not only due to the coupling between the two layers $\tilde{g}_{\text{eff}}^{\{1,2\}}$, but also to the effective detuning Δ_{eff}, arising from the different Lamb shifts of the transition frequency at the two layers. In experiment, one could observe the reflection spectrum and the reflection coefficient is derived as [34]

$$
R = \frac{\langle a_{out} \rangle}{a_{in}} = \left[-1 + \sum_j \frac{2\kappa_R^{[j]}}{\kappa^{[j]} + i\Delta_c^{[j]}} - \frac{i}{a_{in}} \frac{\sqrt{2\kappa_R^{[j]}}}{\kappa^{[j]} + i\Delta_c^{[j]}} \right.
$$

$$\times\sqrt{\frac{2}{3}}\sum_{l} g^{[j]\{l\}^*}\sqrt{N^{\{1\}}}\langle E_{\mu}^{\{l\}}|\rho|G\rangle\Bigg](\hat{a}_{out}^{*}\cdot\hat{a}_{in})\,. \tag{6.32}$$

6.3.2 Numerical results

We consider the cavity structure which has been used in the EIT experiment in a thin-film cavity in Ref. [20]. The structure of the cavity is shown in Table 6.1.

Table 6.1: Structure of the EIT-cavity in Ref. [20].

Material	Thickness (nm)
Pt	2.5
C	11.2
^{57}Fe	2
C	7
^{57}Fe	2
C	19.8
Pt	10

6.3.2.1 Simulation results by CONUSS

We start by presenting the simulation results of CONUSS [102] as benchmark which has been proved valid by many experiments [11, 20, 22, 111]. In Fig. 6.5, we present the calculated results for different incidence angles. In Fig. 6.5(a), the x-ray pulse probes the system at the resonant incidence angle and the EIT spectrum can be observed [20]. Then with increasing the incidence angles, the spectrum transforms from EIT to pseudo-Rabi splitting. In Fig. 6.5(d), the incidence angle is far away from the resonant angle and in this case two dips appear which represent two different resonant energies. This means the 14.4 kev resonant level of ^{57}Fe has been split in the off-resonant case. This feature is caused by the effective coupling between the two ^{57}Fe nuclear ensembles. When the effective coupling exceeds all the decay rates of the system in the off-resonant case, the pseudo-Rabi splitting between the two ensembles occurs.

In order to understand the process more clearly, we present the reflectivity as a function of the incidence angle and the detuning in Fig. 6.6. We find that there is always a dip around the resonant energy of ^{57}Fe. When the incidence angle deviates away from the resonant angle, the second dip forms with decreasing width. The two appearing dips in the off-resonant case represent the two split states.

6.3.2.2 Numerical results from the quantum model

Next we show the numerical results by the quantum model. The first step is to determine the parameters defined in the theoretical model in Sec. 6.3.1. In order

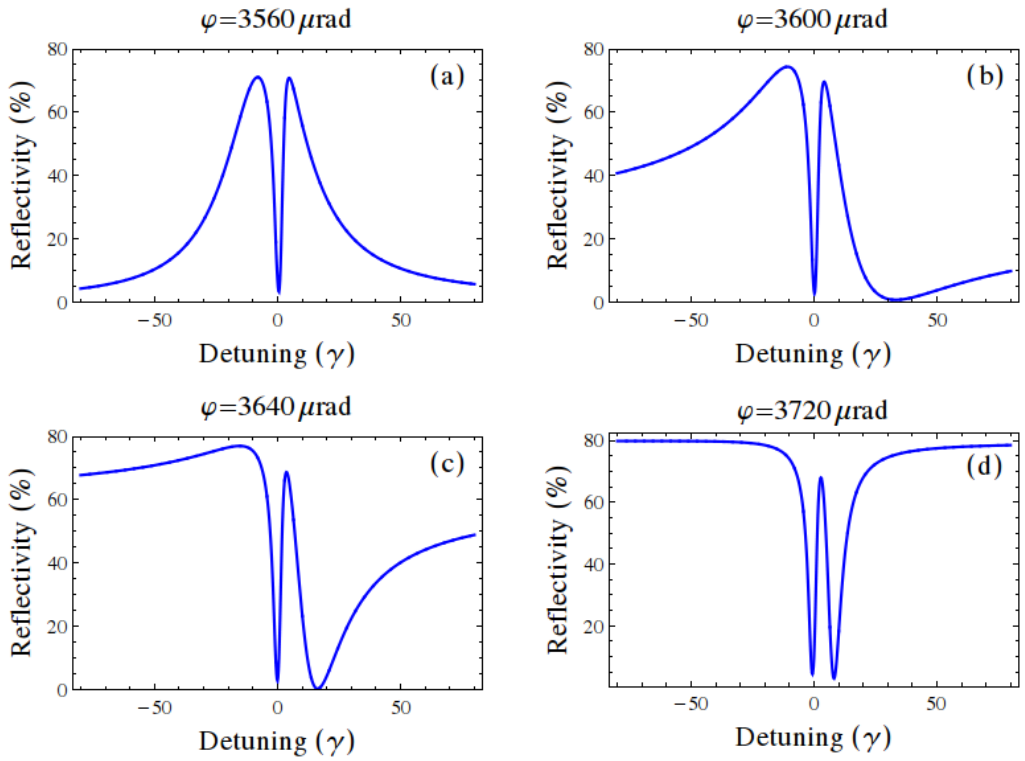

Figure 6.5: CONUSS reflectivity spectra at different grazing incidence angles for the EIT cavity used in Ref. [20].

to obtain the parameters, we write the reflection coefficient in Eq. (6.32) as [34]

$$R = R_C + R_N \,, \tag{6.33}$$

where R_C is the reflection caused by the cavity with

$$R_C = -1 + \sum_j \frac{2\kappa_R^{[j]}}{\kappa^{[j]} + i\Delta_c^{[j]}} \,, \tag{6.34}$$

and R_N is the nuclear contribution to the reflection coefficient with

$$R_N = -\frac{i}{a_{in}} \frac{\sqrt{2\kappa_R^{[j]}}}{\kappa^{[j]} + i\Delta_c^{[j]}} \sqrt{\frac{2}{3}} \sum_l g^{[j]\{l\}^*} \sqrt{N^{\{1\}}} \langle E_\mu^{\{l\}} | \rho | G \rangle \,. \tag{6.35}$$

In the following we take into account two effects which influence the cavity contribution of the reflection coefficient R_C [34]. First we consider the reflection from the bulk material. At x-ray energies the refractive index of cavity materials is less than 1, such that total reflection occurs for small incidence angles φ and complete absorption happens for larger angles. A smooth function $R_{\text{Envelope}}(\varphi)$ is used to describe this process. On the other side, due to the dispersion of the cavity material, an additional relative phase between the reflected light out of the cavity and the light entering the cavity has been observed [111]. Therefore, we apply a complex variable r instead of the cavity surface amplitude (-1) in Eq. (6.34). Now

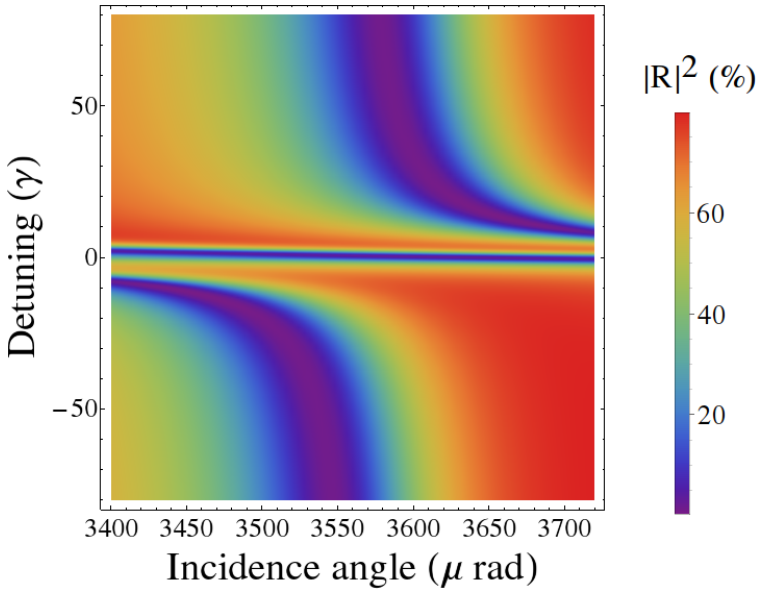

Figure 6.6: CONUSS reflectivity as a function of the incidence angle and the detuning for the EIT cavity used in Ref. [20].

the reflection contribution of the cavity is written as [34]

$$R_C = R_{\text{Envelope}}(\varphi)\left(r + \sum_j \frac{2\kappa_R^{[j]}}{\kappa^{[j]} + i\Delta_c^{[j]}}\right), \tag{6.36}$$

where

$$R_{\text{Envelope}}(\varphi) = \frac{\sin(\varphi) - \sqrt{\sin(\varphi)^2 + n^2 - 1}}{\sin(\varphi) - \sqrt{\sin(\varphi)^2 + n^2 - 1}}. \tag{6.37}$$

Here n is the refractive index of the platinum layer. If we do not consider the resonant contribution of the nuclei, the reflection curve can be represented by R_C in Eq. (6.36). In the same time we can obtain the reflection curve by the simulation of CONUSS in the absence of the nuclei. By fitting the reflection curves generated in the two different ways, we can determine the parameters $\kappa_R^{[j]}$ and $\kappa^{[j]}$. The reflection curves are shown in Fig. 6.7 and the determined parameters are presented in Table 6.4. We find that the reflection curves produced by CONUSS and the fitted quantum model are in good agreement.

After having obtained the cavity parameters, we proceed to find the value of the coupling strength $g^{[j]\{l\}}\sqrt{N^{\{l\}}}$. We decompose the coupling strength as [34]

$$g^{[j]\{l\}}\sqrt{N^{\{l\}}} = \varepsilon^{[j]\{l\}} \cdot \left(g^{\{l\}}\sqrt{N^{\{l\}}}\right), \tag{6.38}$$

where $\varepsilon^{[j]\{l\}}$ indicates the field amplitude of mode j at layer l in the cavity and $g^{\{l\}}\sqrt{N^{\{l\}}}$ is the scaling factor which represents the collective dipole moment. The thickness of the nuclear ensembles are the same and we consider the scale factors $g^{\{l\}}\sqrt{N^{\{l\}}}$ are the same for each ensemble. The relative field amplitudes $\varepsilon^{[j]\{l\}}$ are shown in Table 6.4.

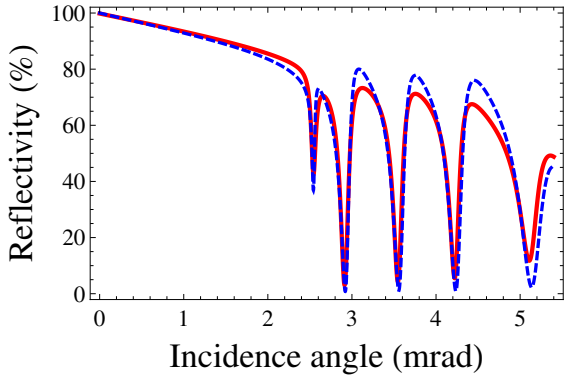

Figure 6.7: The reflection curves. The red solid line is produced by the quantum model and the blue dashed line is the simulation by CONUSS. By considering the reflection and the absorption of the cavity material, we can reproduce the reflection curve by the quantum model.

Table 6.2: Parameters for the quantum model describing the EIT-cavity used in Ref. [20].

Mode j	$\varphi_0^{[j]}$	$\kappa^{[j]}[\gamma]$	$\kappa_R^{[j]}[\gamma]$	$\varepsilon^{[j]\{1\}}$	$\varepsilon^{[j]\{1\}}$
1	2542	32735	259476	1.339 + 0.631 i	1.774 + 1.199 i
2	2920	300223	508933	2.572 + 1.337 i	0.548 + 0.378 i
3	3560	267362	692337	-0.241 + 0.152 i	-2.230 - 1.419 i
4	4236	331349	884613	-1.535 - 1.003 i	0.074 - 0.248 i
5	5136	576749	1919556	-1.127 - 1.512 i	1.156 + 1.500 i

The only uncertain parameter is the scale factor $\sqrt{N^{\{l\}}}$. So far we have not taken into account the resonant nuclear reflection. We can determine the parameter $\sqrt{N^{\{l\}}}$ by fitting the reflectivity spectrum by CONUSS with the quantum model result for the nuclear response. We choose the value of the incidence angle φ, for example, $\varphi = 3700\,\mu$rad. Then we fit the simulation result by CONUSS with the quantum model. After this we can determine the scale factor and the calculated results are shown in Fig. 6.8. We find that the two spectra of reflectivity calculated by CONUSS and the quantum model fit very well and the achieved parameter $\sqrt{N^{\{l\}}}$ in this case is about 1667γ.

Now all the parameters for the quantum model have been obtained. In the following we check the validity of the quantum model. We calculate the spectrum of the reflectivity as a function of the incidence angle and the detuning using the quantum model. The calculated results are presented in Fig. 6.9. We find that the main characteristics of the numerical result from the quantum model in Fig. 6.9 are the same as the calculated result by CONUSS in Fig. 6.6. The EIT dip occurs in the resonant case and two dips representing the splitting appear in the off-resonant case. This proves that the quantum model works very well for the thin-film cavity introduced in Ref. [20]. The pseudo-Rabi splitting between the two ^{57}Fe is predicted by theory.

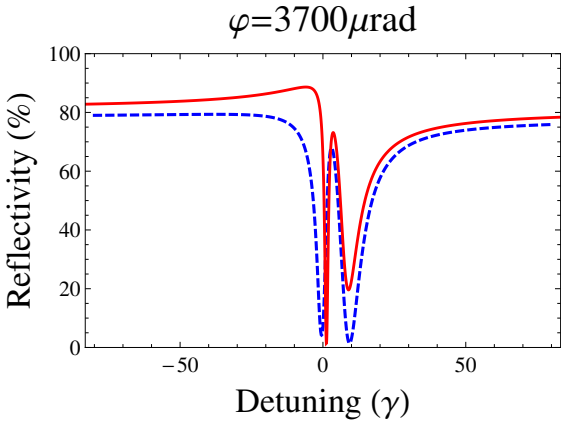

Figure 6.8: The reflection spectrum. The red solid line is produced by the quantum model and the blue dashed line is the simulation from CONUSS.

6.3.3 Preliminary experimental data

In this Section, we investigate numerically a different cavity structure which has been recently used in an experiment. The cavity structure is presented in Table 6.3. The two ^{57}Fe nuclear ensembles are located at the node and antinode of the cavity field, respectively. We first show the CONUSS reflectivity spectrum as the benchmark of the quantum model. Then we derive the parameters of the quantum model and present the reflectivity from the quantum model. Furthermore we compare our theory results with preliminary experimental data.

Table 6.3: Structure of the cavity in experiment.

Material	Thickness (nm)
Pt	1.5
^{57}Fe	1.3
C	14
^{57}Fe	1.3
C	14
Pt	10

6.3.3.1 Simulation results by CONUSS

The calculated reflectivity spectrum as a function of the incidence angle and the detuning calculated by CONUSS is shown in Fig. 6.10. We notice that the EIT spectrum is visible at the resonant incidence angle. In the off-resonant cases, the characteristics of pseudo-Rabi splitting are present. It is clear that two dips corresponding to the two split levels appear in the calculated spectrum.

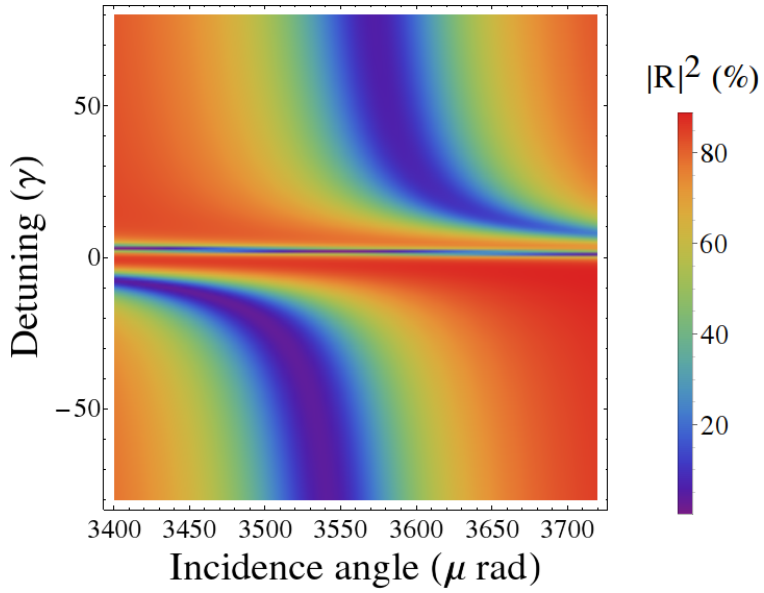

Figure 6.9: The reflectivity calculated as a function of the incidence angle and the detuning for the EIT cavity from the quantum model.

6.3.3.2 Numerical results from the quantum model

Unfortunately, we find that the quantum model presented in Sec. 6.3.1 does not work well in this special case. There is a significant difference between the cavity structures introduced in Tables 6.3 and 6.1. Compared to the cavity structure used for the EIT experiment presented in Table 6.1, in this new case there is no carbon layer between the platinum and the ^{57}Fe nuclear layers. There is a great chance that the incident x-ray pulse interacts directly with the first layer. We take into account this effect and modify the quantum model in Sec. 6.3.1. In that model, the probe pulse interacts with the cavity mode directly. This is introduced in Eq. (6.16) and the cavity mode excites the nuclear layers as described by Eq. (6.17). Here we consider that the probe pulse not only interacts with the cavity mode but also has some possibility to excite the first layer directly. So the effective Hamiltonian is rewritten as

$$\begin{aligned} H = &\left(\tilde{\Omega}_0|E^{\{1\}}\rangle\langle G| + h.c.\right) + \left(\tilde{\Omega}^{\{1\}}|E^{\{1\}}\rangle\langle G| + h.c.\right) \\ &+ \left(\tilde{\Omega}^{\{2\}}|E^{\{2\}}\rangle\langle G| + h.c.\right) + \left(\tilde{\delta}^{\{1\}} - \Delta\right)|E^{\{1\}}\rangle\langle E^{\{1\}}| \\ &+ \left(\tilde{\delta}^{\{2\}} - \Delta\right)|E^{\{2\}}\rangle\langle E^{\{2\}}| + \left(\tilde{g}_{\text{eff}}^{\{1,2\}}|E^{\{1\}}\rangle\langle E^{\{2\}}| + h.c.\right) , \end{aligned} \tag{6.39}$$

where $\tilde{\Omega}_0$ denotes the effective Rabi frequency between the external field and the first nuclear layer. By fitting the reflection curve calculated by CONUSS with the quantum model, we obtain the cavity parameters for the quantum model and present them in Table 6.4.

We proceed then to include the nuclear reflection. We take the incidence angle $\varphi = 3672\,\mu$rad and fit the reflectivity calculated by CONUSS with the quantum

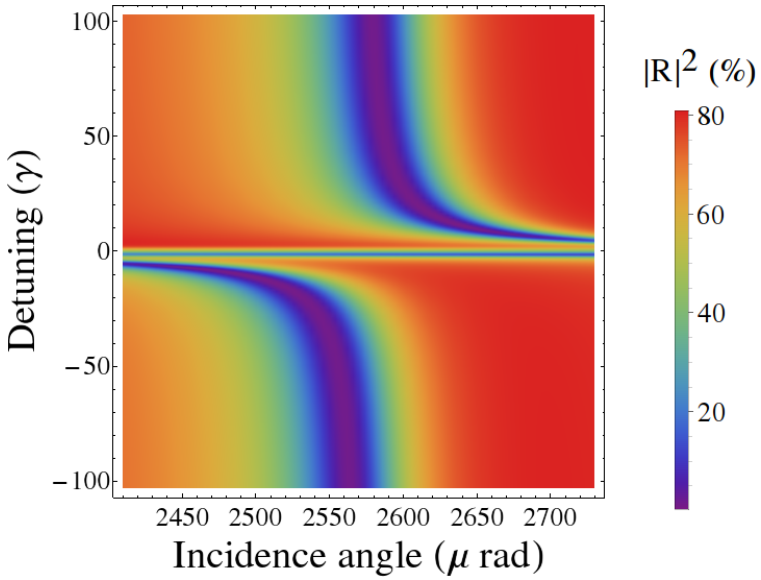

Figure 6.10: CONUSS reflectivity as a function of the incidence angle and the detuning for the cavity structure presented in Table 6.3.

Table 6.4: Parameters for the quantum model of the special cavity structure used in the experiment.

Mode j	$\varphi_0^{[j]}$	$\kappa^{[j]}[\gamma]$	$\kappa_R^{[j]}[\gamma]$	$\varepsilon^{[j]\{1\}}$	$\varepsilon^{[j]\{1\}}$
1	2574	166695	292602	1.453 + 0.468 i	3.356 + 1.864 i
2	3201	279898	759801	1.736 + 0.707 i	-0.443 - 0.028 i
3	4274	446029	1601760	1.537 + 1.033 i	1.856 - 1.602 i
4	5247	642697	2263580	1.305 + 1.124 i	0.352 - 0.167 i

model. The results are shown in Fig. 6.11. The numerical result from the quantum model fits well with the calculated result by CONUSS at the dips. There is a small difference about the cavity contribution to the reflection. By fitting the results by CONUSS, we obtain the values of the scale factor and the external Rabi frequency which are $808\,\gamma$ and $(-0.37 - 1.87i)\,\gamma$, respectively.

We have thus obtained all the parameters for the quantum model and calculate the reflectivity spectrum as a function of the incidence angle and the detuning. The numerical results are presented in Fig. 6.12. The result obtained from the quantum model reflects the main features from the CONUSS simulation shown in Fig. 6.10. Our results show the EIT-like spectrum in the resonant case and the pseudo-Rabi splitting in off-resonant case.

6.3.3.3 Experimental results

The group of Ralf Röhlsberger has recently performed an experiment at the European Synchrotron Radiation Facility (ESRF) in Grenoble, France, using a cavity

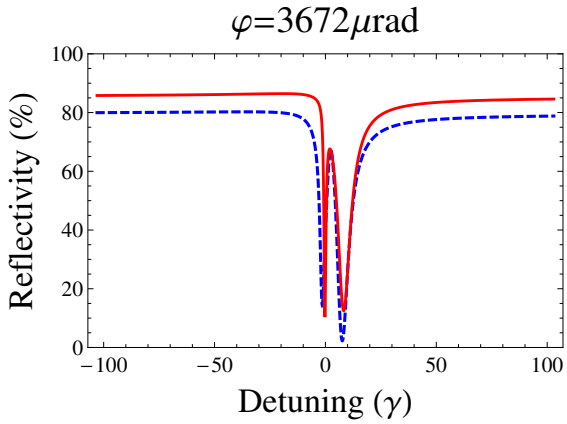

Figure 6.11: The reflectivity spectrum for incidence angle $\varphi = 3672\,\mu$rad. The red solid line is produced from the quantum model and the blue dashed line is the simulation from CONUSS.

sample with the structure parameters presented in Table 6.3. A preliminary experimental data plot is shown in Fig. 6.13. In this figure we can qualitatively observe the transition from the EIT-like spectrum to pseudo-Rabi splitting by changing the incidence angle. The EIT-like spectrum appears at the back of the figure. With increasing incidence angle, two dips form in front of the figure as the pseudo-Rabi splitting occurs. The two dips denote the two split levels. Thus, we may conclude that our theoretical predictions have been confirmed by experimental data.

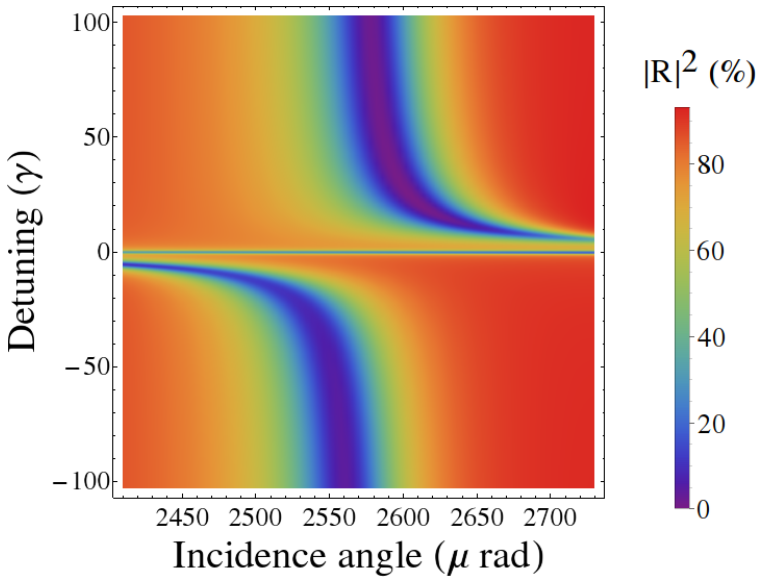

Figure 6.12: The reflectivity calculated as a function of the incidence angle and the detuning for the cavity structure presented in Table 6.3 from the quantum model.

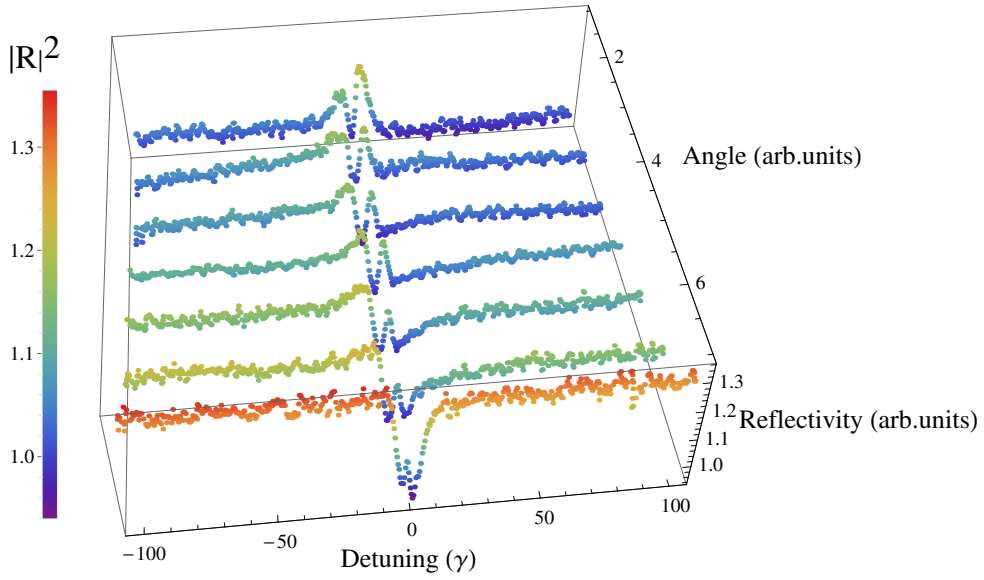

Figure 6.13: Preliminary experimental data obtained at the ESRF. The transition from the EIT-like spectrum at the resonance incidence angle (back) to the pseudo-Rabi splitting (front) can be observed. The color coding refers to the reflectivity.

Chapter 7

Summary and outlook

Summary

In this thesis, collective effects of nuclei in single x-ray photon superradiance have been investigated. First, in Chapter 2 we have developed a new model to describe the collective emission of a single photon from a cloud of generic two-level systems in the presence of magnetic field. We have presented the single-photon radiation spectrum in terms of the superradiance decay rate and the collective Lamb shift value in the absence of the magnetic field. The analysis of the different parameter regimes for superradiance and Lamb shift have shown that for the cases with large Lamb shift, a so far unknown modification consisting of a broadening of the magnetic splitting structure of the resonance lines occurs. Moreover, for vanishing Lamb shift and strong superradiant decay, an EIT-like spectrum is achieved, with a transparency window appearing in the radiation spectrum instead of two resonant peaks.

In order to observe these effects in a specific system, in Chapter 4 we have studied a thin-film x-ray cavity with an embedded ^{57}Fe nuclear layer which has been employed for experimental studies of the superradiance decay and collective Lamb shift in Ref. [11]. The specific cavity system can be also described theoretically by a quantum cavity model previously developed in Ref. [33]. Our calculations have shown that our results obtained from the more general model presented in Chapter 2 applied to the thin-film cavity are consistent with the ones of the quantum cavity model. According to our calculations, we could show that the main effects in Chapter 2, such as the EIT-like spectrum and the broadened magnetic hyperfine splitting, should be observable in the thin-film x-ray cavity system under experimental parameters available today. Based on the EIT-like spectrum obtained in the thin-film cavity with embedded ^{57}Fe nuclei, in Chapter 5 we have shown from the theory side that a spectrally narrow x-ray pulse can be completely stopped in a nuclear medium. The pulse can be mapped onto nuclear coherence and retrieved at later times, with storage time determined by the nuclear excited state mean lifetime, on the order of hundred nanoseconds. This may have many applications in quantum information and computation.

In Chapter 6, we have focused our attention on the collective strong coupling of x-rays and nuclei. We could predict the collective strong coupling of x-rays in a coupled cavities system composed of a thin-film cavity with embedded nuclei and an x-ray Fabry-Pérot cavity. Our results show that Rabi oscillation in x-ray regime occur due to the collective strong coupling. However, unfortunately this setup can

not be implemented experimentally at present due to challenging requirements. This is why we have investigated also a different case in which the coupled cavity setup is replaced by two ^{57}Fe nuclear ensembles placed in the thin-film cavity. In some cases the collective strong coupling between these two nuclear ensembles can be reached. Our results have shown that pseudo-Rabi splitting between the two ^{57}Fe nuclear ensembles reminiscent of the Rabi oscillations in strong coupling regime occurs.

Whereas the results summarized so far are all in the limit $R \ll \lambda$ where R is the size of the sample (of nuclei or atoms) and λ is the wavelength of the photon, in Chapter 3 we have studied the case that $R \gg \lambda$ in nuclear forward scattering. Two types of time-dependent perturbations were considered for coherent control of the resonantly scattered x-ray quanta. Firstly, the simultaneous coherent propagation of two pulses through the nuclear sample was addressed. We have found that the signal of a weak pulse can be enhanced or suppressed by a stronger pulse simultaneously propagating through the sample in counter-propagating geometry. Secondly, the effect of a time-dependent hyperfine splitting was investigated and we put forward a scheme that allows parts of the spectrum to be shifted forward in time.

Based on the results presented in the thesis, a short outlook for possible future studies is given in the following.

Outlook

Subradiance of x-ray photons

In this thesis, we saw that collective effects in an ensemble of identical atoms (or nuclei) lead to the superradiance of a single photon. Actually Dicke predicted that these cooperative effects could either enhance spontaneous emission (superradiance) or suppress it (subradiance) [7]. Superradiance and subradiance stem from the same underlying phase-lock mechanism in which superradiance is based on a constructive interference between many scattered waves and subradiance is correspondingly caused by a destructive interference effect [158]. However, superradiance is much more difficult to observe because the superradiant states are weakly coupled to the environment and the subradiant emission is smeared out in space and time. Recently, subradiance of optical photons in an extended and dilute cold-atom sample containing a huge number of particles has been observed [159]. It would be very interesting to consider the possibility to observe subradiance of x-ray photons in the thin-film cavity with embedded nuclei. The density of the nuclei in the ensemble may play an important role to obtain the subradiance of x-ray photons.

Time-domain oscillations between two ^{57}Fe nuclear ensembles in a thin-film cavity

In Chapter 6 we have shown that the collective strong coupling can be reached between two ^{57}Fe nuclear ensembles in a thin-film cavity. Pseudo-Rabi splitting

between two nuclear ensembles in the frequency domain should occur according to our theoretical predictions and this was also qualitatively confirmed by preliminary experimental data. As future plans, we can also study the effects of the collective strong coupling between the nuclear ensembles in the time domain. An oscillation between the two nuclear ensembles should be observed.

An x-ray Fabry-Pérot cavity with ^{57}Fe

Fabry-Pérot cavities for x-rays have been built during the last few years [151, 152]. Unfortunately, the best reflectivity parameters could not be achieved so far for the transition energy of ^{57}Fe. We hope that with the development of x-ray mirrors, it will be possible to obtain better performance for a Fabry-Pérot cavity resonant with the transition of ^{57}Fe. It would be interesting to investigate what will happen if we confine a ^{57}Fe sample in a resonant Fabry-Pérot cavity. The wavelength of the cavity field would be in sub-Å regime and it would be much smaller than the size of the nuclear ensemble. The theory which describes the atom-photon interaction in a optical cavity would no longer be appropriate in this case and a new approach would be required.

An x-ray-optomechanical interface with thin-film cavities

A recent proposal aims at investigating theoretically an x-ray optomechanical interface [160]. The device uses resonant interactions of x-rays with nuclear transitions, in conjunction with an optomechanical setup interacting with optical photons. An alternative setup could be designed using instead of a simple nuclear sample a thin-film x-ray cavity as the ones addresses in this thesis. Theoretical simulations for the operation of such an interface are in progress.

Bibliography

[1] S. L. McCall and E. L. Hahn, "Self-induced transparency by pulsed coherent light," Physical Review Letters **18**, 908 (1967).

[2] S. L. McCall and E. L. Hahn, "Self-induced transparency," Physical Review **183**, 457 (1969).

[3] I. Abella, N. Kurnit, and S. Hartmann, "Photon echoes," Physical review **141**, 391 (1966).

[4] C. Patel and R. Slusher, "Photon echoes in gases," Physical Review Letters **20**, 1087 (1968).

[5] G. Hocker and C. Tang, "Observation of the optical transient nutation effect," Physical Review Letters **21**, 591 (1968).

[6] R. G. Brewer and R. Shoemaker, "Photo echo and optical nutation in molecules," Physical Review Letters **27**, 631 (1971).

[7] R. H. Dicke, "Coherence in spontaneous radiation processes," Physical Review **93**, 99 (1954).

[8] M. O. Scully and A. A. Svidzinsky, "The effects of the N atom collective Lamb shift on single photon superradiance," Physics Letters A **373**, 1283 (2009).

[9] A. A. Svidzinsky, J.-T. Chang, and M. O. Scully, "Cooperative spontaneous emission of N atoms: Many-body eigenstates, the effect of virtual Lamb shift processes, and analogy with radiation of N classical oscillators," Physical Review A **81**, 053821 (2010).

[10] M. O. Scully and A. A. Svidzinsky, "The Lamb shift-yesterday, today, and tomorrow," Science **328**, 1239 (2010).

[11] R. Röhlsberger, K. Schlage, B. Sahoo, S. Couet, and R. Rüffer, "Collective lamb shift in single-photon superradiance," Science **328**, 1248 (2010).

[12] B. W. Adams, C. Buth, S. M. Cavaletto, J. Evers, Z. Harman, C. H. Keitel, A. Pálffy, A. Picón, R. Röhlsberger, Y. Rostovtsev, and K. Tamasaku, J. Mod. Opt. **60**, 2 (2013).

[13] J. Arthur *et al.*, *Linac Coherent Light Source (LCLS). Conceptual Design Report* (SLAC, Stanford, 2002).

[14] XFEL @ SACLA, Official Website (2012), http://xfel.riken.jp/eng/sacla/.

[15] P. Emma, R. Akre, J. Arthur, R. Bionta, C. Bostedt, J. Bozek, A. Brachmann, P. Bucksbaum, R. Coffee, F.-J. Decker, Y. Ding, D. Dowell, S. Edstrom, A. Fisher, J. Frisch, S. Gilevich, J. Hastings, G. Hays, P. Hering, Z. Huang, R. Iverson, H. Loos, M. Messerschmidt, A. Miahnahri, S. Moeller, H.-D. Nuhn, G. Pile, D. Ratner, J. Rzepiela, D. Schultz, T. Smith, P. Stefan, H. Tompkins, J. Turner, J. Welch, W. White, J. Wu, G. Yocky, and J. Galayda, "First lasing and operation of an angstrom-wavelength free-electron laser," Nature Photon. **4**, 641 (2010).

[16] C. Gutt, P. Wochner, B. Fischer, H. Conrad, M. Castro-Colin, S. Lee, F. Lehmkühler, I. Steinke, M. Sprung, W. Roseker, D. Zhu, H. Lemke, S. Bogle, P. H. Fuoss, G. B. Stephenson, M. Cammarata, D. M. Fritz, A. Robert, and G. Grübel, "Single Shot Spatial and Temporal Coherence Properties of the SLAC Linac Coherent Light Source in the Hard X-Ray Regime," Phys. Rev. Lett. **108**, 024801 (2012).

[17] T. Ishikawa, H. Aoyagi, T. Asaka, Y. Asano, N. Azumi, T. Bizen, H. Ego, K. Fukami, T. Fukui, Y. Furukawa, S. Goto, H. Hanaki, T. Hara, T. Hasegawa, T. Hatsui, A. Higashiya, T. Hirono, N. Hosoda, M. Ishii, T. Inagaki, Y. Inubushi, T. Itoga, Y. Joti, M. Kago, T. Kameshima, H. Kimura, Y. Kirihara, A. Kiyomichi, T. Kobayashi, C. Kondo, T. Kudo, H. Maesaka, X. M. Marechal, T. Masuda, S. Matsubara, T. Matsumoto, T. Matsushita, S. Matsui, M. Nagasono, N. Nariyama, H. Ohashi, T. Ohata, T. Ohshima, S. Ono, Y. Otake, C. Saji, T. Sakurai, T. Sato, K. Sawada, T. Seike, K. Shirasawa, T. Sugimoto, S. Suzuki, S. Takahashi, H. Takebe, K. Takeshita, K. Tamasaku, H. Tanaka, R. Tanaka, T. Tanaka, T. Togashi, K. Togawa, A. Tokuhisa, H. Tomizawa, K. Tono, S. Wu, M. Yabashi, M. Yamaga, A. Yamashita, K. Yanagida, C. Zhang, T. Shintake, H. Kitamura, and N. Kumagai, "A compact X-ray free-electron laser emitting in the sub-angstrom region," Nature Photon. **6**, 540 (2012).

[18] Y. V. Shvyd'ko, Hyperfine Interact. **125**, 173 (2000).

[19] R. Röhlsberger, *Nuclear Condensed Matter Physics With Synchrotron Radiation: Basic Principles, Methodology and Applications* (Springer-Verlag, 2004).

[20] R. Röhlsberger, H.-C. Wille, K. Schlage, and B. Sahoo, "Electromagnetically induced transparency with resonant nuclei in a cavity," Nature **482**, 199 (2012).

[21] R. Röhlsberger, T. Klein, K. Schlage, O. Leupold, and R. Rüffer, "Coherent x-ray scattering from ultrathin probe layers," Phys. Rev. B **69**, 235412 (2004).

[22] K. P. Heeg, H.-C. Wille, K. Schlage, T. Guryeva, D. Schumacher, I. Uschmann, K. S. Schulze, B. Marx, T. Kämpfer, G. G. Paulus, *et al.*, "Vacuum-assisted generation and control of atomic coherences at x-ray energies," Phys. Rev. Lett. **111**, 073601 (2013).

[23] K. P. Heeg, J. Haber, D. Schumacher, L. Bocklage, H.-C. Wille, K. S. Schulze, R. Loetzsch, I. Uschmann, G. G. Paulus, R. Rüffer, R. Röhlsberger, and J. Evers, "Tunable Subluminal Propagation of Narrow-band X-Ray Pulses," Phys. Rev. Lett. **114**, 203601 (2015).

[24] A. Politi, M. J. Martin J. Cryan, J. G. Rarity, S. Yu, and J. L. O'Brien, Science **320**, 646 (2008).

[25] W.-T. Liao, A. Pálffy, and C. H. Keitel, Phys. Rev. Lett. **109**, 197403 (2012).

[26] W.-T. Liao and A. Pálffy, arXiv:1308.3121 (2013).

[27] J. Gunst, C. H. Keitel, and A. Pálffy, "Logical operations with single x-ray photons via dynamically-controlled nuclear resonances," Sci. Rep. **6** (2016).

[28] F. Vagizov, V. Antonov, Y. V. Radeonychev, R. N. Shakhmuratov, and O. Kocharovskaya, Nature **508**, 80 (2014).

[29] R. N. Shakhmuratov, F. G. Vagizov, V. A. Antonov, Y. V. Radeonychev, M. O. Scully, and O. Kocharovskaya, "Transformation of a single-photon field into bunches of pulses," Phys. Rev. A **92**, 023836 (2015).

[30] A. Pálffy, J. Evers, and C. H. Keitel, "Isomer triggering via nuclear excitation by electron capture," Physical review letters **99**, 172502 (2007).

[31] J. Gunst, Y. A. Litvinov, C. H. Keitel, and A. Pálffy, "Dominant secondary nuclear photoexcitation with the x-ray free-electron laser," Physical Review Letters **112**, 082501 (2014).

[32] J. Hannon and G. Trammell, "Coherent γ-ray optics," Hyperfine Interactions **123**, 127 (1999).

[33] K. P. Heeg and J. Evers, "X-ray quantum optics with Mössbauer nuclei embedded in thin-film cavities," Phys. Rev. A **88**, 043828 (2013).

[34] K. P. Heeg and J. Evers, "Collective effects between multiple nuclear ensembles in an x-ray cavity-QED setup," Physical Review A **91**, 063803 (2015).

[35] M. Fleischhauer, A. Imamoglu, and J. P. Marangos, "Electromagnetically induced transparency: Optics in coherent media," Rev. Mod. Phys. **77**, 633 (2005).

[36] D. Phillips, A. Fleischhauer, A. Mair, R. Walsworth, and M. D. Lukin, "Storage of light in atomic vapor," Phys. Rev. Lett. **86**, 783 (2001).

[37] C. Liu, Z. Dutton, C. H. Behroozi, and L. V. Hau, "Observation of coherent optical information storage in an atomic medium using halted light pulses," Nature **409**, 490 (2001).

[38] M. D. Lukin, Rev. Mod. Phys. **75**, 457 (2003).

[39] A. V. Gorshkov, A. André, M. D. Lukin, and A. S. Sørensen, Phys. Rev. A **76**, 033804 (2007).

[40] G. Heinze, C. Hubrich, and T. Halfmann, "Stopped Light and Image Storage by Electromagnetically Induced Transparency up to the Regime of One Minute," Phys. Rev. Lett. **111**, 033601 (2013).

[41] T. Hara, Y. Inubushi, T. Katayama, T. Sato, H. Tanaka, T. Tanaka, T. Togashi, K. Togawa, K. Tono, M. Yabashi, and T. Ishikawa, Nature Commun. **4** (2013).

[42] A. Marinelli, D. Ratner, A. A. Lutman, J. Turner, J. Welch, F.-J. Decker, H. Loos, C. Behrens, S. Gilevich, A. A. Miahnahri, *et al.*, Nature Commun. **6**, 6369 (2015).

[43] J.-M. Raimond, M. Brune, and S. Haroche, "Manipulating quantum entanglement with atoms and photons in a cavity," Reviews of Modern Physics **73**, 565 (2001).

[44] M. J. Hartmann, F. G. Brandao, and M. B. Plenio, "Strongly interacting polaritons in coupled arrays of cavities," Nature Physics **2**, 849 (2006).

[45] A. D. Greentree, C. Tahan, J. H. Cole, and L. C. Hollenberg, "Quantum phase transitions of light," Nature Physics **2**, 856 (2006).

[46] H. Kimble, "The quantum internet," Nature **453**, 1023 (2008).

[47] L.-M. Duan, M. Lukin, J. I. Cirac, and P. Zoller, "Long-distance quantum communication with atomic ensembles and linear optics," Nature **414**, 413 (2001).

[48] K. M. Birnbaum, A. Boca, R. Miller, A. D. Boozer, T. E. Northup, and H. J. Kimble, "Photon blockade in an optical cavity with one trapped atom," Nature **436**, 87 (2005).

[49] L. S. Bishop, J. Chow, J. Koch, A. Houck, M. Devoret, E. Thuneberg, S. Girvin, and R. Schoelkopf, "Nonlinear response of the vacuum Rabi resonance," Nature Physics **5**, 105 (2008).

[50] P. F. Herskind, A. Dantan, J. P. Marler, M. Albert, and M. Drewsen, "Realization of collective strong coupling with ion Coulomb crystals in an optical cavity," Nature Physics **5**, 494 (2009).

[51] Y. Dudin, L. Li, F. Bariani, and A. Kuzmich, "Observation of coherent many-body Rabi oscillations," Nature Physics **8**, 790 (2012).

[52] A. Gaëtan, Y. Miroshnychenko, T. Wilk, A. Chotia, M. Viteau, D. Comparat, P. Pillet, A. Browaeys, P. Grangier, *et al.*, "Observation of collective excitation of two individual atoms in the Rydberg blockade regime," Nature Physics **5**, 115 (2009).

[53] M. O. Scully and A. A. Svidzinsky, "The super of superradiance," Science **325**, 1510 (2009).

[54] N. Skribanowitz, I. Herman, J. MacGillivray, and M. Feld, "Observation of Dicke superradiance in optically pumped HF gas," Physical Review Letters **30**, 309 (1973).

[55] M. Gross, C. Fabre, P. Pillet, and S. Haroche, "Observation of near-infrared Dicke superradiance on cascading transitions in atomic sodium," Physical Review Letters **36**, 1035 (1976).

[56] Y. Kaluzny, P. Goy, M. Gross, J. Raimond, and S. Haroche, "Observation of self-induced Rabi oscillations in two-level atoms excited inside a resonant cavity: the ringing regime of superradiance," Physical review letters **51**, 1175 (1983).

[57] N. Ginzburg, A. Sergeev, I. Zotova, Y. V. Novozhilova, N. Y. Peskov, I. Konoplev, A. Phelps, A. Cross, S. Cooke, P. Aitken, *et al.*, "Experimental observation of superradiance in millimeter-wave band," Nuclear Instruments and Methods in Physics Research Section A: Accelerators, Spectrometers, Detectors and Associated Equipment **393**, 352 (1997).

[58] M. Scheibner, T. Schmidt, L. Worschech, A. Forchel, G. Bacher, T. Passow, and D. Hommel, "Superradiance of quantum dots," Nature Physics **3**, 106 (2007).

[59] A. A. Svidzinsky and M. O. Scully, "Evolution of collective N atom states in single photon superradiance: Effect of virtual Lamb shift processes," Optics Communications **282**, 2894 (2009).

[60] M. O. Scully, "Collective Lamb Shift in Single Photon Dicke Superradiance," Phys. Rev. Lett. **102**, 143601 (2009).

[61] W. E. Lamb Jr and R. C. Retherford, "Fine structure of the hydrogen atom by a microwave method," Physical Review **72**, 241 (1947).

[62] C. Schwartz, "Lamb shift in the helium atom," Physical Review **123**, 1700 (1961).

[63] G. W. Erickson and D. R. Yennie, "Radiative level shifts, I. Formulation and lowest order lamb shift," Annals of Physics **35**, 271 (1965).

[64] P. J. Mohr, "Lamb shift in a strong Coulomb potential," Physical Review Letters **34**, 1050 (1975).

[65] C. Schwob, L. Jozefowski, B. De Beauvoir, L. Hilico, F. Nez, L. Julien, F. Biraben, O. Acef, J.-J. Zondy, and A. Clairon, "Optical Frequency Measurement of the 2 S- 12 D Transitions in Hydrogen and Deuterium: Rydberg Constant and Lamb Shift Determinations," Physical Review Letters **82**, 4960 (1999).

[66] M. Chaichian, M. Sheikh-Jabbari, and A. Tureanu, "Hydrogen atom spectrum and the Lamb shift in noncommutative QED," Physical Review Letters **86**, 2716 (2001).

[67] A. A. Svidzinsky, J.-T. Chang, and M. O. Scully, "Cooperative spontaneous emission of N atoms: Many-body eigenstates, the effect of virtual Lamb shift processes, and analogy with radiation of N classical oscillators," Phys. Rev. A **81**, 053821 (2010).

[68] A. Svidzinsky and J.-T. Chang, "Cooperative spontaneous emission as a many-body eigenvalue problem," Physical Review A **77**, 043833 (2008).

[69] M. O. Scully and M. S. Zubairy, *Quantum Optics* (Cambridge University Press, 2006).

[70] J. Hannon and G. Trammell, "Coherent γ-ray optics," Hyperfine Interact. **123-124**, 127 (1999).

[71] T. J. Bürvenich, J. Evers, and C. H. Keitel, Phys. Rev. Lett. **96**, 142501 (2006).

[72] C. G. Schroer, O. Kurapova, J. Patommel, P. Boye, J. Feldkamp, B. Lengeler, M. Burghammer, C. Riekel, L. Vincze, A. van der Hart, and M. Kuchler, Appl. Phys. Lett. **87**, 124103 (2005).

[73] C. G. Schroer and B. Lengeler, Phys. Rev. Lett. **94**, 054802 (2005).

[74] H. C. Kang, H. Yan, R. P. Winarski, M. V. Holt, J. Maser, C. Liu, R. Conley, S. Vogt, A. T. Macrander, and G. B. Stephenson, Appl. Phys. Lett. **92**, 221114 (2008).

[75] Y. Shvyd'ko, S. Stoupin, A. Cunsolo, A. H. Said, and X. Huang, Nature Phys. **6**, 196 (2010).

[76] Y. Shvyd'ko, S. Stoupin, V. Blank, and S. Terentyev, Nature Photon. **5**, 539 (2011).

[77] H. Yumoto, H. Mimura, T. Koyama, S. Matsuyama, K. Tono, T. Togashi, Y. Inubushi, T. Sato, T. Tanaka, T. Kimura, H. Yokoyama, J. Kim, Y. Sano, Y. Hachisu, M. Yabashi, H. Ohashi, H. Ohmori, T. Ishikawa, and K. Yamauchi, Nature Photon. **7**, 43 (2013).

[78] T. Osaka, M. Yabashi, Y. Sano, K. Tono, Y. Inubushi, T. Sato, S. Matsuyama, T. Ishikawa, and K. Yamauchi, Opt. Express **21**, 2823 (2013).

[79] R. Coussement *et al.*, Phys. Rev. Lett. **89**, 107601 (2002).

[80] I. Wong, A. Grigoriu, J. Roslund, T.-S. Ho, and H. Rabitz, "Laser-driven direct quantum control of nuclear excitations," Phys. Rev. A **84**, 053429 (2011).

[81] R. N. Shakhmuratov, F. Vagizov, and O. Kocharovskaya, "Single gamma-photon revival from sandwich absorbers," Phys. Rev. A **87**, 013807 (2013).

[82] W.-T. Liao, A. Pálffy, and C. H. Keitel, Phys. Lett. B **705**, 134 (2011).

[83] W.-T. Liao, A. Pálffy, and C. H. Keitel, Phys. Rev. C **87**, 054609 (2013).

[84] U. Van Bürck, Hyperfine Interact. **123**, 483 (1999).

[85] Y. Kagan, A. M. Afanas'ev, and V. G. Kohn, J. Phys. C **12**, 615 (1979).

[86] J. P. Hannon and G. T. Trammell, Hyperfine Interact. **123**, 127 (1999).

[87] G. V. Smirnov, Hyperfine Interact. **97/98**, 551 (1996).

[88] G. V. Smirnov, U. van Bürck, J. Arthur, A. Q. R. Baron, A. I. Chumakov, S. L. Ruby, W. Potzel, and B. G. S., Phys. Rev. Lett. **77**, 183 (1996).

[89] X. Kong, W.-T. Liao, and A. Pálffy, "Field control of single x-ray photons in nuclear forward scattering," New J. Phys. **16**, 013049 (2014).

[90] M. O. Scully, E. S. Fry, C. H. R. Ooi, and K. Wódkiewicz, Phys. Rev. Lett. **96**, 010501 (2006).

[91] P. Ring and P. Schuck, *The Nuclear Many-Body Problem* (Springer Verlag, New York, 1980).

[92] Y. V. Shvyd'ko, Phys. Rev. B **59**, 9132 (1999).

[93] W.-T. Liao, *Coherent Control of Nuclei and X-rays* (Springer Theses, Heidelberg, 2013).

[94] Y. Kagan, Hyperfine Interact. **123/124**, 83 (1999).

[95] A. R. Edmonds, *Angular Momentum in Quantum Mechanics* (Princeton University Press, 1996).

[96] Y.-W. Lin, W.-T. Liao, T. Peters, H.-C. Chou, J.-S. Wang, H.-W. Cho, P.-C. Kuan, and I. A. Yu, Phys. Rev. Lett. **102**, 213601 (2009).

[97] H. Mimura, S. Handa, T. Kimura, H. Yumoto, D. Yamakawa, H. Yokoyama, S. Matsuyama, K. Inagaki, K. Yamamura, Y. Sano, *et al.*, Nature Physics **6**, 122 (2009).

[98] H. Jex, A. Ludwig, F. J. Hartmann, E. Gerdau, and O. Leupold, Europhys. Lett. **40, 317 (1997)**.

[99] N. Miura, T. Osada, and S. Takeyama, J. Low Temp. Phys. **133**, 139 (2003).

[100] R. Röhlsberger, T. S. Toellner, W. Sturhahn, K. W. Quast, E. E. Alp, A. Bernhard, E. Burkel, O. Leupold, and E. Gerdau, Phys. Rev. Lett. **84**, 1007 (2000).

[101] C. Gardiner and P. Zoller, *Quantum noise: a handbook of Markovian and non-Markovian quantum stochastic methods with applications to quantum optics*, Vol. 56 (Springer Science & Business Media, 2004).

[102] W. Sturhahn, "CONUSS and PHOENIX: Evaluation of nuclear resonant scattering data," Hyperfine Interactions **125**, 149 (2000).

[103] W. Sturhahn and E. Gerdau, "Evaluation of time-differential measurements of nuclear-resonance scattering of x rays," Physical Review B **49**, 9285 (1994).

[104] A. Papandrew, M. Lucas, R. Stevens, I. Halevy, B. Fultz, M. Hu, P. Chow, R. Cohen, and M. Somayazulu, "Absence of magnetism in hcp iron-nickel at 11 K," Physical review letters **97**, 087202 (2006).

[105] H. Paulsen, H. Grünsteudel, W. Meyer-Klaucke, M. Gerdan, H. Grünsteudel, A. Chumakov, R. Rüffer, H. Winkler, H. Toftlund, and A. Trautwein, "The spin-crossover complex [Fe (tpa)(NCS) 2]," The European Physical Journal B-Condensed Matter and Complex Systems **23**, 463 (2001).

[106] J. Becker, "The Use of the Field Emission Electron Microscope in Adsorption Studies of W on W and Ba on W," Bell System Technical Journal **30**, 907 (1951).

[107] O. Leupold, J. Pollmann, E. Gerdau, H. Rüter, G. Faigel, M. Tegze, G. Bortel, R. Rüffer, A. Chumakov, and A. Baron, "Nuclear resonance scattering of synchrotron radiation at the 21.5 keV resonance of 151Eu," EPL (Europhysics Letters) **35**, 671 (1996).

[108] E. Gerdau and H. DeWaard, "Nuclear resonant scattering of synchrotron radiation," Hyperfine Interactions **123** (1999).

[109] H. Grünsteudel, H. Paulsen, W. Meyer-Klaucke, H. Winkler, A. Trautwein, H. Grünsteudel, A. Baron, A. Chumakov, R. Rüffer, and H. Toftlund, "Nuclear resonant scattering and molecular orbital calculations on an iron (II) spin-crossover complex," Hyperfine interactions **113**, 311 (1998).

[110] E. Zeldov, J. R. Clem, M. McElfresh, and M. Darwin, "Magnetization and transport currents in thin superconducting films," Physical Review B **49**, 9802 (1994).

[111] K. P. Heeg, C. Ott, D. Schumacher, H.-C. Wille, R. Röhlsberger, T. Pfeifer, and J. Evers, "Interferometric phase detection at x-ray energies via Fano resonance control," Phys. Rev. Lett. **114**, 207401 (2015).

[112] U. Fano, "Effects of configuration interaction on intensities and phase shifts," Physical Review **124**, 1866 (1961).

[113] M. Fleischhauer and M. Lukin, "Dark-state polaritons in electromagnetically induced transparency," Phys. Rev. Lett. **84**, 5094 (2000).

[114] Y. V. Shvyd'ko, T. Hertrich, U. van Bürck, E. Gerdau, O. Leupold, J. Metge, H. D. Rüter, S. Schwendy, G. V. Smirnov, W. Potzel, and P. Schindelmann, "Storage of Nuclear Excitation Energy through Magnetic Switching," Phys. Rev. Lett. **77**, 3232 (1996).

[115] W.-T. Liao, A. Pálffy, and C. H. Keitel, "Coherent storage and phase modulation of single hard-x-ray photons using nuclear excitons," Phys. Rev. Lett. **109**, 197403 (2012).

[116] L. Young, E. P. Kanter, B. Krässig, Y. Li, A. M. March, S. T. Pratt, R. Santra, S. H. Southworth, N. Rohringer, L. F. DiMauro, G. Doumy, C. A. Roedig, N. Berrah, L. Fang, M. Hoener, P. H. Bucksbaum, J. P. Cryan, S. Ghimire, J. M. Glownia, D. A. Reis, J. D. Bozek, C. Bostedt, and M. Messerschmidt, "Femtosecond electronic response of atoms to ultra-intense X-rays," Nature **466**, 56 (2010).

[117] E. P. Kanter, B. Krässig, Y. Li, A. M. March, P. Ho, N. Rohringer, R. Santra, S. H. Southworth, L. F. DiMauro, G. Doumy, C. A. Roedig, N. Berrah, L. Fang, M. Hoener, P. H. Bucksbaum, S. Ghimire, D. A. Reis, J. D. Bozek, C. Bostedt, M. Messerschmidt, and L. Young, "Unveiling and Driving Hidden Resonances with High-Fluence, High-Intensity X-Ray Pulses," Phys. Rev. Lett. **107**, 233001 (2011).

[118] N. Rohringer, D. Ryan, R. A. London, M. Purvis, F. Albert, J. Dunn, J. D. Bozek, C. Bostedt, A. Graf, R. Hill, S. P. Hau-Riege, and J. Rocca, Nature **481**, 488 (2012).

[119] K. Tamasaku and T. Ishikawa, Phys. Rev. Lett. **98**, 244801 (2007).

[120] K. Tamasaku, K. Sawada, E. Nishibori, and T. Ishikawa, Nature Phys. **7**, 705 (2011).

[121] S. Shwartz, M. Fuchs, J. B. Hastings, Y. Inubushi, T. Ishikawa, T. Katayama, D. A. Reis, T. Sato, K. Tono, M. Yabashi, S. Yudovich, and S. E. Harris, "X-Ray Second Harmonic Generation," Phys. Rev. Lett. **112**, 163901 (2014).

[122] M. Fuchs, M. Trigo, J. Chen, S. Ghimire, S. Shwartz, M. Kozina, M. Jiang, T. Henighan, C. Bray, G. Ndabashimiye, *et al.*, Nature Phys. **11**, 964 (2015).

[123] F. Vagizov, V. Antonov, Y. V. Radeonychev, R. N. Shakhmuratov, and O. Kocharovskaya, "Coherent control of the waveforms of recoilless [ggr]-ray photons," Nature **508**, 80 (2014).

[124] R. N. Shakhmuratov, F. G. Vagizov, V. A. Antonov, Y. V. Radeonychev, M. O. Scully, and O. Kocharovskaya, Phys. Rev. A **92**, 023841 (2015).

[125] J. Gunst, C. H. Keitel, and A. Pálffy, preprint arXiv:1506.00517 (2015).

[126] M. D. Lukin, S. F. Yelin, and M. Fleischhauer, "Entanglement of Atomic Ensembles by Trapping Correlated Photon States," Phys. Rev. Lett. **84**, 4232 (2000).

[127] J. Hald, J. L. Sørensen, C. Schori, and E. S. Polzik, "Spin Squeezed Atoms: A Macroscopic Entangled Ensemble Created by Light," Phys. Rev. Lett. **83**, 1319 (1999).

[128] B. Julsgaard, J. Sherson, J. I. Cirac, J. Fiurášek, and E. S. Polzik, "Experimental demonstration of quantum memory for light," Nature **432**, 482 (2004).

[129] M. Hosseini, B. M. Sparkes, G. Hétet, J. J. Longdell, P. K. Lam, and B. C. Buchler, Nature **461**, 241 (2009).

[130] V. R. Almeida, C. A. Barrios, R. R. Panepucci, and M. Lipson, "All-optical control of light on a silicon chip," Nature **431**, 1081 (2004).

[131] L. Liu *et al.*, Nature Photon. **4**, 182 (2010).

[132] P. J. Shadbolt, M. R. Verde, A. Peruzzo, A. Politi, A. Laing, M. Lobino, J. C. Matthews, M. G. Thompson, and J. L. O'Brien, "Generating, manipulating and measuring entanglement and mixture with a reconfigurable photonic circuit," Nature Photon. **6**, 45 (2012).

[133] D. J. Moss, R. Morandotti, G. A. L., and M. Lipson, Nature Photon. **7**, 597 (2013).

[134] L. V. Hau, S. E. Harris, Z. Dutton, and C. H. Behroozi, Nature **397**, 594 (1999).

[135] T. Baba, Nature Photon. **2**, 465 (2008).

[136] B. Wu, J. F. Hulbert, E. J. Lunt, K. Hurd, A. R. Hawkins, and H. Schmidt, Nature Photon. **4**, 776 (2010).

[137] Y. V. Shvyd'ko, "Nuclear resonant forward scattering of x rays: Time and space picture," Phys. Rev. B **59**, 9132 (1999).

[138] P. Anisimov and O. Kocharovskaya, "Decaying-dressed-state analysis of a coherently driven three-level Λ system," Journal of Modern Optics **55**, 3159 (2008).

[139] G. V. Smirnov, U. van Bürck, A. I. Chumakov, A. Q. R. Baron, and R. Rüffer, "Synchrotron Mössbauer source," Phys. Rev. B **55**, 5811 (1997).

[140] T. Mitsui, M. Seto, R. Masuda, K. Kiriyama, and Y. Kobayashi, "Synchrotron Radiation M? ssbauer Spectroscopy Using Doppler-shifted 14.4 keV Single-line 57Fe-M? ssbauer Radiation," Jpn. J. Appl. Phys. **46**, L703 (2007).

[141] V. Potapkin, A. I. Chumakov, G. V. Smirnov, J.-P. Celse, R. Rüffer, C. McCammon, and L. Dubrovinsky, "The 57Fe synchrotron Mössbauer source at the ESRF," J. Synchrotron Radiat. **19**, 559 (2012).

[142] T. Toellner, E. Alp, W. Sturhahn, T. Mooney, X. Zhang, M. Ando, Y. Yoda, and S. Kikuta, "Polarizer/analyzer filter for nuclear resonant scattering of synchrotron radiation," Appl. Phys. Lett. **67**, 1993 (1995).

[143] T. Toellner, E. Alp, T. Graber, R. Henning, S. Shastri, G. Shenoy, and W. Sturhahn, "Synchrotron Mössbauer spectroscopy using high-speed shutters," J. Synchrotron Radiat. **18**, 183 (2011).

[144] A. B. Matsko, Y. V. Rostovtsev, O. Kocharovskaya, A. S. Zibrov, and M. O. Scully, "Nonadiabatic approach to quantum optical information storage," Phys. Rev. A **64**, 043809 (2001).

[145] A. S. Zibrov, A. B. Matsko, O. Kocharovskaya, Y. V. Rostovtsev, G. R. Welch, and M. O. Scully, "Transporting and Time Reversing Light via Atomic Coherence," Phys. Rev. Lett. **88**, 103601 (2002).

[146] G. Smirnov, U. Van Bürck, J. Arthur, S. Popov, A. Baron, A. Chumakov, S. Ruby, W. Potzel, and G. Brown, "Nuclear exciton echo produced by ultrasound in forward scattering of synchrotron radiation," Physical review letters **77**, 183 (1996).

[147] H. Jex, A. Ludwig, F. Hartmann, E. Gerdau, and O. Leupold, "Ultrasound-induced echoes in the nuclear-exciton decay utilising synchrotron radiation Bragg-scattered by a quartz crystal," EPL (Europhysics Letters) **40**, 317 (1997).

[148] P. R. Berman, "Cavity quantum electrodynamics," (1994).

[149] S. Horoche and D. Kleppner, "Cavity quantum electrodynamics," Phys. Today **42**, 24 (1989).

[150] H. Walther, B. T. Varcoe, B.-G. Englert, and T. Becker, "Cavity quantum electrodynamics," Reports on Progress in Physics **69**, 1325 (2006).

[151] Y. V. Shvyd'ko, M. Lerche, H.-C. Wille, E. Gerdau, M. Lucht, H. D. Rüter, E. E. Alp, and R. Khachatryan, "X-Ray Interferometry with Microelectron-volt Resolution," Phys. Rev. Lett. **90**, 013904 (2003).

[152] X. R. Huang, D. P. Siddons, A. T. Macrander, R. W. Peng, and X. S. Wu, "Multicavity X-Ray Fabry-Perot Resonance with Ultrahigh Resolution and Contrast," Phys. Rev. Lett. **108**, 224801 (2012).

[153] Y. Shvyd'Ko, S. Stoupin, V. Blank, and S. Terentyev, "Near-100% bragg reflectivity of x-rays," Nature Photon. **5**, 539 (2011).

[154] Y.-C. Liu, X. Luan, H.-K. Li, Q. Gong, C. W. Wong, and Y.-F. Xiao, "Coherent Polariton Dynamics in Coupled Highly Dissipative Cavities," Phys. Rev. Lett. **112**, 213602 (2014).

[155] A. Steyerl and K.-A. Steinhauser, "Proposal of a Fabry-Perot-type interferometer for X-rays," Zeitschrift für Physik B Condensed Matter **34**, 221 (1979).

[156] K.-D. Liss, R. Hock, M. Gomm, B. Waibel, A. Magerl, M. Krisch, and R. Tucoulou, "Storage of X-ray photons in a crystal resonator," Nature **404**, 371 (2000).

[157] Y. V. Shvyd'ko and E. Gerdau, "Backscattering mirrors for X-rays and Mössbauer radiation," Hyperfine Interactions **123**, 741 (1999).

[158] A. Carmele, "Storing Light in the Dark," Physics Online Journal **9** (2016).

[159] W. Guerin, M. O. Araújo, and R. Kaiser, "Subradiance in a Large Cloud of Cold Atoms," Phys. Rev. Lett. **116**, 083601 (2016).

[160] W.-T. Liao and A. Pálffy, "An Optomechanical Interface Bridging X-Ray and Optical Photons," arXiv preprint arXiv:1508.06769 (2015).

Acknowledgements

During the study of my PhD in Heidelberg , I have spent a very good time and have met many very nice people. Without their encouragement, help and support, this thesis would not be possible.

I would like to express my deepest gratitude to my supervisor PD. Dr. Adriana Pálffy. She is a wonderful teacher. Her passion for physics inspires me. I always recall the first time when she shared with me her idea about the x-ray Fabry-Pérot cavity. It was a snowy afternoon, and despite of the terrible weather she went directly from her home to my office and told me that she just thought of an idea about the x-ray Fabry-Pérot cavity. It was about ten days before the birth of her cute boy Elijah. At that moment I learned so much about how deep one's love for physics could be. Her scientific insights and her way of doing sciences influence me. I have learned many things from her, such as how to deal with physics problems, how to write an academic paper, how to give a nice talk and so on. I think I have improved a lot because of her. She gave me a lot of useful suggestions on not only science but also life. I sincerely appreciate for working with her in the last few years.

I am sincerely grateful to Honorarprof. Christoph H. Keitel for his great help throughout my PhD study. I would like to thank him not only for offering me a position to study in the Theory division at the Max Planck Institute for Nuclear Physics, but also for the financial support for the conferences and summer schools during my PhD study.

I am deeply grateful to Prof. Jörg Jäckel for reading my thesis, writing the second reference report and attending my examination.

I am deeply grateful to Prof. Thomas Pfeifer not only for being the member of my examination committee but also for his useful suggestions during my PhD study.

I am deeply grateful to Prof. Klaus Pfeilsticker for attending my examination as a examiner.

I am deeply grateful to Prof. Jianmin Yuan (袁建民). As the supervisor of my master study, he supported me to study in Germany. During my PhD study, he also gave me many suggestions through emails and phone calls. I appreciate for his help.

I would like to thank my proofreaders Jonas Gunst, Lida Zhang (张理达) and Yuanbin Wu (吴远彬). They have given me many useful comments and hints about the thesis.

I would like to thank Jonas Gunst and Kilian Heeg for their help in translating the abstract of this thesis into German.

I would like to thank Lida Zhang (张理达) and Wen-Te Liao (廖文德) for their help during my PhD study. They have answered me many questions in physics and also taught me skills about using softwares such as Mathematica and Latex. They have helped me solve many problems.

I would like to thank Dr. Jörg Evers for answering me many questions and giving me many suggestions on x-ray quantum optics.

I would like to thank Kilian Heeg and Jonas Gunst for the discussions about x-rays. Kilian answered me many questions about the x-ray thin-film cavity. Jonas gave me many suggestions and we shared many views about x-ray quantum optics.

I would like to thank Jianxing Li (栗建兴) for his help during my daily life.

I would like to thank Ms Sibel Babacan for her kind help in administrative affairs.

I would like to thank my colleagues: Jonas Gunst, Lida Zhang, Kilian Heeg, Wen-Te Liao, Andreas Reichegger, Patrick Reiser, Paolo Lango...We had a great lunch time during the last three and a half years.

I would to like thank my other friends in our institute, Luling Jin (金璐玲), Meng Wen (温猛), Ni Cui (崔妮), Yanwei Li (李延伟), Ruoyu Liu (柳若愚), Chunhai Lyu (吕纯海)，Zuoye Liu (刘作业),Yonghao Mi (米永浩), Difa Ye (叶地发), Xueguang Ren (任雪光), Suo Tang (唐锁), Suli Han (韩素立), Helen Poon (潘海琳). I really enjoyed the time we spent together.

I would like to thank Randolf Beerwerth for answering me many questions about German society and American culture. We had a lot of fun during his stay in our institute.

I would like to thank Lerui Liang (梁乐睿) for his help in the last three years.

I would like to thank Yi Liu (刘毅). Everytime I need to go somewhere by car, Yi always drives me there.

I would like to thank Fan Wang (王凡) for his help whenever I need it.

In particular, my sincere thanks go to my beloved Hanqi Yu (虞涵棋). Her smile made me happy no matter how tired I was during the writing of this thesis. Thanks

for her support and it really means a lot to me.

Last but not least, I am sincerely grateful to my family: my father Chuanbao Kong (孔传宝), my mother Xiuying Yin (殷秀英)，my brother in law Zengning Zhou (周增宁)，my sister Juan Kong (孔娟) and my cute niece Jiajin Zhou (周佳锦). Your understanding, support and love make me who I am. I know you are always there no matter what happens.